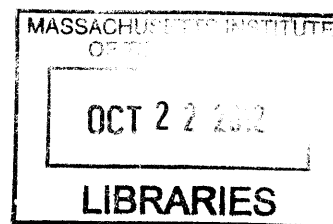Design and Characterization of Tunable Stiffness Flexural Bearings

by

Aaron E. Ramirez

Sc.B. Mechanical Engineering
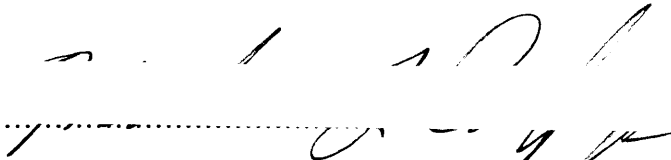Massachusetts Institute of Technology, 2010

Submitted to the Department of Mechanical Engineering

in Partial Fulfillment of the Requirements for the Degree of

Master of Science in Mechanical Engineering

at the

Massachusetts Institute of Technology

September 2012

Signature of Author...
Department of Mechanical Engineering
August 20, 2012

Certified by...
Martin L. Culpepper
Associate Professor of Mechanical Engineering
Thesis Supervisor

Accepted by...
David E. Hardt
Professor of Mechanical Engineering
Graduate Officer

(this page intentionally left blank)

Design and Characterization of Tunable Stiffness Flexural Bearings

by

Aaron E. Ramirez

Submitted to the Department of Mechanical Engineering
On August 20, 2012 in Partial Fulfillment of the
Requirements for the Degree of Master of Science in
Mechanical Engineering

ABSTRACT

Compressed flexures have a downwards-tunable stiffness in their compliant directions; their stiffness can theoretically be reduced by up to four orders of magnitude. The compression-stiffness relation is linear for most of the loading, and this behavior can be taken advantage of to use the flexure as a tunable spring, opening up new design possibilities. Compressed flexures present the possibility of developing more sensitive flexure-based instruments such as accelerometers. The purpose of this research was to characterize the behavior of compressed flexures and develop guidelines for their design. Tradeoffs were assessed when substituting compressed flexures for conventional flexures and their suitability for use in a precision system.

An experimental setup was designed and built to test a stage guided by four compressed flexure bearings. Compression was applied to the test flexures via a displacement input that was de-amplified by a wedge pair to increase preload resolution. The motion in each of the stage's six degrees of freedom in response to flexure compression and in response to a voice coil actuator acting in the flexure's compliant direction was measured by seven capacitance probes arranged around the test stage, and a seventh capacitance probe measured the input displacement.

With the experimental setup it was found that a stiffness reduction of a factor of 7 was possible. The magnitude of parasitic motions in the test stage were found to increase linearly with flexure compression. When being actuated in the compliant direction, parasitic motions were evident with magnitudes of the same order of magnitude as the sensor noise. Compressed flexures are highly sensitive to thermal variations; a 0.5 $°C$ temperature increase resulted in an 11% increase in stiffness. A model developed in this thesis predicts that deviations from column straightness of 2% of the flexure thickness limit the stiffness reduction to a factor of 1.2, while a deviation of 0.2% allows for a stiffness reduction of 10,000.

Thesis Supervisor: Martin L. Culpepper
Title: Associate Professor of Mechanical Engineering

(this page intentionally left blank)

ACKNOWLEDGEMENTS

Lastly I would like to thank my mother, without whom none of this would have been possible. She was the one who inspired in me a love of learning, and she invested much of herself into making sure I had everything I needed to be successful, and for that I am eternally grateful. Gracias mami, por todo lo que has hecho por mi.

CONTENTS

9

10

11

(this page intentionally left blank)

FIGURES

14

15

(this page intentionally left blank)

TABLES

(this page intentionally left blank)

1

INTRODUCTION

The purpose of this thesis was to generate the knowledge required to use compressed flexures as a machine element with a tunable stiffness reducible by one or more orders of magnitude. Their properties are not well understood and pose an area of research for use in novel flexure mechanisms; this research sought to characterize the behavior of compressed flexures and develop guidelines for their design. Elastic instability is ordinarily seen as a failure mode to be designed against, but in this work elastic instability is instead used to design a new class of low-stiffness flexural bearing. Tradeoffs were assessed when substituting compressed flexures for conventional flexures and their suitability for use in a precision flexure system. An experimental setup was built to assess the behavior of a set of compressed flexures (Figure 1.1).

The importance of this work is that it will demonstrate advantages of compressed flexures over conventional flexures, expand the engineer's toolkit with a novel machine element, introduce a new class of flexure-based devices which offer high stiffness relative to the reduced-stiffness degree of freedom, decrease the overall size of flexure systems, and enhance performance of flexures made of brittle materials.

The impact of this thesis is its significance to flexure-based instrumentation such as MEMS devices, accelerometers and the ability to design new devices, such as an adjustable mechanical displacement divider.

19

Compressed flexures have a tunable stiffness in their compliant directions; their stiffness is theoretically reducible by up to four orders of magnitude. The compression-stiffness relation is linear for approximately 80% of the loading range, and this behavior may be taken advantage of to use the flexure as a tunable spring.
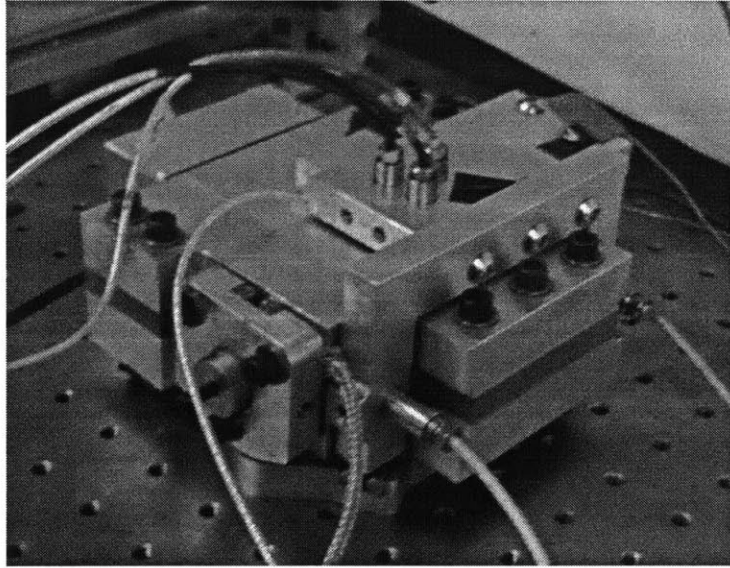
Figure 1.1: Photograph of experimental setup use to test compressed flexures.

1.1.1 Uncompressed flexures as a precision machine element

Since the 19th century, flexural elements have been utilized by engineers developing precision instrumentation or design engineers seeking to obtain guided motion from a monolithic structure. Flexures are widely utilized by precision engineers because of their advantages, which include:

- Excellent suitability for manufacturing processes such as abrasive waterjet machining or wire-electro-discharge machining, which can cut flexures out of plate stock with 125 μm and 5 μm tolerances, respectively

- Deterministic behavior

- Stiction-free motion

- Linear behavior, for small displacements

As in all things engineering, tradeoffs must be made – flexures are not well-suited for every engineering problem. Disadvantages of flexures include that they

- Exhibit hysteresis when stresses grow too large, or when improperly assembled

- Typically are restricted to motions of around a hundredth of the length of the flexure, due to fatigue and hysteresis considerations

- Typically have a large volume compared to the extent of their motions

- Exhibit poor dynamic performance especially when several flexure stages are stacked in series, due to flexures behaving as springs

- Can exhibit buckling instability with compressive loads

- Nonlinear force-deflection relationships with larger deflections

A more thorough discussion of the advantages and disadvantages of flexures can be found in the introductory chapter to Smith's book on flexures [1] as well as Howell's book on compliant mechanisms [2]. The buckling instability disadvantage listed above represents the focus of this work: in this thesis compressive loadings are deliberately added to exploit a unique behavior in flexural bearings as they approach elastic instability. As compressive loading is added, the stiffness of the flexure is reduced in the direction in which it will ultimately buckle; such instability is typically detrimental in mechanical systems, but in this work this phenomenon is harnessed to achieve flexures with very low stiffness relative to their uncompressed stiffness. This phenomenon also opens up the possibility of designing flexures with a downwards-tunable stiffness, where the stiffness can be reduced by varying the compression.

1.1.2 Advantages of adding compression

Compressing flexures can change the characteristics of the flexures slightly or drastically depending on the magnitude of the compressive load relative to the flexure's buckling load. Below the buckling load, the effect will be to reduce the flexure's stiffness in the direction it would buckle. Compressions with a magnitude higher than the buckling load can cause the flexures to become a bistable mechanism, which as a machine element is distinct from the uncompressed flexure and has its own set of engineering applications.

1.1.3 Importance of this work

Several potential applications were described in section D of U.S. patent 0132088 awarded to researchers at the Charles Stark Draper Laboratory [3] and are summarized here and further discussed in §1.3.1. Compressed flexures have the potential to be used in a variety of sensors such as accelerometers, precision scales, seismometers, vibrometers and displacement sensors. They can also replace conventional flexures if it is necessary to increase the sensitivity of the instrument the flexure is guiding.

In addition, they are used to guide the motion of actuators, such as force coils, with very low stiffness in one direction and high stiffness in other directions. Conventional flexures have the problem that their stiffness tends to be high relative to the amount of force available to the actuator, even in the low-stiffness direction. The actuator must exert a certain amount of force to deform the flexures; the actuator force that deforms the flexures would not be available to actuate whatever system the force coil is coupled to.

1.1.3.1 Advantages over serial flexures

Compressed flexures present a new area of design possibilities by enabling an increase in compliance in a desired direction by one or more orders of magnitude without significantly increasing the footprint of the flexural bearing or modifying the stiffness in other directions; this is not possible with conventional flexures. For a conventional flexure, to increase compliance by a factor of 10 would require that the flexure lengths be approximately doubled, and this length increase also increases the flexure's compliance in the out-of-plane direction.

When flexural bearings are combined in series, the degrees of freedom of the complete assembly are the union of the degrees of freedom of the two individual flexural bearings. This is typically done to achieve degrees of freedom not possible or feasible with individual flexures, and also to reduce the stiffness of the flexure. A classic example of increasing flexure compliance by stacking flexural stages is the double-parallelogram flexure. With this arrangement it is possible to double flexure compliance without increasing the footprint, at the cost of increased complexity, dynamic performance and machining cost.

1.1.3.2 Expanding the engineer's toolkit

A mechanical element that behaves as a spring with tunable stiffness represents a new basic machine element that in the hands of creative engineers will find many uses that have yet to be considered by the author of this work. To be able to design hardware with compressed flexures, the engineers should know under what conditions a compressed flexural element behaves as an ideal spring with tunable stiffness and should understand what the engineering tradeoffs are when designing with compressed flexures. This thesis aims to find and document

those conditions and tradeoffs so that compressed flexures may be more easily utilized by other engineers who are not flexure specialists.

1.1.3.3 A new class of devices

One of the traits of flexural bearings is that they tend to take up a large volume compared to the amount of motion they allow because of range restrictions due to hysteresis and fatigue considerations. Consider a simple flexural bearing which is a cantilevered beam. The deflection at the tip will be

$$\delta_{tip} = \frac{FL^3}{3EI} \tag{1.1}$$

The maximum stress in the beam will limit the ultimate deflection; the maximum stress in the beam can be calculated as

$$\sigma_{max} = \frac{M_{max}y}{I} = \frac{F_{max}L}{bt^2} \tag{1.2}$$

The maximum stress in the beam is typically taken to be some fraction of the material's yield stress to avoid fatigue failure or hysteresis due to plasticity. Plugging in F_{max} from (1.2) into the expression for δ_{max} in (1.1) yields

$$\delta_{max} \propto \frac{1}{b}\frac{L^2}{t} \sigma_y n \tag{1.3}$$

with n as the anti-fatigue or hysteresis factor, typically around 0.1 to 0.3. Of note is that the maximum allowed displacement is proportional to the square of the length and inversely proportional to the beam depth and thickness. The beam thickness and depth are typically constrained by manufacturing limitations, an out-of-plane stiffness requirement, and buckling resistance requirements.

24

If instead a compressed-flexure system is implemented and the compliance is increased by a factor of 1000 by adding compression, the length of the system can be reduced by a factor of 100 (though not exactly, since a compressed flexure system will also have an increase in stress – some adjustment must be made to correct for this). Such size reduction could allow for flexural bearing miniaturization and allow them to be designed in applications where they were previously precluded due to their size.

1.1.3.4   Effect on the overall size of flexural bearings

It has been observed throughout the course of experimentation that the stiffness of the flexure can be reduced by an order of magnitude. The Draper patent presents the possibility of a reduction of between three and four orders of magnitude. The stiffness of a cantilevered beam is inversely proportional to the cube of its length. Suppose a flexural bearing has length L and stiffness k; a compressed flexure with a stiffness reduction of one order of magnitude can be substituted. Assuming the required stiffness is k, the length of the new compressed flexure could be reduced to $\frac{1}{10}L$ while still maintaining the stiffness k. If a flexure stage with characteristic area L^2 is replaced with compressed flexures with length $\frac{1}{10}L$ the occupied area could potentially be reduced by a factor of 100. One of the major disadvantages of conventional flexures is that the physical space the bearings occupy tends to be large compared to the amount of motion they provide; with compressed flexures, this disadvantage is mitigated.

1.1.3.5   Increase in design flexibility

With the exception of some specialized couplings such as those offered by Helical, flexural bearings typically cannot be bought off-the-shelf as can be other mechanical elements

25

such as screws or springs, and so are usually designed for a specific application. They must be designed with high attention to detail or else the flexure may fail in a variety of ways. The designer must carefully design the geometry of the flexures to meet design requirements for stiffnesses in one or more degrees of freedom, overall size, temperature stability, all while ensuring that the stresses in the flexures are small enough to avoid hysteresis and a premature failure due to fatigue. Once the flexural bearing is designed, machined, and installed, the mechanical characteristics (such as stiffness) of the flexures cannot be changed as they are inherent in the geometry of the flexures. If it is later discovered in the field that the stiffness of the flexure needs to be changed, a new flexure would have to be designed, machined and installed. A flexure with an adjustable stiffness would avoid costly redesigns by allowing stiffness adjustments in the field; a compressed flexure could achieve reductions in stiffness, while adding tension can increase stiffness.

1.1.3.6   Preventing rupture in brittle flexures

In general, brittle materials such as silicon are much stronger in compression than they are in tension. Typically in MEMS devices, micromachined silicon is used for mechanical elements such as beams, and beam elements experience simultaneous compression and tension while bending. The part of the micromachined beam in tension will fail before the beam segment in compression does; with the addition of a compressive preload it is possible that the net compressive load allows for an increase in the usable range of the brittle flexure before rupture. In a bending beam without any preload, one side of the beam will be under tension and the other side will be under compression. With the application of a compressive preload on the beam it is possible to reduce or even eliminate the tensile load. In an IEEE paper Yoder et al   recognized

26

that semiconductor wafers are sometimes damaged during processing due to imposed bending loads, hurting profitability; the researchers investigate the possibility of adding a net compressive strain to increase the strength of the wafer in bending [4]. Such techniques could also be used to extend the usable range of existing MEMS flexural bearings.

1.1.4 Impact of this work

1.1.4.1 Accelerometer design

A typical accelerometer is composed of a spring-mass-dashpot system; acceleration is indirectly measured by measuring the displacement of a proof mass against a calibrated spring.
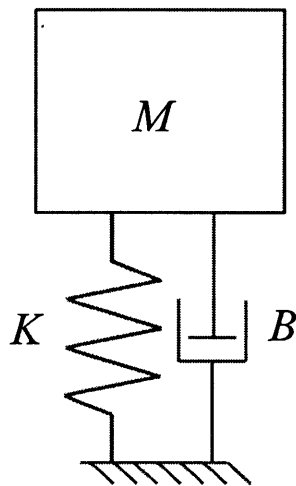
Figure 1.2: Schematic of a simple accelerometer.
Inertial loads produce a measurable displacement of the proof mass.

By combining Newton's law of accelerations with Hooke's law,

$$F = ma \qquad (1.4)$$

$$F = kx \qquad (1.5)$$

27

$$a = \frac{k}{m}x \qquad\qquad (1.6)$$

it is shown that the acceleration is directly proportional to the spring stiffness and inversely proportional to the proof mass. If a smaller acceleration is to be measured, the proof mass must be increased or the spring stiffness must be decreased. However, the general drive for miniaturization directly conflicts with increasing the size of the proof mass; decreasing the stiffness of the spring is possible with the introduction of compressed flexures. A typical micromachined MEMS accelerometer is supported by silicon cantilever beams; the stiffness of such a beam is inversely proportional to L^3 where L is the length of the cantilever beam. If it is desired to decrease the stiffness of the cantilever beam by a factor C, then the length of the flexures must increase by a factor of $\sqrt[3]{C}$. However, increasing the length of the cantilever springs also conflicts with the drive to miniaturize. It can be seen then that if smaller sensors with improved mechanical acceleration sensitivity are to be developed, then a technological leap is required; reducing flexure stiffness by the conventional manner of increasing the flexure beam length can only be tolerated for so long before miniaturization forces another approach. The technology discussed in this thesis presents such an innovation that could decrease the stiffness of the cantilever springs by a factor of between 10 and 10,000, with a proportional increase in acceleration sensitivity and reduction in overall size.

1.1.4.2   A mechanical displacement divider

By taking advantage of the fact that the flexure stiffness can be changed with the compressive load it is possible to design a mechanical transmission using a fixed spring and a variable spring (the compressed flexure). If there are two springs in series, where one of the

28

springs is a compressed flexure and one of the springs is a conventional spring with fixed stiffness, such as a Belleville, coil spring, or another flexure, the following analysis can be performed.
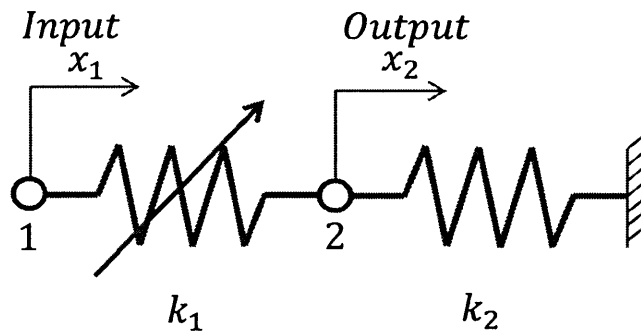
Figure 1.3: Schematic of a displacement divider with a tunable stiffness spring.

If a displacement x_1 is applied at node 1 and recognizing that the forces on both springs must be equal to satisfy equilibrium, the displacement at the output can be written as

$$x_2 = x_1 \frac{k_1}{k_1 + k_2} \tag{1.7}$$

By varying the ratio of the two spring rates it is possible to achieve different transmission ratios. Such a device could be useful when applying displacement inputs to micro-scale devices with inexpensive larger-scale manipulators, such as screws. An application would be adjustment of optics where submicron adjustments need to be made(Figure 1.4); a mechanical displacement divider could divide the input from a micrometer screw between an adjustable spring and a fixed spring and reduce the input displacement of the micrometer by a factor of 10 or 100 to achieve submicron positioning capability.

29
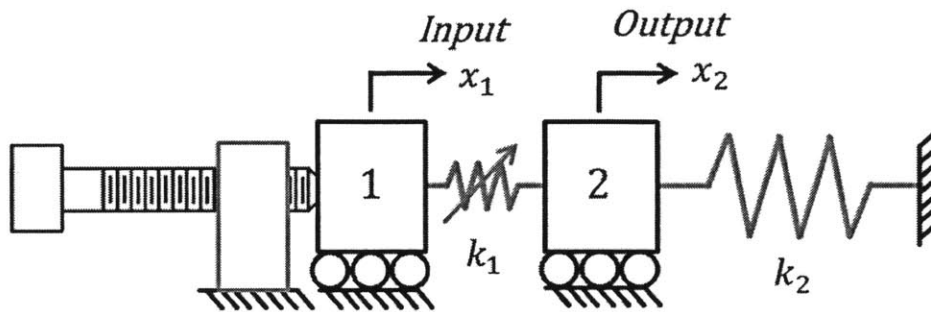
Figure 1.4: A displacement divider application.

A manual actuator such as a screw is used to apply a displacement to an input stage; the displacement of the output stage is a fraction of that of the input stage.

1.2 Potential Risks

In a precision system it is considered good practice to keep the amount of energy stored as low as possible to prevent this energy from manifesting in undesirable ways; for example, in designing a flexural bearing, one would strive to minimize the strain energy. When designing compressed flexures, more strain energy is being added to the system when compared to uncompressed flexures; one of the dangers inherent in this is that the additional strain energy can cause the flexure to relieve some of this energy by deforming in undesired manners. For example, when compressing a beam-column, the beam can minimize its energy by bowing out to the side instead of remaining straight, as will be discussed in §2.4. One of the goals of this thesis is to explore the effects of this energy addition to what would otherwise be a precision system (a one degree of freedom stage supported by flexural bearings).

1.3 Prior art

Changing the stiffness of a beam-column by way of adding compression is a technique that has existed for at least several decades, since around 1950 when researchers noted that the natural frequency of a hinged bar would change with axial loading [5]. Several more recent investigations into the area are described in the following subsections. None of these sources provide detailed guidelines for designing compressed flexures.

1.3.1 CSDL patent

U.S. Patent 0132088 [3] awarded to researchers at the Charles Stark Draper Laboratory (CSDL) describes an accelerometer design whose key feature is a flexural suspension composed of compressed flexures which reduce the suspension's stiffness in the sense direction by a minimum factor of 100 and as high a reduction factor as 10,000.
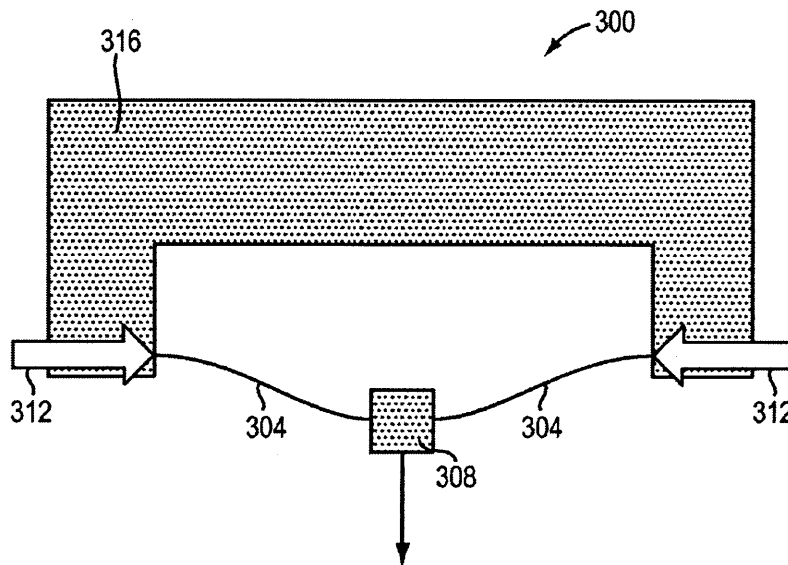
Figure 1.5: Compressed flexure accelerometer concept from CSDL patent 0132088 [3]

A key feature of the accelerometer is that there is very low flexure stiffness in the sense direction, and very high stiffness in all other directions. The CSDL team defines "zero stiffness" to be at least 2 orders of magnitude stiffness reduction from the unstressed configuration, and preferably 3 or 4 orders of magnitude. They also define "high stiffness" to be 2 orders of magnitude higher than the unstressed stiffness of the sensing suspension flexures.

Several methods of achieving the flexure compression are described:

- The frame and flexures are made of materials with different CTEs; changing the ambient temperature will change the compression

- Frame and flexures are same CTE, but the frame has a pre-stretch and clamps down on the flexures

- Mechanical forcing mechanisms adjust the compression of the flexures

- Flexures have a film of material deposited with different CTE during manufacturing; cooling causes compression due to CTE mismatch

Another feature discussed in the patent is using an actuator as a spring with a stiffness negative of that of the suspension; in this way, the flexure stiffness is cancelled and the net effect is a proof mass with zero stiffness. The actuator, with the addition of feedback and a suitable controller, could be used to cancel out error motions due to manufacturing or eccentric loading.

In addition, the Draper researchers describe a mechanism with zero rotational stiffness in addition to the zero linear stiffness. Mechanical elements with very low rotational stiffness are outside the scope of this paper but could be a future topic of research.

This thesis builds upon the work done of the Draper researchers by investigating in depth the behavior of flexures in response to compression and understanding barriers to compressed flexure performance, such as limited stiffness reduction ability. The patent shows several

32

potential uses for compressed flexures but does not provide detailed guidelines for their design; this thesis seeks to fill that knowledge gap and providing engineers with design rules.

1.3.2 Low frequency vibration isolators

Researchers at the NASA Langley Research center faced the design task of attenuating very low frequency signals (<10 Hz); their solution was to design several passive Zero-Spring-Rate mechanisms. In a paper discussing the design of a vibration isolator with a zero-stiffness suspension [6], three different designs of a low-frequency vibration attenuator were presented and tested. The designs used beam-columns with compression added mechanically either via a piezo actuator or a differential set screw. The researchers were able to reduce the stiffness of the springs by more than an order of magnitude.

In another NASA paper describing the design of a low-stiffness suspension for a low-frequency vibration isolator [7], researchers propose a design for a Zero-Spring-Rate-Mechanism (ZSRM) based on superimposing flexures near their buckling load with a negative stiffness with a conventional spring with a positive stiffness, the net sum being close to zero. It is a passive mechanism. The researchers determine that the initial imperfections initiate nonlinear behavior, which ultimately limits performance of the ZSRM. Such a mechanism would be used to replace a previous suspension mechanism consisting of long lengths of cables; lower-stiffness suspensions required excessively long cable lengths relative to the space available in the testing facilities. The researchers conclude that the buckled beams in the zero-stiffness mechanism are sensitive to imperfections.

The NASA researchers focus on the task of low-frequency vibration isolation; most of their modeling pertains to the dynamic response of the compressed flexures. This thesis works to

33

broaden the applications for compressed flexures as well as establishing design rules for static and quasi-static behavior.

1.3.3 Bistable MEMS microbeams

A bistable beam mechanism is similar to a compressed flexure in that the compression is enough to cause buckling in the beam such that it remains in one of two equilibrium positions. Given the right conditions, a compressed flexure will become a bistable mechanism; in certain applications, this bistable postbuckling behavior can be advantageous. In a paper discussing the use of bistable beams as nonvolatile memory storage elements [8], Hälg discusses modeling the bistable elements as beams undergoing simultaneous compression and bending with the equilibrium state of the beam being found by minimizing the strain energy stored in the beam. Fang and Wickert discuss in-depth the post-buckling behavior of the microbeams and include the effect of initial imperfection on the postbuckling behavior [9]. It is possible that a designer may have need of a mechanical element that behaves as a linear spring but at times will require bistable behavior; a compressed flexure element would be able to switch between the two modes of operation based on the amount of compression.

Despite both being based on the same mechanical element, a compressed flexure, the pre-buckling and post-buckling behavior of compressed flexures are entirely different. Fang and Wickert for example focus on the effects of initial imperfections on postbuckling behavior; in this thesis the effect of initial imperfections on prebuckling behavior are studied. This thesis focuses entirely on the pre-buckling behavior of compressed flexures and fills a knowledge gap left by the post-buckling researchers.

1.3.4 Comparison of compressed flexures with similar technologies

It is hypothesized that the compressed flexure can replace conventional flexures in certain applications; comparisons between the two different machine elements are summarized based on several criteria Table 1.1, with compressed flexures being compared to conventional flexures based on several criteria..

Table 1.1: Comparison of compressed flexures and other precision bearing technolgoies

Technology	Cost	Stiffness	Design flexibility	Longevity	Footprint
Conventional flexures					
Compressed flexures	Higher	Much lower	Higher	Lower	Smaller

The cost is higher for the compressed flexures as they require additional design effort and additional hardware for preloading. The stiffness of the compressed flexure can be lower than the uncompressed flexure by one or more orders of magnitude. The ability to tune the stiffness grants the compressed flexure greater design flexibility. The longevity of compressed flexures is expected to be lower due to the higher stresses involved. The footprint of compressed flexures is smaller than that of conventional flexures as discussed in §1.1.3.4.

1.4 Thesis Scope

In this thesis "tunable stiffness flexures" refers to flexural bearings which are arranged to constrain a motion stage to move in a single degree of freedom; these flexures will have compression applied along their axes to decrease their stiffness along the motion stage's degree

of freedom. While it is also possible to increase flexure stiffness by adding tension instead of compression, this will be outside the scope of the thesis, as the behavior of interest for the funding agency lies within reducing the stiffness of flexural bearings.

The objectives of this work are to:

1. Generate models to predict tunable stiffness flexure behavior

2. Generate guidelines for designing tunable stiffness flexures; delineate tradeoffs that must be made when implementing compressed flexures

3. Quantify limitations to the stiffness-reducing behavior; characterize the change in stiffness of a test set of flexural bearings, comparing the stiffness with that of the developed model

4. Quantify the degree to which other degrees of freedom are influenced by the compression. Measure the motions in six degrees of freedom of a test stage guided by compressed flexures, and compare the parasitic motions with the desired output motion.

1.5 Thesis summary

The first chapter of this thesis has been a discussion on the motivation behind this work, as well as a summary of similar work done by other researchers, and a summary of the work done in this thesis. Chapter 2: Background discusses the background material necessary for developing the buckling models used in this thesis; this includes simple Euler buckling, buckling with initial imperfections, and energy-minimization based modeling to relate input displacements and transverse displacements to stiffnesses. Chapter 3: Modeling discusses how a set of

compressed flexures can be modeled as individually buckled beams. Chapter 4: Experimental

Design details the design of the test flexure and the test setup to evaluate the performance of the

compressed flexural bearings which guide the test stage. The design of the each module in the

test setup is discussed. Chapter 5: Results and Discussion discusses the experimental procedures

used to collect data and the experimental results obtained from various experiments. Chapter 6:

Summary and Future Work recaps the work done in this thesis and discusses possible future

areas of research to further develop compressed flexural bearings.

(this page intentionally left blank)

2

BACKGROUND

In this section column buckling is briefly reviewed with models of increasing complexity, beginning with a description of ideal Euler column buckling modes and restrictions on when buckling can be considered to be Euler buckling. Deviations from ideal Euler buckling conditions by introducing initial geometric imperfections in the column are discussed. The effect of compression on in-plane and out-of-plane stiffness is covered in this section as well.

2.1 Euler buckling

The Euler buckling formula encapsulates a complex instability phenomenon into a simple formula relating the critical compressive buckling load to beam geometry, material properties and boundary conditions; the tradeoff for this simple model is that several conditions must be met for buckling to be considered Euler buckling [10].

1. The beam is assumed to be perfectly straight

2. The compressive load is assumed to be applied centrally

3. The beam is assumed to behave perfectly elastically; e.g., the stresses in the beam do not exceed the material's proportional limit

4. The bar remains straight, undergoing perfect compression until the critical

   buckling load is reached

A beam which meets these criteria will buckle elastically when

$$P_{cr} = \frac{\pi^2 EI}{(KL)^2}$$
(2.1)

where K is a coefficient that depends on the boundary conditions and varies from 0.5 for

a beam with both ends built-in and 2.0 for a beam with one free end and one built-in end. Values

for other end conditions are given in Table 2.1.

Table 2.1: Effective length coefficients for Euler column buckling with various end conditions

End conditions	K
Pinned-Pinned	1
Fixed-Fixed	0.5
Fixed-Guided	1
Fixed-Free	2
Fixed-Pinned	0.707

Solving for the Euler buckling load of a column typically consists of writing the fourth-

order differential equation of the beam's shape,

$$\frac{d^4y}{dx^4} + k^2\frac{d^2y}{dx^2} = 0, \quad k = \sqrt{\frac{P}{EI}}$$
(2.2)

a differential equation whose general solution is known to be of the form

$$y(x) = A\cos kx + B\cos kx + Cx + D \qquad (2.3)$$

Four boundary conditions are required to obtain a system of four equations with four unknowns. One solution technique is to assemble these equations into a matrix and set the determinant of the matrix equal to zero; this will yield a transcendental equation whose solutions correspond to buckling loads. For example, a beam that is built in on both sides will have the transcendental equation

$$z\sin(z) - \cos^2(z) + 2\cos(z) - \sin^2(z) - 1 = 0, \qquad z = kl \qquad (2.4)$$

The first three solutions of this equation are

$$z_1 = 2\pi, \qquad z_2 = 2.86\pi, \qquad z_3 = 4\pi \qquad (2.5)$$

Figure 2.1 shows the first three buckling modes of a doubly-clamped beam as obtained through a SolidWorks Simulation buckling finite-element analysis. The buckling loads are also given, and normalized with respect to the fundamental buckling load.

For engineering applications, typically the first solution is the most relevant, as it represents the lowest compressive load for which the column will become unstable and fail; higher modes are irrelevant beyond the lowest buckling load because the beam has already collapsed. The higher buckling modes are only possible if the column is constrained from buckling in the lower modes, if for example the clamped-clamped buckled beam in Figure 2.1(a) was prevented from displacing at its midsection and its compression was increased it would buckle as in Figure 2.1(b). If the beam was not allowed to displace at its midsection, and also not allowed to rotate at its midsection, and the compressive loading was further increased, it would

41

buckle as in Figure 2.1(c).
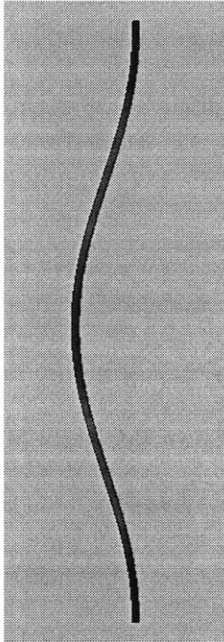
$$P_1 = 4\pi^2 \frac{EI}{L^2} \qquad\qquad P_2 = 8.18\pi^2 \frac{EI}{L^2} = 2.05P_1 \qquad\qquad P_3 = 16\pi^2 \frac{EI}{L^2} = 4P_1$$
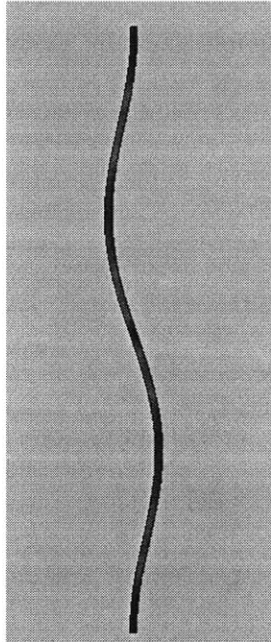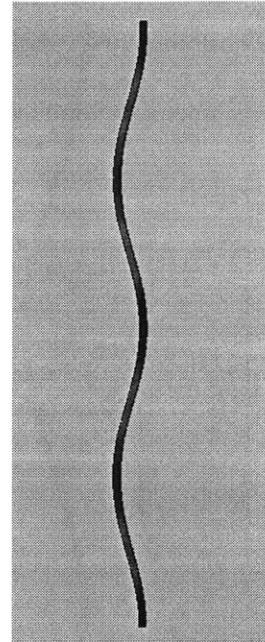
(a) (b) (c)

Figure 2.1: First three buckling modes of a doubly built-in column and their relation to the fundamental buckling mode.

(a) Fundamental mode, (b) Second mode (anti-symmetric), (c) Third mode (symmetric)

Note that the relationship between the buckling mode and the fundamental buckling load is not linear, i.e., the third buckling load is not three times the fundamental load, $P_3 \neq 3P_1$. For a clamped-clamped beam, the fundamental buckling mode is

$$P_1 = 4\pi^2 \frac{EI}{L^2} \tag{2.6}$$

42

2.2 Euler buckling slenderness constraints

From experience with common items such as yardsticks or business cards, engineers intuitively know that a column which is very long compared to its thickness will not fail by crushing; when compressed it will buckle and bow out to the side and will immediately restore itself after the load has been removed. In contrast, the engineer also knows that a thick, short beam or column will not buckle. Short and stout beams will instead "squash" or "crush", failing by plastic deformation (Figure 2.2).
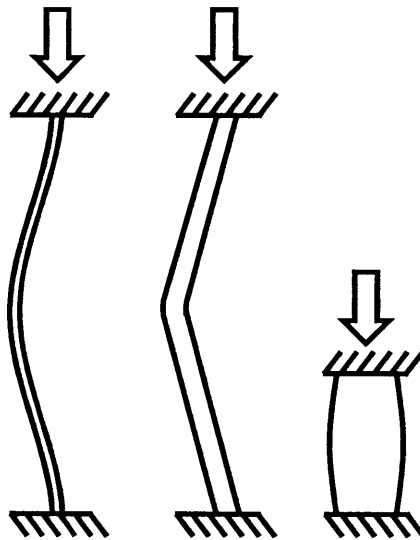
Figure 2.2: Effect of slenderness on buckling.
From left to right: A slender column undergoing Euler buckling, a thicker column undergoing intermediate buckling, and a stocky column being crushed plastically

It is of particular interest to know in advance what geometric, material, and loading parameters will result in a beam which buckles or a beam which crushes. In the traditional civil engineering application, this was important because a beam that buckled would have a much smaller carrying capacity than the carrying capacity predicted by its crushing strength, therefore

the engineer would apply a generous safety factor to ensure that the beam parameters were nowhere near the Euler buckling regime. This problem has been investigated by a multitude of researchers at the beginning of the 20th century; prior to the advent of aeronautics, engineers tended to shy away from slender columns altogether. The growth of the aeronautical industry created a demand for ever-lighter, ever-stronger structures – this demand gave impetus to research in engineering techniques for designing slender compression members and the conditions under which they would fail [11]. Timoshenko and Gere [10] present a discussion on the effect of inelasticity and buckling; a summary of their discussion follows.

The application discussed in this work differs from that of the civil engineers, in that civil engineers avoid the Euler buckling regime with healthy safety factors, whereas in designing compressed flexures the opposite is done; a beam-column is designed that will buckle in a purely elastic Euler manner (it should be noted here that Euler buckling implies elastic behavior) and avoids any plasticity effects, which are undesirable in flexural bearings as plasticity leads to output motion hysteresis. Much work has been done in the 20th century regarding the transition region between pure crushing and Euler buckling; however, this transition regime is beyond the scope of this thesis, as in this work the focus will be on designing beam columns that buckle elastically. In this thesis a healthy safety factor is applied to keep the compressed flexures in the Euler regime, just as civil engineers apply such safety factors to keep their columns out of buckling.

A column is assumed to have a rectangular cross section, and that deformations are small compared to the beam thickness (the usual Euler-Bernoulli beam bending assumptions). Furthermore it is assumed that the beam is undergoing simultaneous axial loading and bending.

44

With the Euler assumption that the beam remains straight before buckling, the stress can be written as

$$\sigma_{cr} = \frac{P_{cr}}{A} \qquad (2.7)$$

This can be rewritten in terms of the dimensionless slenderness ratio λ, and combining with the critical Euler load for a clamped-clamped column we obtain

$$\sigma_{cr} = \frac{4\pi^2 E}{\lambda^2} \qquad (2.8)$$

which itself is defined in terms of the length and radius of gyration as

$$\lambda = \frac{l}{r} \qquad (2.9)$$

where the radius of gyration is defined as

$$r = \sqrt{\frac{I}{A}} \qquad (2.10)$$

Rewriting the critical stress in this manner enables use of the dimensionless slenderness ratio that encapsulates important information about the beam's geometry and can be used to design columns accordingly. For designing compressed flexures, it is desired to completely avoid any inelastic effects because these will contribute to hysteresis in the motion of whatever the flexures are guiding. So long as the critical buckling stress remains well below the material's proportional limit, there should be no inelastic effects in the beam. If Eq. (2.8) is rewritten to replace σ_{cr} with σ_y, that is, if the stress in the column that causes buckling is also the same stress that causes yielding, a critical slenderness ratio λ_{cr} can be found that defines the threshold

45

between Euler buckling and the intermediate buckling which involves both plastic and elastic effects.

$$\lambda_{cr} = 2\pi \sqrt{\frac{E}{\sigma_y}} \qquad (2.11)$$

This expression for λ_{cr} is interesting in that it is independent of geometry; it is dependent only on the ratio of the elastic modulus to the yield strength. This means that depending on the hardness condition of a material, the beam could buckle in different regimes. For example, two columns, one made of hardened steel and the other made of the same steel without the hardening could exhibit different buckling behaviors.

Unfortunately there is a complication here due to the fact that the proportional limit is not defined for all materials, or that is difficult to find data for. It can also vary depending on the material's hardness condition; the yield strength of the material is more commonly used by engineers, as it is much more commonly available. Aluminum is problematic in that due to its microstructure it does not have a clearly defined proportional limit, so another approach is to use the 0.2% offset yield stress and applying a healthy safety factor. To avoid hysteresis in aluminum, Slocum recommends going no higher than around 10% to 30% of the material's yield strength [12].

2.3   Effect of initial imperfections

During the course of experimentation it was found that the behavior of the buckling flexure beams was significantly different from the behavior predicted by Euler, whose derivations were described in §2.1. The simple Euler model assumes that the beam is perfectly

46

straight, and remains straight during loading. In reality this is not the case; there will exist in the beam some curvature due to geometric imperfections from manufacturing and/or curvature induced due to eccentric loading. With eccentric column loading, the loading does not go directly through the beam-columns central axis. The buckling behavior that will be observed will not be the perfect bifurcation predicted with the Euler theory, where the beam stays perfectly straight until the load P_{cr} is attained, and the beam only moves laterally after the critical load is achieved. What will be observed with initial imperfections is that the beam starts to deflect out to the side as soon as any column compression is added and that this deflection is amplified with additional compression.

There are two types of imperfections which can affect the buckling behavior – eccentric loading and initial column curvatures. In an eccentric loading condition, as in Figure 2.3(a), the column loading is applied off-center, introducing an additional moment which must be accounted for in the moment-curvature relation. With initial geometric imperfection, as in Figure 2.3(b), an additional moment must be added due to the initial shape causing internal reaction moments.
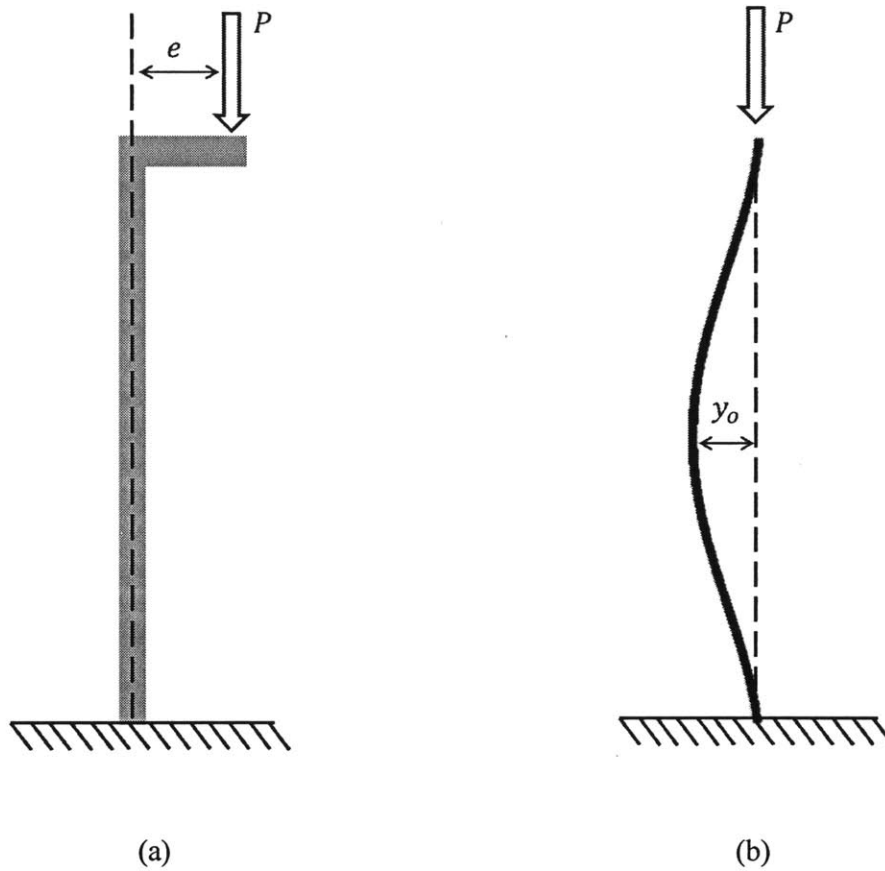
Figure 2.3: Imperfect conditions which affect buckling behavior.
(a) eccentric column loading and (b) pre-existing geometric shape

In this thesis columns with built-in ends are used (zero displacement and zero slope at the ends), therefore eccentric loadings have no effect; if the ends of the column are not allowed to rotate, a load applied off-center will have no effect different from a load applied directly to the column's centroid [10]. Therefore, discussion will be restricted to a column having an initial curvature, whose shape matches that of the first buckling mode.

The derivation for the midspan deflection vs. the input preload is derived here as in Jones [13], but modified for a doubly built-in beam (or clamped-clamped) rather than a clamped-pinned beam. The derivation begins with the moment-curvature relation

48

$$EI\frac{d^2y}{dx^2} = M \tag{2.12}$$

It is recognized that the deflection of the beam $y(x)$ can be broken up into two parts: that which exists due to initial geometric imperfections $y_i(x)$, and deflection that results from loading the column, $y_t(x)$. The beam moment $M(x)$ can be found by sectioning the beam and applying equilibrium. (2.22) can be rewritten as

$$EI\frac{d^2}{dx^2}[y_t(x)] = M_o - P[y_t(x) + y_i(x)] \tag{2.13}$$

Note that $y_o(x)$ does not appear on the left hand side of (2.13); this is because y_o requires no moment to exist [13]. An assumption must be made for the initial shape of the beam $y_i(x)$. Jones argues that choosing an initial imperfection in the shape of the first buckling mode represents a worst-case scenario, since one could argue that such an initial imperfection would mean that the column is already buckled. For a clamped-clamped beam, the chosen initial imperfection function is

$$y_i(x) = -\frac{y_o}{2}\left(\cos\left(\frac{2\pi}{L}x\right) - 1\right) \tag{2.14}$$

This choice of initial imperfection allows the midspan deflection to be specified by a parameter y_o. By applying the boundary conditions for a clamped-clamped beam and using the method of undetermined coefficients, (2.13) can be solved and simplified to

$$EI\frac{d^2}{dx^2}[y_t(x)] = M_o - P[y_t(x) + y_o(x)] \tag{2.15}$$

After simplification, the midspan deflection can be written as

49

$$\delta_t = y_o \left(\frac{1}{1 - \frac{P}{P_E}} \right)$$
(2.16)

Where δ_t is the midspan deflection of the column, P is the input compressive loading and

P_E is the critical compressive load. This can be nondimensionalized by dividing by the column

thickness t, yielding

$$\frac{\delta_t}{t} = \frac{1}{c} \left(\frac{1}{1 - \frac{P}{P_E}} \right)$$
(2.17)

Where a parameter c has been introduced to represent the magnitude of the initial

imperfection relative to the column thickness; a smaller c value means that the imperfection is

large; a c value of one implies that the initial imperfection at the midspan is one beam thickness.

Higher c-values represent more 'perfect' beam, with the initial imperfection being smaller

compared to the column thickness. It can be seen that smaller values of the initial imperfection

cause the column to approach ideal Euler buckling: zero lateral displacements for all loads less

than the critical buckling load, with an indeterminate transverse deflection at the buckling load

(represented by a vertical line at P_{cr}).

Nondimensional midspan displacement vs. nondimensional force
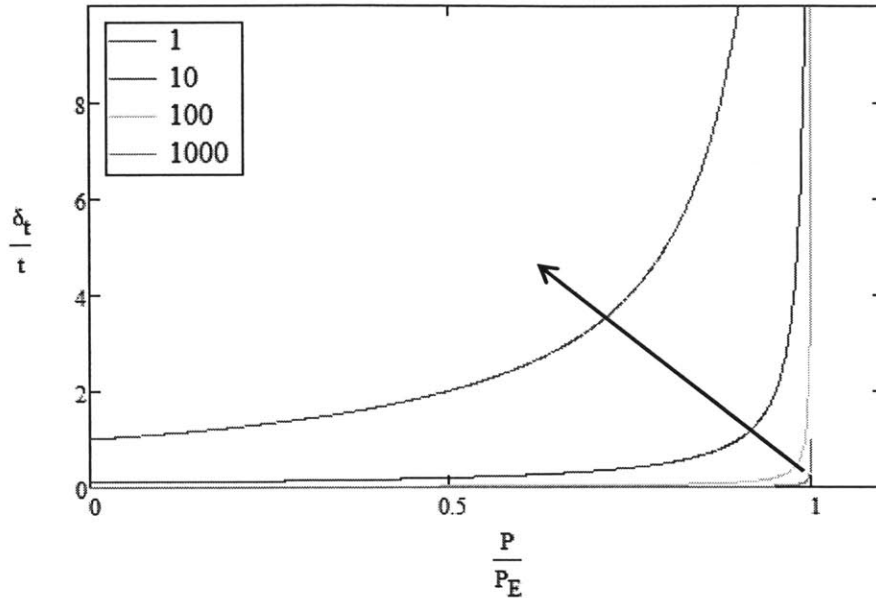
Figure 2.4: Effect of initial imperfection on the transverse-displacement-force curve.
The arrow indicates the direction of larger initial imperfection; ideal Euler buckling would
have zero midspan translation until the Euler buckling load is reached.

2.4 Effect of compression on in-plane stiffness

Assuming that the compressed flexures are designed to buckle in a particular direction, that is if $\frac{b}{t}$ is at least 10 (see Figure 2.5) which in turn implies that $\frac{I_2}{I_1} = 100$, beam deflection formulas from a source such as Roark's [11] can be used to predict the transverse stiffness vs. the input preload.

51
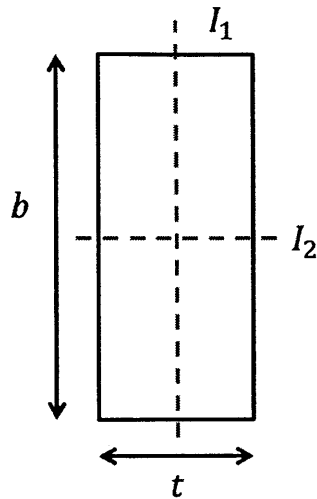
Figure 2.5: Cross section of a compressed flexure beam.
The beam will buckle in the direction of smaller moment of inertia I. A beam of
square or circular cross section could buckle in either direction.

Roark's lists formulas for the deflection of a beam in response to various types of

loadings and end conditions. The stiffness of a compressed flexure could be modeled from the

midspan deflection of a clamped-clamped beam undergoing simultaneous compression and

bending, with the beam load at the midspan.
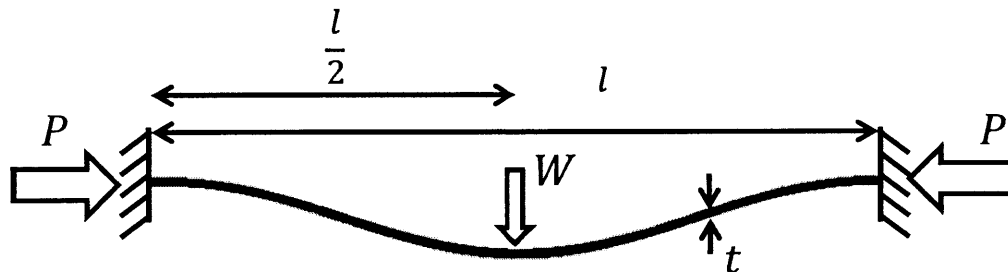
Figure 2.6: Clamped-clamped beam used for stiffness vs preload model

Under these conditions, the deflection at the midspan is given by

$$y_{max} = -\frac{W}{kP}\left(\tan\left(\frac{kl}{4}\right) - \frac{kl}{4}\right), \quad k = \sqrt{\frac{P}{EI}} \tag{2.18}$$

The stiffness K of the beam in bending can be computed as the force divided by the displacement, or

$$K = \frac{W}{y_{max}} = -\frac{kP}{\left(\tan\left(\frac{kl}{4}\right) - \frac{kl}{4}\right)} \tag{2.19}$$

This can be expanded about $P = 0$ using a Taylor expansion to obtain

$$K_{lin}(P) = \frac{192EI}{l^3} - \frac{24}{5l}P \tag{2.20}$$

The first term in (2.20) is identical to the stiffness of a clamped-clamped beam without any compression. The function $k(P)$ and $k_{lin}(P)$ are plotted below in Figure 2.7 using parameters for the test flexures used in this thesis. The first-order linearized model almost perfectly matches the actual trigonometric expression; an engineer could use (2.20) to design a tunable stiffness flexure, since this expression is much simpler and offers more intuition than the trigonometric form (2.19).

53
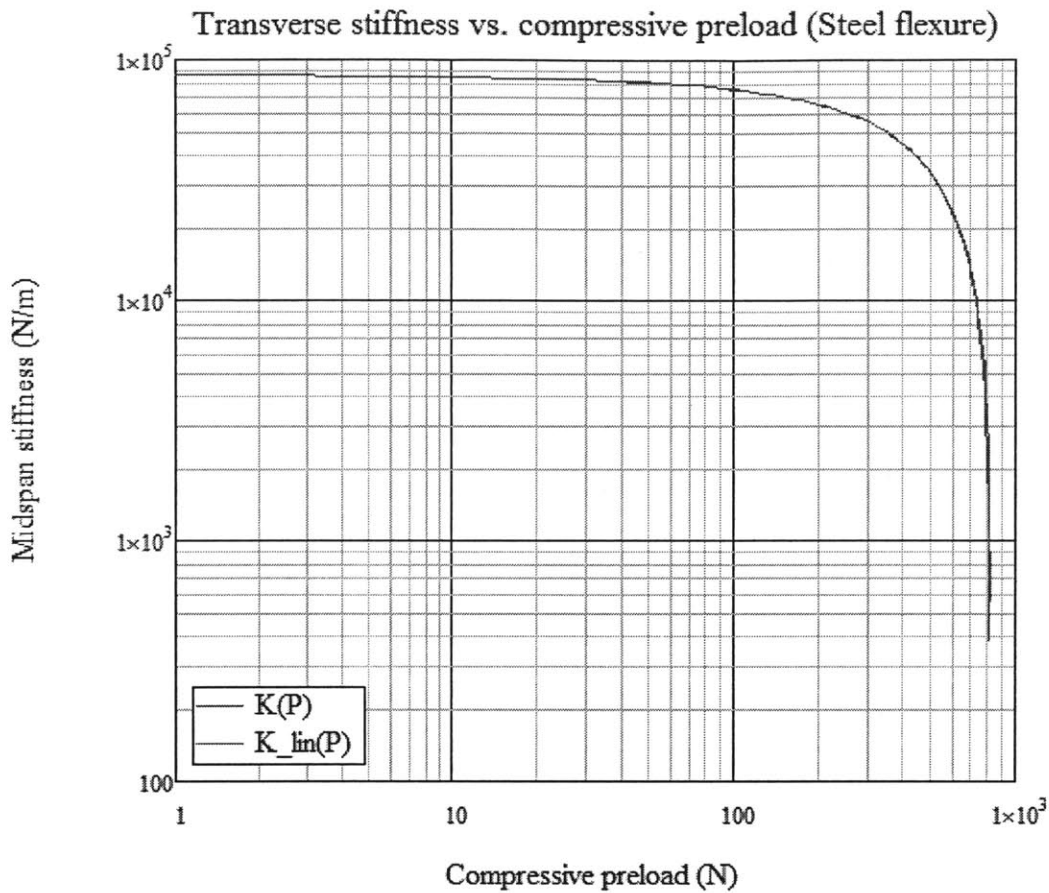
Figure 2.7: Stiffness vs preload model based on beam-column formulas from Roark's.
The linear approximation appears to match the trigonometric expression; plotting the data differently proves otherwise.

It is difficult to see the error between the linearization and the exact function from this log-log plot; therefore the linearization error is plotted in Figure 2.8 as a percentage against the nondimensional load, normalized to the critical buckling load. The linearization error reaches -5% at a dimensionless load of 0.83, -10% at 0.9, and -20% at 0.95.
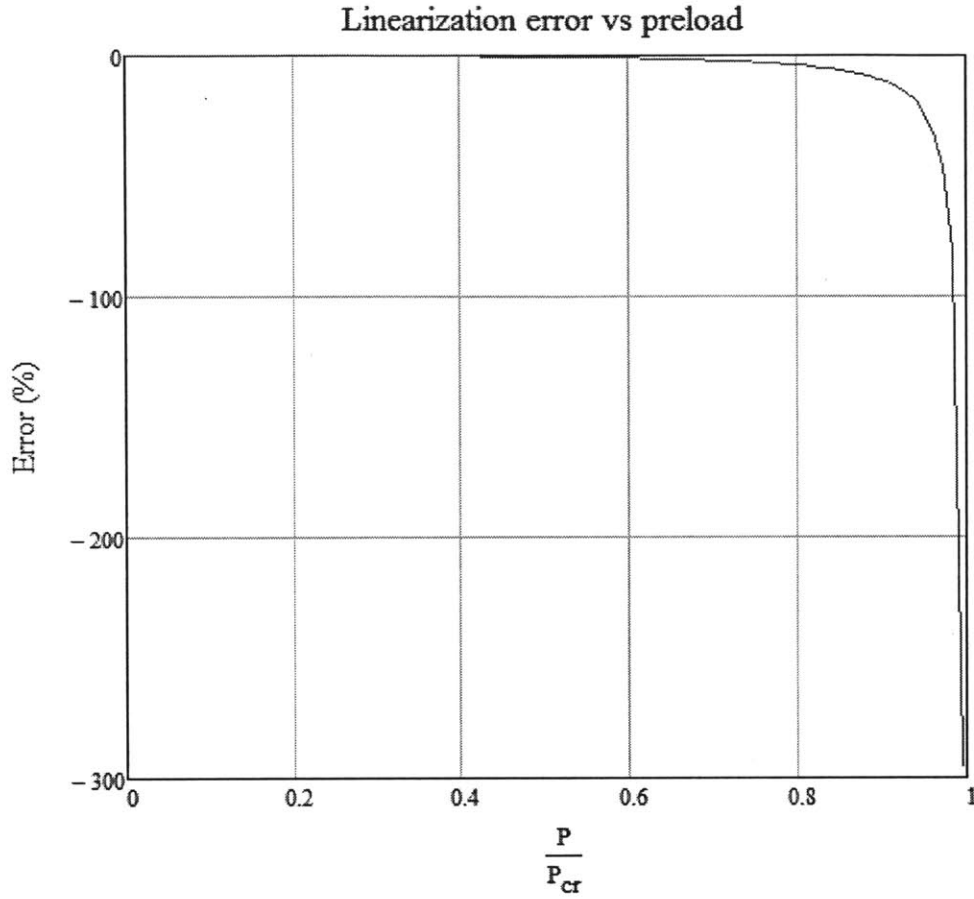
Figure 2.8: Linearization error plotted vs. compressive preload.
The linear approximation remains within 5% of the theoretical value for the first 80% of the tuning range.

In the range where the linear approximation remains accurate to within 5% of the exact value, the stiffness changes by approximately a factor of five. Eq. (2.21) can also be written in terms of the input column compression Δ using the relations developed in §3.5,

$$K_{lin}(\Delta) = \frac{192EI}{l^3} - \frac{24}{5}\frac{EA}{l^2}\Delta \qquad (2.21)$$

55

2.5 Effect of compression on out-of-plane stiffness

The out-of-plane stiffness as a function of preload can be computed in the out-of-plane direction exactly as it was computed for the in-plane stiffness as in §2.4, the main difference being that the beam tension factor $k = \sqrt{\frac{P}{EI}}$ will be different due to a different moment of inertia. The overall shape of the curve will look exactly the same as for the in-plane stiffness, except that the buckling asymptote will occur at a much higher load. For the flexure parameters used in this thesis, the critical buckling load in the out of plane direction is higher than the in-plane direction by a factor of 360. In Figure 2.9 from the no-preload stiffness to where the flexure buckles in-plane, the out of plane stiffness changes by 0.2%.
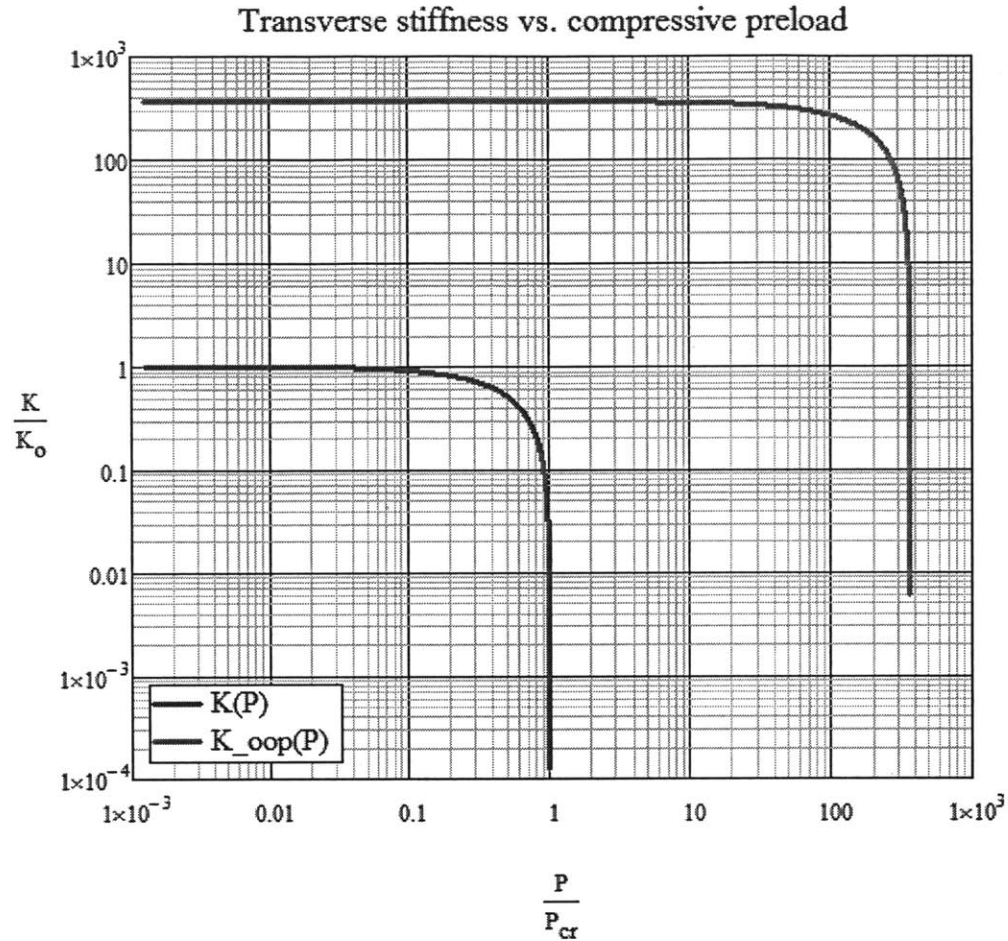
Figure 2.9: Plot of in-plane and out-of-plane stiffnesses.
Each buckling load is normalized against the critical buckling load for the in-plane direction, and each in-plane stiffness is normalized against the in-plane stiffness before compression.

2.6 Stiffness modeling via strain energy minimization

The Euler model does not provide a method for calculating lateral displacements; it assumes that the beam remains perfectly straight, and once buckling occurs, the lateral displacement is indeterminate. In the proposed application it is of interest to be able to characterize the lateral load-displacement relationship in order to obtain a stiffness value, and to observe how this stiffness changes with axial compression. It is therefore necessary to develop a

model that can predict the stiffness behavior based on initial design parameters such as beam geometry, material, and boundary conditions. Here is discussed a stronger model based on strain energies that relates the input displacement to the transverse displacement by assuming the beam takes on a certain shape which is free to change its amplitude, and that the correct amplitude for this assumed shape can be calculated by minimizing the strain energy from the input displacement and bending energy from to the transverse displacement. This model also takes into account initial imperfections by assuming an initial mid-span displacement y_o.

The modeling is begun by assuming a shape function for the flexure, preferably one that satisfies the boundary conditions of a clamped-clamped beam. The shape function must have zero deflection and zero slope at the top and bottom; furthermore, it should be smooth. A cosine curve fits these requirements. The curve is also given a degree of freedom via the parameter a, which will be used to find the energy-minimizing shape of the beam for a given input displacement.

$$y(x, a) = a y_o \left(\frac{1}{2} cos \left(\frac{2\pi}{L} x \right) + \frac{1}{2} \right) \qquad (2.22)$$

where y_o represents the initial imperfection, and a is a factor that allows the beam shape to change in response to the input loading. The strain energy due to bending and compression is then calculated, given an input displacement compression Δ; this strain energy function is then minimized with respect to a to find the value of a that corresponds to the input Δ. This is implemented in the MathCAD worksheet in the digital supplement file

`stiffness_modeling_via_strain_energy_minimization.xmcd`. The stiffness vs. preload curves predicted by the model are plotted in (Figure 2.10). The model based on the Roark's equations is also plotted, as well as two sets of Finite Element Analysis data from

58

SolidWorks Simulation. The 'linFEA' curve represents the linear-elastic simulation, which does not take into account large-deformation behavior. The 'nFEA' curve, which consists of fewer data points due to the greatly increased computation time, does take into account large displacement behavior and applies the load in a series of loadings. For an imperfection of 1 μm, which represents an initial imperfection that is 500 times smaller than the flexure thickness, the imperfect model and the Roark's model collapse together (they cannot be seen apart in the figure). The linear elastic FEA separates from the other models for larger preloads, and the non-linear FEA stays close to the ideal models predicted by the Roark-based formula and 1 μm imperfection energy model.
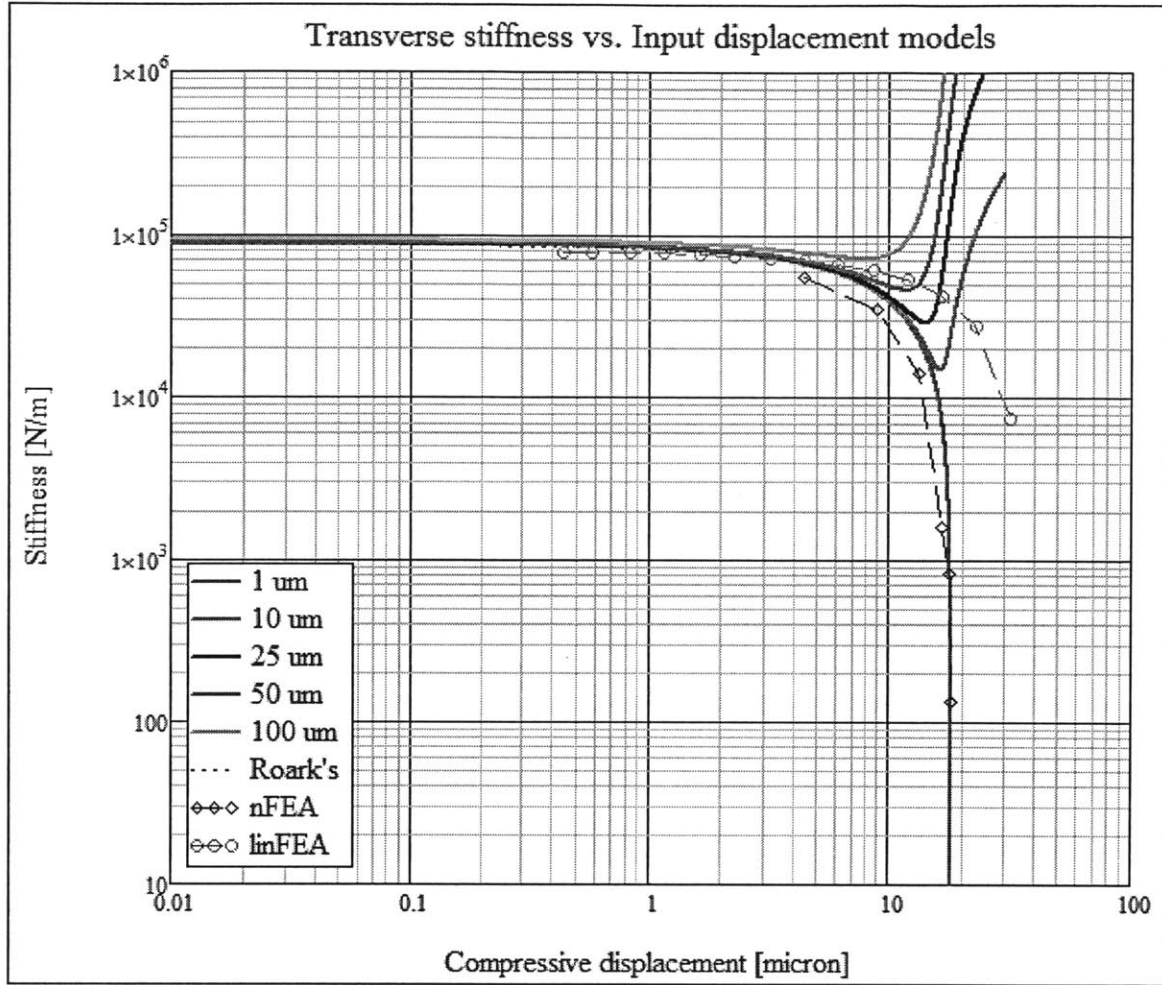
Figure 2.10: Plot showing the different compressed flexure models.

The first five lines are from the strain-energy-minimizing model with different initial imperfections. The Roark's solution cannot be distinguished from the $1 \mu m$ curve. A non-linear FEA predicts behavior close to ideal. The linear FEA diverges from the other models at higher preloads.

2.7 Beam-column stresses

For a beam undergoing bending without any added compression, the stress in the beam can be written as

$$\sigma(x,c) = \frac{M(x)c}{I} \qquad (2.23)$$

where I is the moment of inertia of the beam, $M(x)$ is the moment in the beam, and c is the distance from the neutral axis at a given x position. Since I is a constant, the greatest stresses will be found when M and c are largest.

To find the stress in a beam-column we use superposition to find that the stress is a combination of the compressive stress and the bending stress,

$$\sigma(x,c) = \frac{P}{A} \pm \frac{M(x,P)\,c}{I} \qquad (2.24)$$

The complication here is that now the moment in the beam is a function of the compressive load P. Roark's Formulas for Stress and Strain [11] contains solutions to the beam-column problem.

$$M_{max} = \frac{W}{2k} tan\left(\frac{kl}{4}\right), \quad k = \sqrt{\frac{P}{EI}} \qquad (2.25)$$
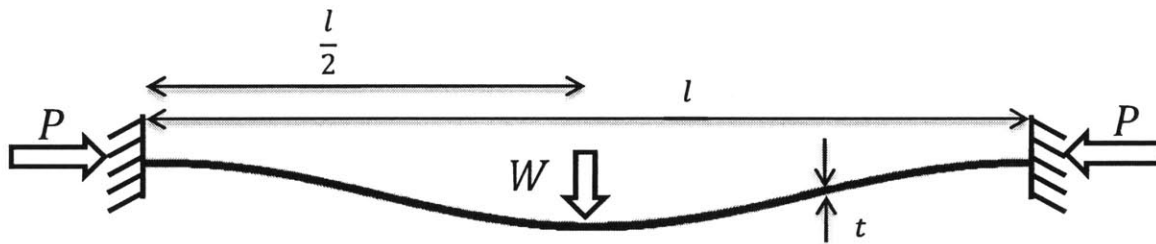
Figure 2.11: Diagram of a beam-column model used for calculating stresses

Plugging this into (2.24) gives the expression for the maximum stress in the beam

$$\sigma_{max} = \frac{EI}{A}k^2 \pm \frac{tW}{4k} tan\left(\frac{kl}{4}\right) \qquad (2.26)$$

61

The stress is dependent on both the beam load W and the column load P (which is in the k factor), which makes predicting maximum stresses more difficult. This function be can plotted as a two-dimensional surface plot in Figure 2.12. This model is suitable for a beam-column that is initially straight and is deflecting small amounts. A stronger model is needed to take into account beam-columns that have an initial imperfection; this initial imperfection introduces a moment due to the compression, which causes the imperfection to grow, which then increases the moment further; this runaway-effect induces a stress multiplier on the compressive load in the beam, as will be discussed in the next section.

Max stress vs compressive and transverse loading
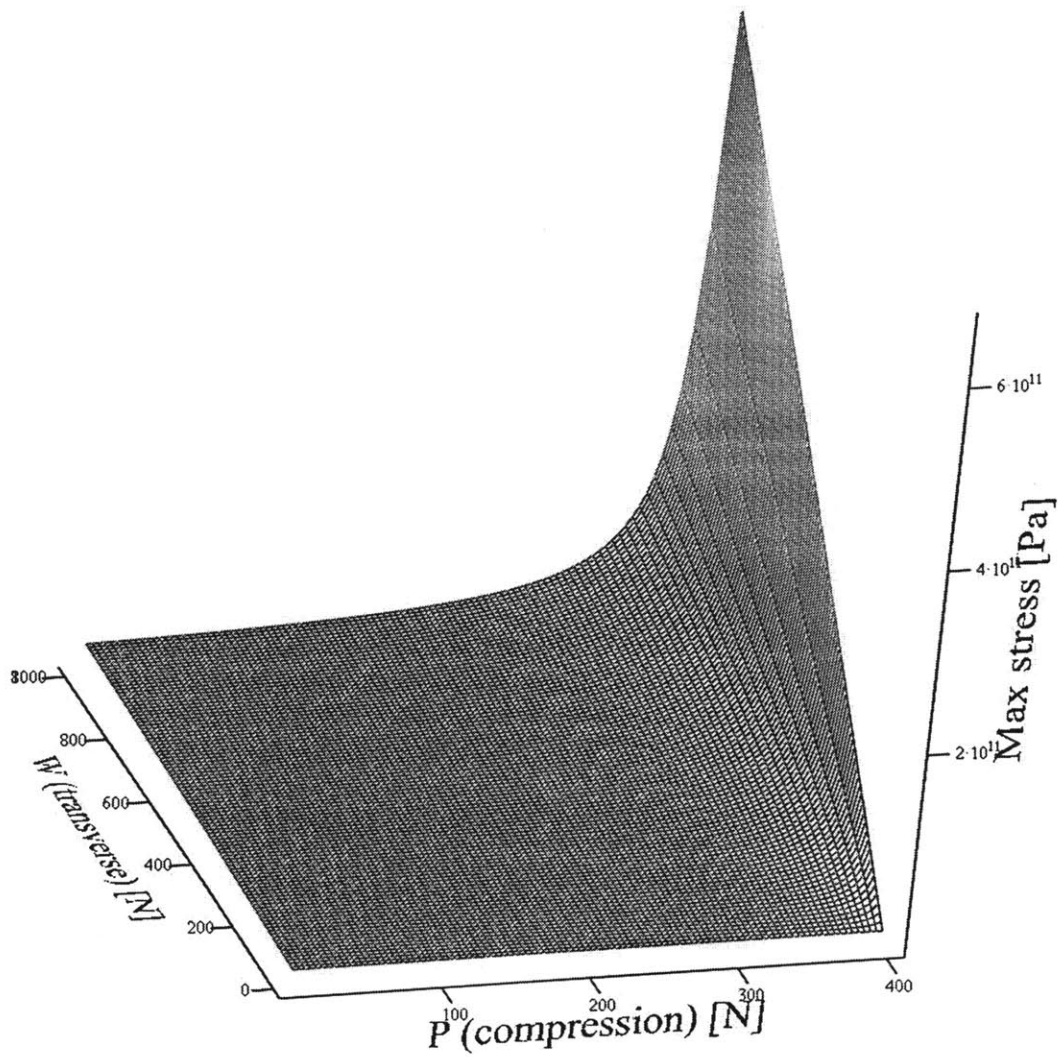
Figure 2.12: Maximum beam column stress as a function of input compression P and transverse loading W.

The buckling load grows excessively high when there is a combination of both transverse loading and buckling (here the Euler buckling load is approximately 417 N

2.8 Stresses in a beam column with initial imperfection

Jones [13] discusses the effect of an initial imperfection on the stresses in the beam-column. By combining the results of §2.3, the lateral deflection of an imperfect column caused by compressive loading, with the stress relation in §2.7, he arrives at the following formula

$$\sigma_{max} = \frac{P}{A}\left(1 + \frac{1}{1-\alpha}\frac{6a}{t}\right), \quad \alpha = \frac{P}{P_E} \tag{2.27}$$

where a is the initial imperfection, t is the thickness of the beam, P_E is the Euler buckling load, and P is the compressive load. The stress in the beam is the compressive stress $\frac{P}{A}$ times a multiplier that depends on the ratio of the compressive load to the Euler buckling load; as the compressive load approaches the buckling load, the stress could potentially diverge. The initial imperfection a controls how fast this grows; if a is zero, there is no initial imperfection and the only stress will be the compressive stress $\frac{P}{A}$.

CHAPTER

3

MODELING

As is always the case in engineering there is a tradeoff to be made when building models between model accuracy and model complexity. The ideal model would be able to capture all of the relevant model physics and make good predictions about the system's behavior while remaining mathematically tractable. However, it is not always possible to maintain a model's mathematical tractability especially as a system's complexity increases. In some physical systems, models can quickly become complex enough so that only a numerical solution is possible, thus denying the engineer the insight that can be gained from an analytical solution. A good model should provide design insight and make useful predictions without burdening the designer with excess computation.

3.1 Model idealization

The flexural bearings described in this thesis are not composed of a single column under compression – in order to provide adequate constraint for the experiments, and to be useful for engineering applications, it was determined for reasons that will be discussed in §4.2 that a minimum of four flexure would be used, which corresponds to four beam columns (Figure 3.1).

65

The challenge is to decide how to apply the buckling theory explained in §2 and developed for single-column buckling to this more complex arrangement of flexures.
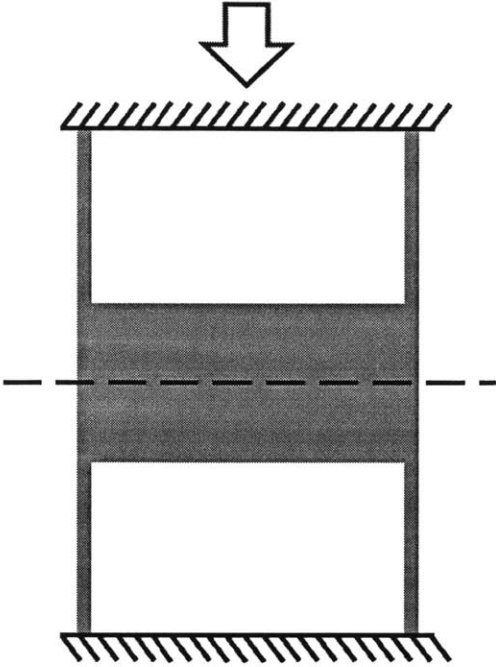
Figure 3.1: The compressed flexure layout that will be the focus of modeling efforts.
This flexure arrangement allows for motion of the central stage along the dashed line.

As will be described in §4.2, a monolithic flexure was designed and manufactured out of a single plate of material; monolithic flexures avoid many problems that can arise from a built-up assembly of flexures, such as the effects of misalignment introduced during assembly and improperly designed or assembled bolted joints.

To use the simple Euler buckling equations, two major simplifications must be shown to be reasonable:

- The central beam connecting the two columns does not significantly alter the buckling load from the buckling load calculated for each column alone

- The thickened central portion of the beam can be ignored from the Euler buckling load

66

The former is discussed in section 3.2, and the latter is discussed in section 3.3.

3.2   Buckling of a rigid sway frame

The simplest models for column buckling are for a single column under compression; however, the test flexure is unfortunately not so simple. The test flexure is considered to be two columns joined together at the midsection with equal loadings. Timoshenko and Gere [10]
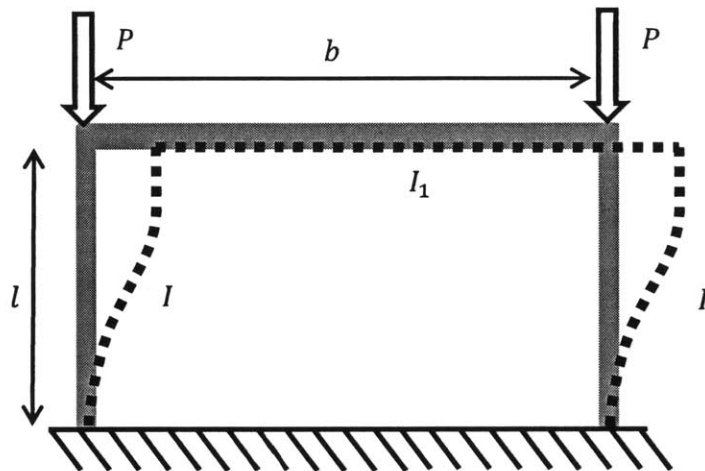
Figure 3.2: A rigid sway frame deforming after being loaded

provide an analysis for a similar structure known in civil engineering as a "rigid sway frame". It is "rigid" because all of the interconnections are joined together 'rigidly' rather than pinned (in this case, it is rigid because it is a monolithic structure, but in civil engineering it could be a welded structure), and it is a "sway" frame because it is allowed to move laterally instead of being fixed in position.

A sway frame such as that depicted in Figure 3.2 is, due to symmetry, equivalent to half the column assembly shown in Figure 3.1**Error! Reference source not found.**. Timoshenko and Gere solve for the buckling load by writing the moment-curvature differential equation for the

individual beam sections; they obtain equation (3.1) which they then use to calculate the

buckling loads.

$$\frac{kl}{tan(kl)} = -\frac{6l}{b}\frac{I_1}{I}$$
(3.1)

If the rigidity of the central beam is higher than the rigidity of the beam-columns by at least a

factor of 100, then the right hand side grows large and the solution is

$$P_{cr} = \frac{\pi^2 EI}{l^2}$$
(3.2)

which is the same buckling load for a single fixed-guided beam. If the central beam is very

compliant, the solution goes to zero and the critical buckling load becomes

$$P_{cr} = \frac{\pi^2 EI}{4l^2}$$
(3.3)

which is the same buckling load as that of a fixed-free beam. It appears to be the case that the

central section only changes the buckling load from these two cases when the rigidity of the

central beam approaches that of the columns; otherwise, the buckling loads are calculated by

treating each column independently and ignoring the central section.
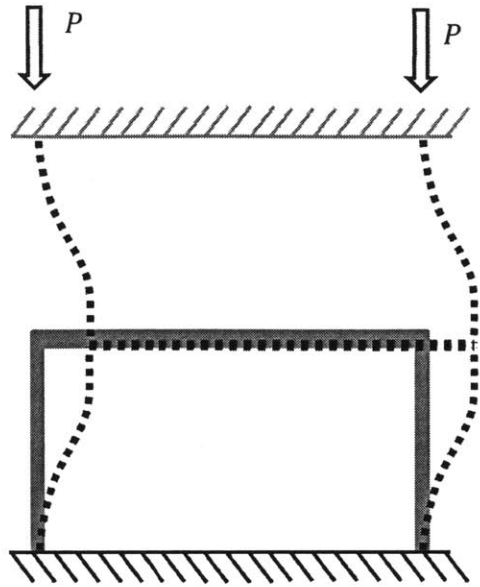
Figure 3.3: Symmetric sway frame model of experimental flexure.

The buckling load P is identical to that of a single fixed-fixed beam, if the rigidity of the central section is larger than the beam column rigidity by a factor of at least 100

3.3 Buckling of a column with step changes in cross-section

The buckling load of a stepped column with stepwise changes in cross section can be computed by applying the moment-curvature differential equation to each beam section and matching boundary conditions at each interface. Analysis will be restricted to a beam-column with stepwise changes in cross-section (no tapering columns, for example). It is further assumed that two of the sections, the top and bottom columns, are identical and of the same length (Figure 3.4), and that the beam-column is symmetric about the mid-plane (represented by a dashed line in Figure 3.4). The beam is also assumed to be made of a single material and that the depths of each section are identical.
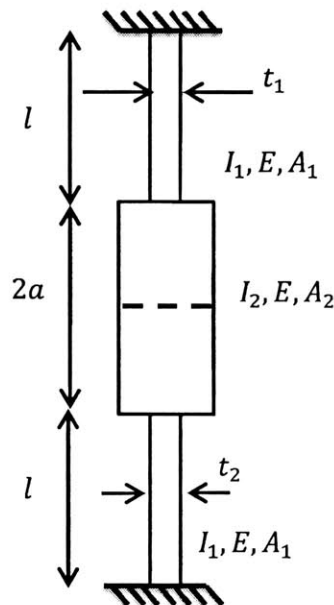
Figure 3.4: Symmetric stepped column buckling model.

The Euler moment-curvature relation can be applied to each section; additional constraints are that the beam must be continuous, that the beam slope must be continuous, and that the internal moment and shear are continuous. The general solution of the moment-curvature differential equation in each of the three sections is

$$y(x) = A \cos kx + B \cos kx + Cx + D \qquad (3.4)$$

where $k = \sqrt{\dfrac{P}{EI}}$ is the beam tension factor and is different for the narrow and thick beam sections, since the moment of inertia I changes.

With three column sections, this results in a system of 12 equations with 12 unknowns. Four boundary conditions are given by the displacement and slope conditions at the top and bottom of the column; eight additional conditions are obtained by matching the position, slope, moment and shear at each column interface. This system of equations can be assembled into a 12 by 12 matrix; setting the determinant of this matrix equal to zero gives the equation that must be solved to find the buckling loads. Finding the determinant of a 12 by 12 matrix symbolically was not possible for MathCAD to compute; therefore a numerical solution was found instead using the parameters in Table 3.2, which are the beam parameters of the test flexure used.

Table 3.2: Beam parameters used in numeric stepped column solver

Parameter	Value used	Description
l	$0.023\ m$	Thin section length
E	$220\ GPa$	Elastic modulus, plane strain, steel
t_1	$0.5\ mm$	Flexure thickness
t_2	$10\ mm$	Thick section thickness
a	$15\ mm$	Half-length of thick section
b	$9.53\ mm$	Beam depth

When using these values, the ratio of I_2 to I_1 is 8000. The result of the numeric solver is a buckling load of 370.2 N. Comparing this to the computed Euler buckling load using the same parameters but ignoring the thick section,

$$P_{cr} = \frac{4\pi^2 E I_1}{(2l)^2} \tag{3.5}$$

gives 370.227 N. The percent error between the Euler load that ignores the thick section, and the stepped column solver solution is 7.3×10^{-3} %, a few thousandths of a percent. Therefore it is concluded that the thick section in the middle of the column does not change the buckling load and the length of the thick section can be ignored from computation of buckling loads.

It is hypothesized that at some value for I_2 the central portion can no longer be neglected, for example when the two sections have the same moment of inertia. The numeric solver is rerun, and I_2 is computed to be some multiple of I_1. The results are summarized in Table 3.3.

Table 3.3: Results of stepped column study for varying moment of inertia ratio

$\dfrac{I_2}{I_1}$	Numeric result [N]	% error from fixed-fixed Euler, Eq. (3.5)
8000	370.2	-7.3×10^3
1000	369.7	-0.143
100	365.4	-1.321
10	321.4	-15.19
1	135.6	-173.0

The last row in Table 3.3 is the special case where the moments of inertia are the same; in this case there is no step change in cross section. The Euler load in this case can be calculated for this beam as

$$P_{cr} = \frac{4\pi^2 E I_1}{(2l + 2a)^2} = 135.63\ N \qquad (3.6)$$

which is a percent error of -0.022% from the numeric solver result. It is concluded from this numeric study that for compressed flexures of the type shown in Figure 3.4 with moment of inertia ratios of greater than 100, the length of the central thickened portion may be ignored from buckling calculations if an error of approximately 1% is acceptable.

3.4 Modeling the experimental flexure

The test flexure is simplified for modeling purposes by assuming that because both columns are displacing by the same amount, they experience the same loads. It is assumed that the mid-section connecting the two columns does not contribute to the buckling load (other than

73

restricting higher buckling modes), as discussed in §3.2, and that the test stage does not change

the buckling load as discussed in §3.3. Therefore, it is possible to calculate the buckling loads for

each column by treating each column independently.
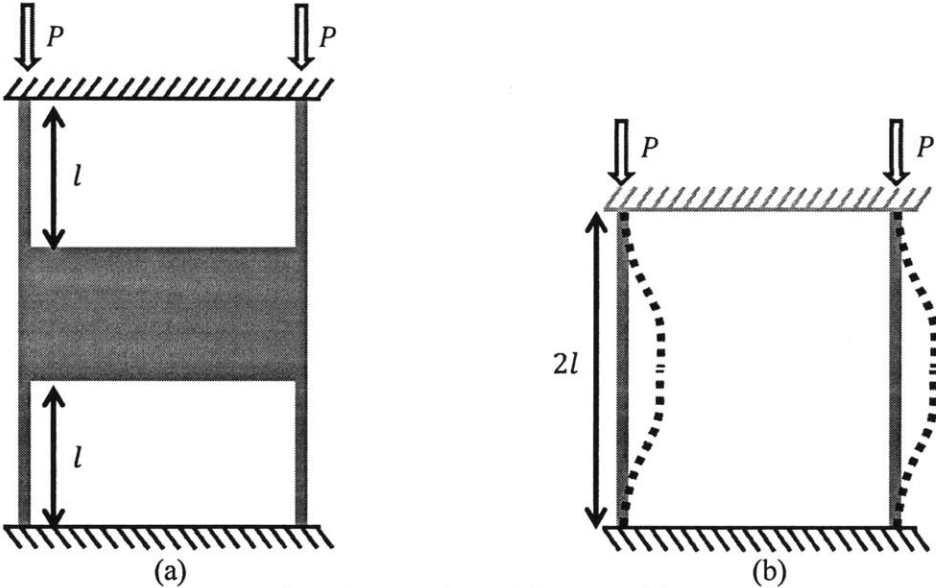
Figure 3.5: Experimental flexure model
(a) before simplifications and (b) after modeling simplifications are made

3.5 Prescribing displacement vs. prescribing forces

In this thesis an experiment is performed where columns are loaded by applying a

displacement. Applying a displacement Δ generates a reaction load P within the columns; this

reaction load can be computed from the uniaxial column relation

$$\Delta = \frac{PL}{EA} \tag{3.7}$$

where L is the column length, E is the elastic modulus, and A is the cross-sectional area. To find

the critical displacement at which buckling would occur, the Euler critical buckling load (2.6) is

substituted into (3.7)

74

$$\Delta_{cr} = \frac{4\pi^2 I}{AL} \tag{3.8}$$

which for a rectangular beam with moment of inertia $I = \frac{1}{12} bt^3$ can be further simplified

to

$$\Delta_{cr} = \frac{\pi^2}{3} \frac{t^2}{L} \tag{3.9}$$

It is interesting to note that the critical displacement for buckling is material independent

and only depends on geometric properties of the column.

When the beam is undergoing simultaneous compression and transverse deflection, some

of the internal reaction load is relieved when the beam bows out to the side. The internal reaction

load P can be computed under these conditions by an approximate method; the shape of the

beam must be approximated. For a clamped-clamped beam, a cosine curve matches the boundary

conditions and is used as an approximation. The midspan deflection is prescribed as δ and the

deflection as a function of position along the beam is given as

$$y(x) = \delta \left(\frac{1}{2} \cos \left(\frac{2\pi}{L} x \right) + \frac{1}{2} \right) \tag{3.10}$$

From the theory of moderately large deflections, the strain of the neutral axis is given by

$$\varepsilon_o = \frac{dU}{dx} + \frac{1}{2} \left(\frac{dy}{dx} \right)^2 \tag{3.11}$$

Integrating this along the length of the beam, substituting $\sigma = \varepsilon_o E = \frac{P}{EA}$, and assuming that the

beam-column's input displacement is $-\Delta$ gives

$$\frac{PL}{EA} = -\Delta + \int_0^L \frac{1}{2} \left(\frac{dy}{dx} \right)^2 dx \tag{3.12}$$

75

With the choice of $y(x)$ given in (2.9), this evaluates to

$$P = \frac{EA}{L}\left(-\Delta + \frac{(\pi\delta)^2}{4L}\right) \tag{3.13}$$

Any transverse deflection will reduce the compressive reaction load P. This relationship can be used to approximate the internal reaction load in the beams when there are moderately large (on the order of the beam thickness) transverse deflections involved. The quantity $\frac{EA}{L}$ can be considered to be the beam-column's stiffness in response to stretching or compressing.

4

EXPERIMENTAL DESIGN

This chapter describes the functional requirements for the experimental setup, the design

of the test flexure, the design of each module within the experimental setup, and the

instrumentation used in the experiment. The test setup with all modules mounted is shown in

Figure 4.1
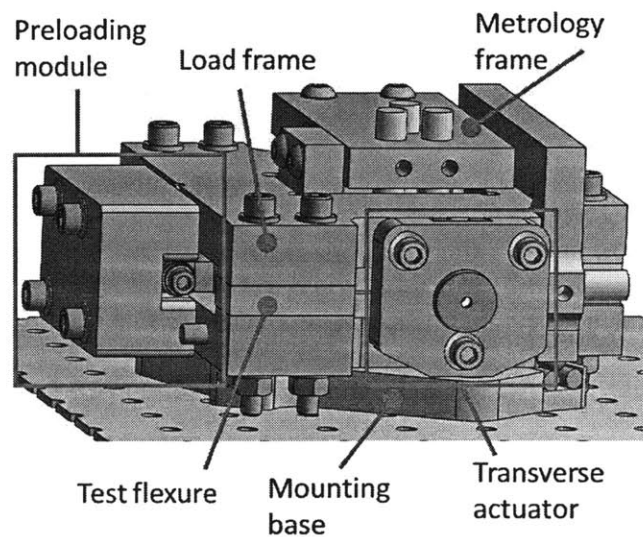
Figure 4.1: Assembled experimental setup with all modules mounted

4.1 Functional Requirements

The overall goals of the thesis as described in the thesis scope in §1.3.4 are to:

1. Generate models to predict tunable stiffness flexure behavior

2. Generate guidelines for designing tunable stiffness flexures; delineate tradeoffs that must be made when implementing compressed flexures

3. Quantify limitations to the stiffness-reducing behavior; characterize the change in stiffness of a test set of flexural bearings, comparing the stiffness with that of the developed model

4. Quantify the degree to which other degrees of freedom are influenced by the compression. Measure the motions in six degrees of freedom of a test stage guided by compressed flexures, and compare the parasitic motions with the desired output motion.

To meet the non-modeling objectives, the following set of design requirements for the experimental setup were developed to test the flexure designed in §4.1. The test setup should

- Measure reduction in stiffness of up to four orders of magnitude, between $100,000 \frac{N}{m}$ down to $10 \frac{N}{m}$

- Measure the motion of a test stage in 6 degrees of freedom with 0.1 μm resolution

- Measure the input displacement with 0.1 μm resolution

- Apply displacements with resolution of at least 0.1 μm, a hundredth of the buckling displacement

- Allow for application of a probing transverse load with a resolution of 0.1 N

Having compressive loads on the order of hundreds of Newtons in the same experimental setup measuring sub-micron displacements complicates the design of the experimental setup; the relatively heavy compressive loads will cause distortion in any parts that are carrying the load, so the experimental setup must be able to withstand these loads without affecting the measurements. Good practice in precision machine design recommends that the metrology frame be decoupled from the load frame – with this decoupling any loads in the structure will not deform the metrology structure [14-15].

4.2 Flexure design

Designing the test flexures required consideration of available sensors and actuators. The test flexure design process is described in the following sections.

4.2.1 Compressed flexure concept

In its simplest manifestation, a compressed flexure could be a cantilevered beam with an applied axial load. The sensor target could be mounted at the tip as shown in Figure 4.2.
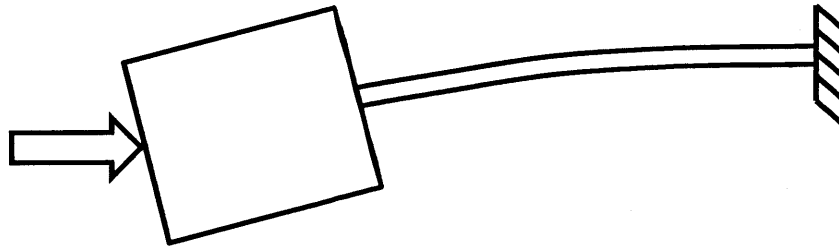
Figure 4.2: Simple compressed flexure beam with test stage at tip

79

However, assuming the sensor target is mounted at the tip of the beam, such a test flexure would be undesirable because this flexure would contain multiple parasitic motions (at least one rotation and translation), and it would be difficult to implement compression due to the combined deflection and rotation of the beam tip. An improvement can be made by applying symmetry and mirroring the cantilevered beam; this eliminates the tip rotation parasitic motion.
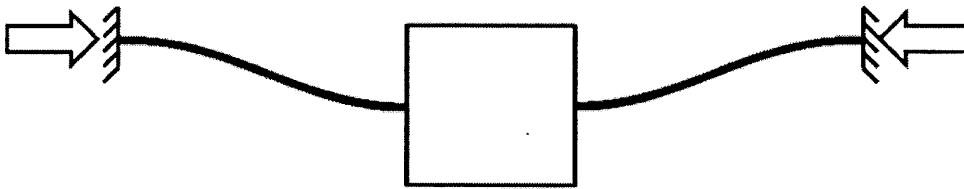
Figure 4.3: Improved compressed flexure test stage eliminates parasitic test stage rotation

This flexure is an improvement, but does not constrain in-plane or out of plane rotations well compared to designs with some improvements. Such an improvement can be made by using two of these modules together to constrain both the in-plane rotation, and the out of plane rotation (assuming that these are blade flexures, not wire flexures).
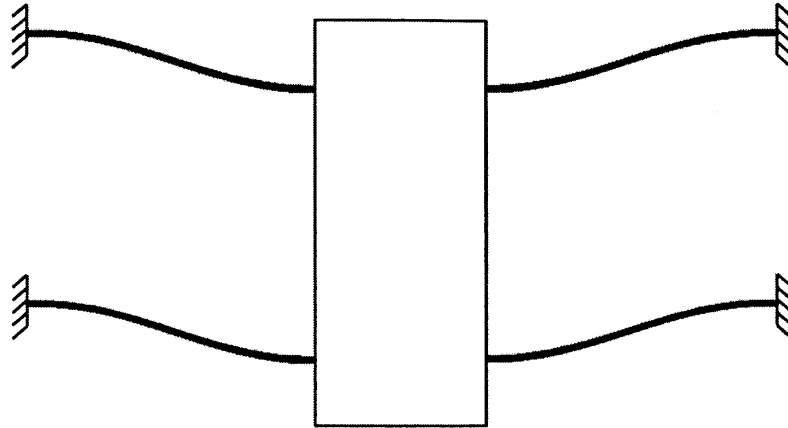
Figure 4.4: Compressed flexure stage which constrains all degrees of freedom except the up-and-down motion of the test stage.

The last problem that remained was to ensure that the inputs to the flexure columns result in pure compression, without any parasitic rotations. As in many flexure-related problems, this problem can be solved by adding more flexures.

4.2.2 Ensuring uniaxial column compression

Regardless of whatever method is used to apply compression to the flexures, the flexure assembly should preferably be designed such that misaligned inputs result only in uniaxial compression for the flexures. To achieve this objective, a secondary stage was designed as part of the flexure assembly (Figure 4.5b).

(a)   (b)
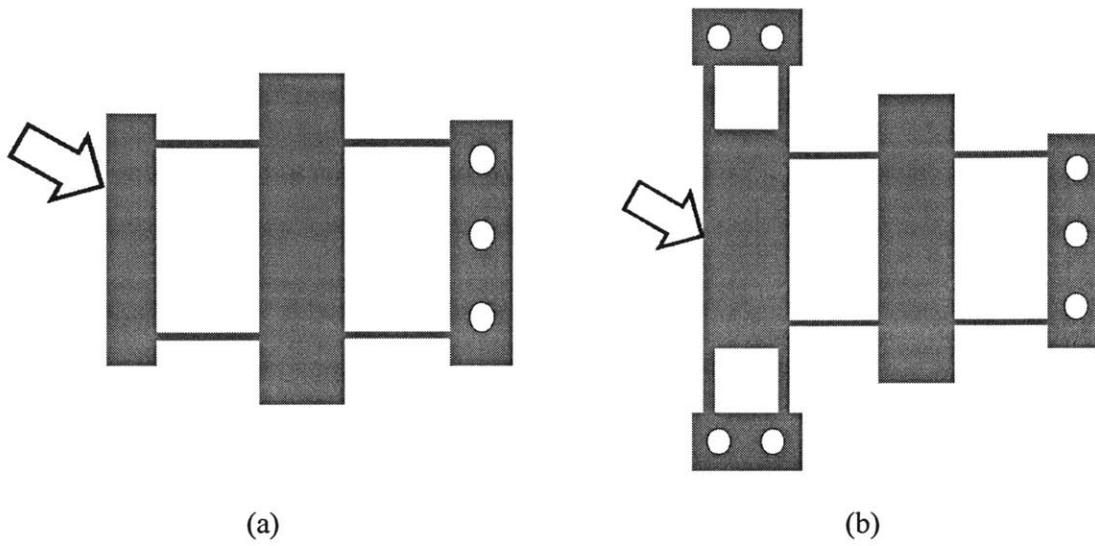
Figure 4.5: Flexure assembly concept
(a) without guidance stage and (b) with guidance stage. For (a) it is assumed that the input block is prevented from moving laterally, otherwise it (and the flexures attached to it) serve no function beyond transmitting the compressive load.

The axial stiffness of the secondary guidance flexures will resist any motion that isn't in the compressive direction; the ratio of the axial stiffness to the bending stiffness in a beam is proportional to $\left(\frac{L}{t}\right)^2$, and a typical beam has a length-to-thickness ratio of around 20. Arranging beams so that they withstand axial loads instead of bending loads thus increases their stiffness by a factor of 400. In Figure 4.5a the force is shown as being in-plane, but it could also have some error such that it has components in an out-of-plane direction; having a pair of guidance flexures on each side allows these out of plane components to be resisted.

At this point, the flexure concept had been generated, but there remained detailed design work to do – in order to proceed with detailing, the metrology had to be considered.

4.2.3 Sensor sizing considerations

The sensor selection is discussed in §4.3; capacitance probes were selected and the test flexure was designed to be used with capacitance probes. The overall size of the flexures was constrained by the size and requirements of the capacitance probes, whose required sensing areas were at minimum a10 mm diameter circle for each sensor. In order to measure rotations, two sensors had to be placed a distance apart and their sensing areas should not overlap; therefore a minimum probe separation width of 10 mm was required. In order to increase resolution to sensing rotations, the probes were given additional spacing beyond the 10 mm minimum whenever reasonably possible.

4.2.4 Flexure material selection

The capacitive sensors require a metallic target in order to sense properly, but this is not entirely restricting as it is possible to mount metallic targets on a non-metallic flexure. A Pugh chart was made to help decide which material should be chosen for the flexure; metals were chosen as the "baseline" and two other material classes were compared against metals along various criteria.

Polymer advantages are that they are relatively inexpensive (except for the more exotic materials such as PEEK), and are inexpensive to machine. Disadvantages are that they tend to have large thermal expansion coefficients, they suffer from viscoelastic effects such as stress relaxation, and their stress-strain curves are not always linear in the elastic region.

Ceramic advantages are their low temperature stabilities and excellent stress-strain linearity (either they behave elastically, or they break); however ceramics would be extremely difficult and expensive to machine. This disadvantage was double-weighted because not only are

they difficult to machine, but certain technologies such as wire EDM machining are unavailable for ceramics.

Table 4.1: Material decision matrix

Material	Material cost	Machining cost	Temperature stability	Viscoelastic effects	Stress-strain linearity	Total
Metals	0	0	0	0	0	**0**
Polymers	1	1	-1	-1	-1	-1
Ceramic	-1	-2	1	0	1	-1

The next challenge was to choose which metal to use for the flexure. Because of the larger stresses involved when dealing with compressed flexures compared to conventional flexures, aluminum was ruled out due to its ill-defined yield point; aluminum under larger loading readily develops hysteresis. For conventional aluminum flexures, beam stresses are typically kept to within 10-30% of the yield strength; keeping this restriction with compressed flexures was more difficult. The properties of availability, hardenability, well-defined yield point and corrosion resistance led to choosing 440C stainless steel hardened and tempered to R_c 55, which gives a yield strength of approximately 1900 MPa .

4.3 Metrology considerations

The experiment requires that the six degrees of freedom of the test stage be measured, as well as the displacement of the input stage; therefore seven sensors would be required. The

sensors would have to measure displacements on the order of microns with a resolution of at least 0.1 μm (a factor of 10). The sensors had to meet the following requirements:

- Ideally should be non-contact to avoid adding any parasitic forces to the test stage

- The sensors should be compact, as there would be 7 of them arranged around the test flexure

The first bullet point above ruled out many precision sensor technologies such as LVDTs, micrometers and potentiometers. A set of capacitive probes were available and it was decided that these would be ideal for the experiment for the following reasons:

- Seven probes and driver units were available, which was exactly the number of sensors needed: six for measuring the stage's motion in space, and one for measuring the input displacement

- The sensors had 10 nm resolution

- The sensors were non-contact and would not add parasitic forces

- The probes were compact, allowing all seven of them to be mounted into a small frame

It was therefore decided that the test setup would be designed around the capacitive probes.

In addition, the interconnections between the modules should not be overconstrained to avoid imparting any parasitic misalignments or loadings on the experimental setup. Any pre-existing deformations caused during assembly can grow with any additional loadings on the parts, and on a test setup with large forces these deformations can cause additional parasitic deformations. Kinematic couplings can be used to mount together different parts without overconstraint – a kinematic joint will not cause warping because it is exactly constrained. Designing a kinematic coupling involves consideration of the contact stresses at the coupling

85

interface, which can quickly exceed material yielding limits even for light nesting loads between the coupling halves.

4.4 Transverse actuator considerations

The actuator was required to be non-contact, just like the sensors, to avoid any parasitic forces from within the actuator affecting the test-stage motion. This requirement restricted the design space by eliminating some actuators such as micrometer slides, pneumatic actuators, and hydraulic actuators. A voice coil was chosen because it was non-contact and could tolerate some misalignment. The voice coil was required to be able to exert enough force to cause a displacement at least two orders of magnitude larger than the sensor resolution. For the capacitance probes, with sensor resolution on the order of tens of nanometers, this requirement imposed that the voice coil be able to exert a displacement of at least 1 μm, which required a force output of order 0.1 N based on some first-order estimates. To size the voice coil, several voice coils from online vendors were compared based on their overall size, force output, and price; one from Moticont was chosen with a continuous force output of 2.5 N, which exceeds the force output requirement by an order of magnitude.

4.5 Manufacturing considerations

The overall scale of the flexures was constrained by the sensing area required by the capacitive sensors; several prototype manufacturing methods were evaluated. Manufacturing a flexure at this scale would require a machining process with tolerances on the order of microns (two orders smaller than the characteristic feature, the thickness of the flexures) using either

86

CNC milling, Abrasive Waterjet (AWJ) machining, or wire electro-discharge machining (wEDM).

4.5.1 Abrasive waterjet (AWJ) machining

AWJ machines are machines which use a high-pressure stream of water mixed with abrasive to pierce through almost any material, including ceramics and hardened steel. AWJ machining was an attractive option, as there were several of these machines available for use; however, machining tight-tolerance (on the order of tens or microns or better) high quality parts required a well calibrated machine (and operator). In addition, AWJ machines are known to create tapered parts unless the cut speed is slown down drastically, which increases the cost to operate the machine; Awtar discusses in-depth the quality of AWJ-machined flexures [14]; of particular importance is that he notes the AWJ does not produce vertical walls, instead producing slanted walls. The magnitude of the slant changes depending on how fast the machine is cutting and the thickness of the workpieice. Searching online for various AWJ cutting services shows tolerances of around 125 μm, 25 times larger than that for wEDM (see next section).

4.5.2 Wire electro-discharge machining (wEDM)

wEDM machines are something like a high-tech hot-wire foam cutter; they function by holding a thin wire taut and introducing a high voltage between the wire and part. Sparks arc across the wire and part, eroding away material, even for hardened materials that would be difficult to machine by conventional methods such as milling and drilling. Tolerances quoted by several wEDM services offered on the Internet give a typical value of about 5 μm. wEDM

87

machining is limited to conductive materials, such as metallic parts, and is expensive compared to conventional manufacturing processes such as CNC milling.

4.5.3 CNC milling

CNC is a general, well-established subtractive manufacturing process that is capable of producing different geometries by mechanically shearing away chips of material with a cutter. The specific application of CNC milling to flexure fabrication is discussed by Smith [1]. This mechanical shearing of material introduces surface stresses to the material being cut. In addition, cutting thin walls such as flexure blades can be problematic due to the cutting forces involved; often, while machining a flexure blade, the thin wall will resonate and leave a poor surface finish. While inexpensive compared to wEDM, the process has a major drawback in that it is much more difficult to machine hardened materials. Machining hard materials is still possible with proper feeds, speeds, tooling, and operator knowledge. If the flexure is designed with narrow slots, it will be more difficult to machine because it will require a long, thin endmill; such endmills have low rigidity and will typically leave poor surface finishes, if they can even be used at all. If the endmill is not rigid enough, it will not be able to cut the material; instead, the endmill will flex and the endmill will rub on the surface. This is especially relevant when attempting to machine a hardened material. Tolerances will be sensitive to these process parameters and a hardened material will be less forgiving to any deviations from optimum machining parameters, and tolerances would be at best around 5 μm.

4.5.4 Comparison of manufacturing methods

When comparing these three manufacturing processes for machining flexures, wEDM comes out as the best choice if cost is not a concern and if the material is conductive because of its tight tolerances and straight walls. AWJ machining would be the next-best option, but its wider tolerances and inconsistently tapered walls are a disadvantage when compared to wEDM; AWJ machining does have the advantage over wEDM of being able to machine non-metallic materials. CNC milling may not even be possible depending on the flexure geometry and material hardness condition; CNC milling would be useful for machining larger flexures out of softer materials such as aluminum if precautions are taken to avoid damaging the flexures during the machining.

4.6 Experimental setup design

The experimental setup for characterizing the flexure stage was designed in modules. The design of each module is discussed below. All of the modules were made of the same material; as Awtar discusses in his Ph.D thesis [14], 6061-T651 aluminum has the advantage that it is stable with time, it has intermediate strength compared with other aluminum alloys such as 7075, and it contains low internal stresses. Combined with the excellent machinability of 6061-T651 and its availability, 6061-T651 was chosen for all machined parts, except the machined preload wedge.

4.6.1 Flexure loading frame design

Two concepts were considered for mounting the flexure design presented in §4.2. The first concept, Figure 4.6(a) shows a concept where the flexure is bolted to a thick subplate.

Figure 4.6(b) shows a concept where the flexure is sandwiched in between two thick plates. In each figure the load path through the structure is shown; each element in the load path must deform.
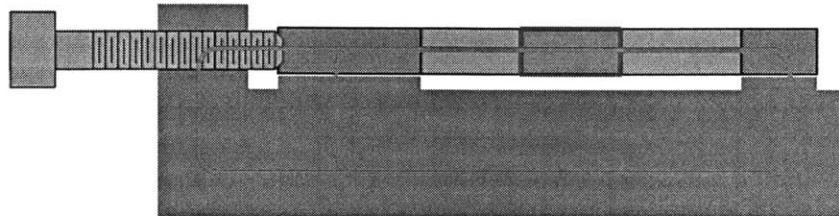
(a)
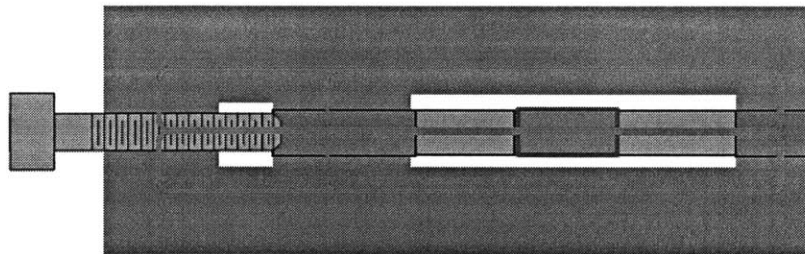
(b)

Figure 4.6: Two concepts for the load frame.
The red line represents the force load path through the test setup; the screw imposes a compressive load that must be resisted by the load plates (a) single plate design (b) symmetric double plate design.

Each of the concepts comes with disadvantages and advantages. Concept (a) allows for a more accessible stage, but has the disadvantage that the input forces from the screw cause bending moments in the load plate and in the screw mount which cause parasitic motions and loadings. Concept (b) has a symmetric design that does not impart any bending stresses and avoids bending entirely. For this reason concept (b) was chosen.
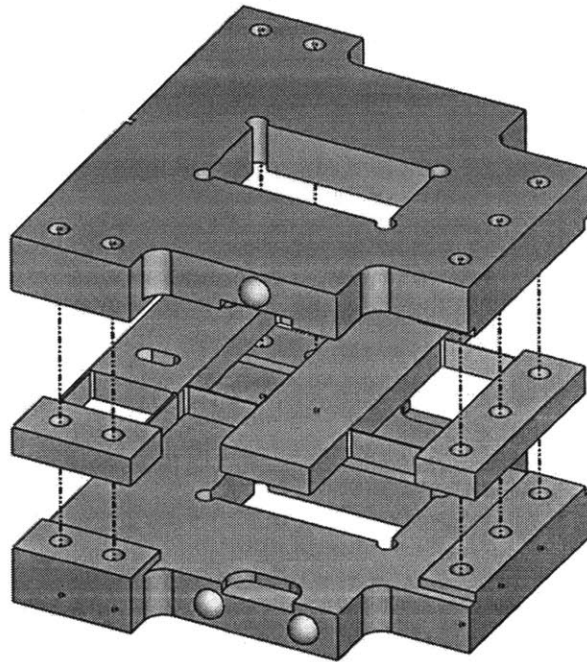
Figure 4.7: Load plate and test flexure exploded view assembly.
The holes in the top and bottom load plates are clearance; socket head cap screws go through
the entire assembly, and nuts are used to clamp the assembly together.

The holes in the top and bottom load plates are clearance for ¼ -20 socket head cap
screws to go through the entire assembly, and nuts are used to clamp the assembly together. The
bottom plate of the load frame has three balls epoxied in with which to rest on the mounting
base; this prevents any parasitic deformations from being caused by bolting it down.

4.6.2 Metrology frame design

The metrology frame is designed to be completely decoupled from the load bearing
structure in accordance with good practice in precision machine design [15]. Coupling between
the load frame and metrology frame results in warping of the metrology frame, which in turn
results in erroneous sensor readings due to parasitic relative motion between the sensor
supporting structure and the sensor targets. In this experiment the metrology frame holds seven

91

probes and is designed to fit through holes in the load bearing structure to measure the six

degrees of freedom of the flexure stage and one degree of freedom of the preload input stage.

Capacitive probes are mounted in the structure using soft-point setscrews – these screws have a

tip made of a soft polymer and will not damage the capacitive probes. Figure 4.8 shows the

metrology frame coupled to the mounting base; the mass of the metrology frame provides the

nesting force for the kinematic coupling.
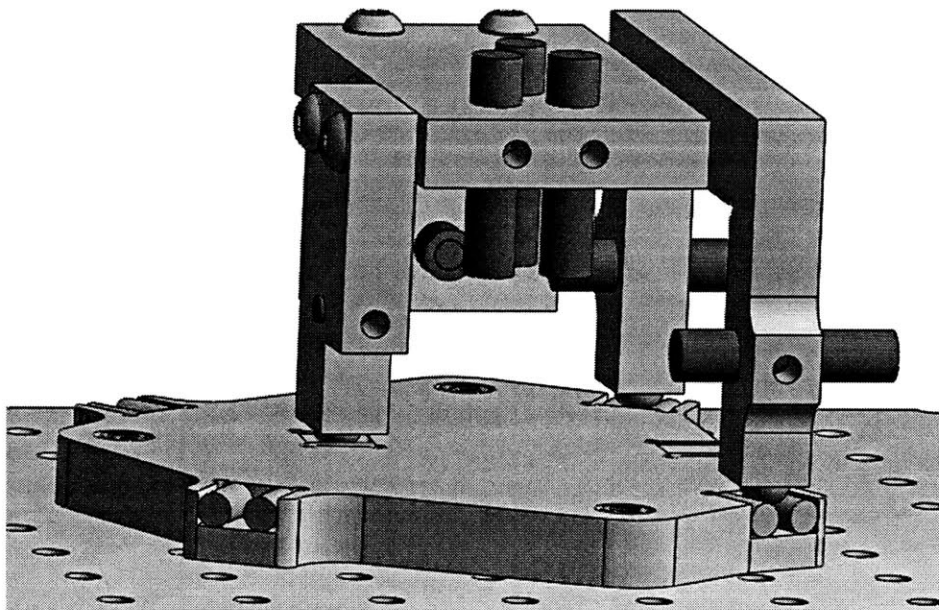
Figure 4.8: CAD model of metrology frame resting on mounting base

Having a kinematic coupling at the base instead of bolting the frame down prevents any

frame distortion due to tightening the bolts. The arrangement of the capacitive probes and

metrology frame (with the top piece shown as transparent) around the test flexure stage along

with the coordinate system used is shown in Figure 4.9.
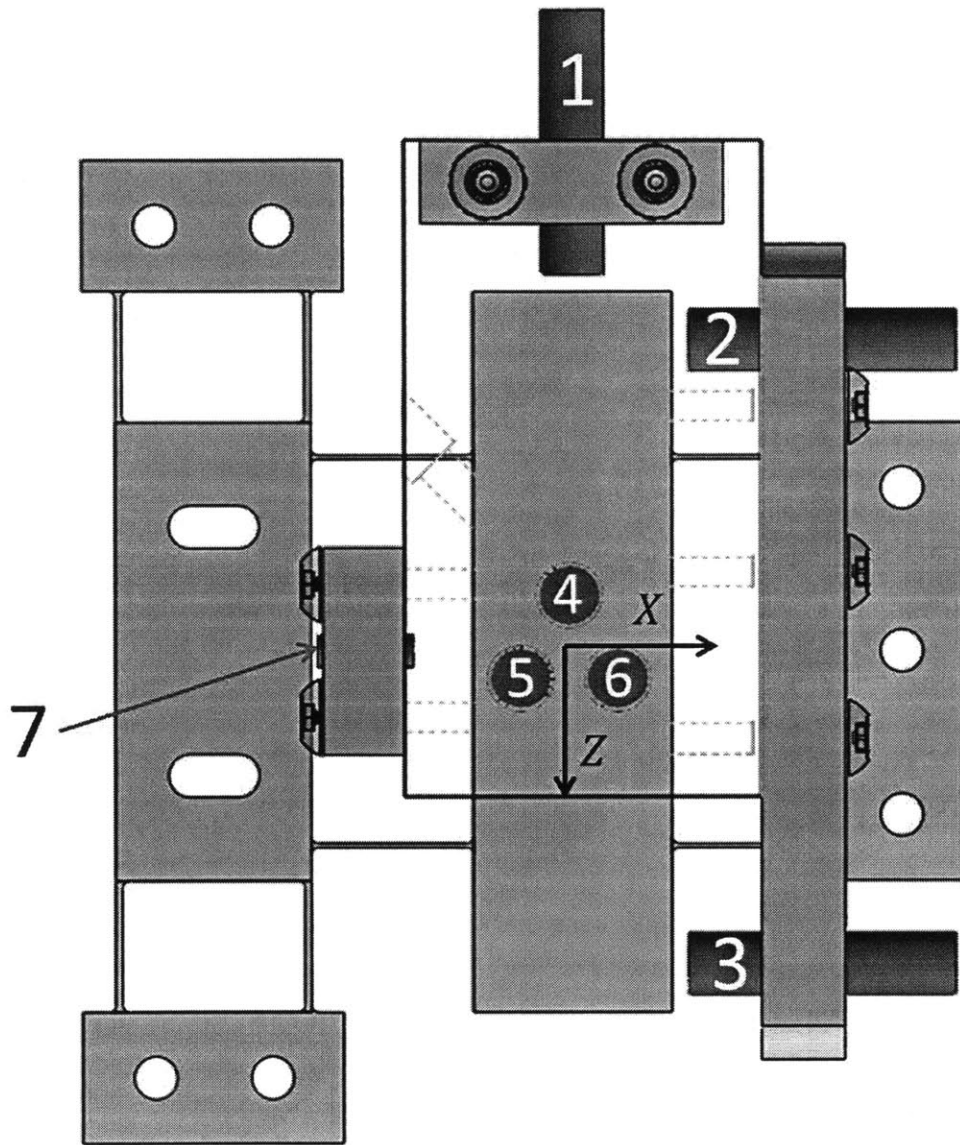
Figure 4.9: Arrangement of seven probes and coordinate system used in the experimental setup. X is the compression axis, Z is the "sense" direction, and Y is the out-of-plane direction

4.6.3 Mounting base design

The mounting base provides a stable support for the test setup and metrology frame without imparting any additional loads. In addition, this setup allows the probes to be adjusted slight and replaced into their original position, which is especially important for probe 7 as it is deep within the structure and not accessible without removing the frame (see Figure 4.9). This particular mounting base bolts to an optical table, and contains two sets of kinematic coupling
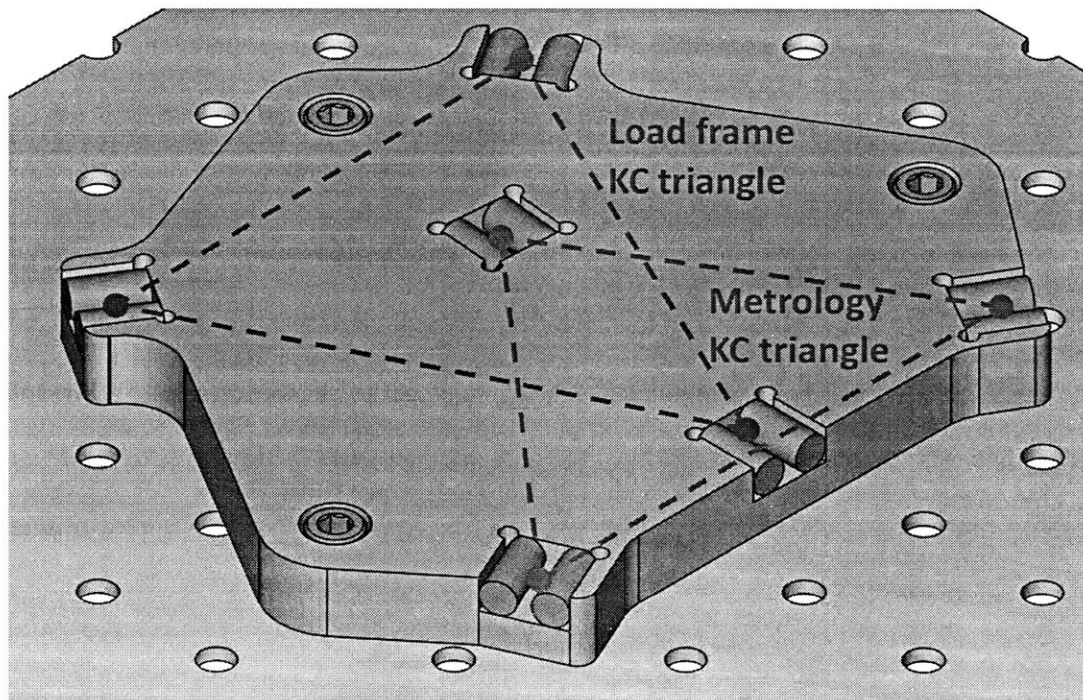
Figure 4.10: Mounting base bolted to optical table.
The two kinematic coupling triangles are superimposed; the metrology frame triangle is drawn in red and the load frame triangle is drawn in blue.

halves, one each for the test setup load frame and one for the metrology frame. The odd shape allows the socket head cap screws to pass through both load plates and accept a nut on the other end without interference. Figure 4.1 shows the entire test setup assembled and resting on the mounting base.

4.6.4 Preload module design

The preload module applies a force or displacement input to the flexural bearings. In order to effectively apply a displacement input, the preload module must be much stiffer than the axial stiffness of the flexures. If this is not the case, when applying displacements the preload module will stretch instead of compressing the flexures. The combined axial stiffness of the flexures being compressed is on the order of $100 \frac{N}{\mu m}$, requiring forces on the order of hundreds of Newtons in order to reach the buckling load. Any module that pushes axially against the flexure must be able to do so with a significant amount of force without itself being more compliant than the flexures. If the preload module displacement input is too compliant, it would not hold the input stage rigidly and the input stage would be moving slightly as the test stage is being actuated. The axial stiffness of the flexures can be calculated by assuming uniaxial compression of the columns,

$$K_{axial} = \frac{EA}{L} \qquad (4.14)$$

and is computed to be of order of magnitude $10^7 \frac{N}{m}$. Because columns are stiff in the axial direction, even small displacements can generate large reaction compression loads. The Euler buckling load for the columns was calculated to be in the $10 \ \mu m$ range, so the preload module should allow for submicron-level displacement adjustment.

Micrometer heads were initially considered, but were immediately ruled out as their load capacity was far lower than required in this application; these types of micrometers can only withstand approximately $1N$ of force before incurring thread damage. The buckling loads were calculated to be approximately $800 \ N$, which is far higher than can be tolerated by a micrometer.

95

A simple screw such as a 10-32 can be used in place of the micrometer slide, but with less resolution than the micrometer (friction is ultimately the limiting factor).
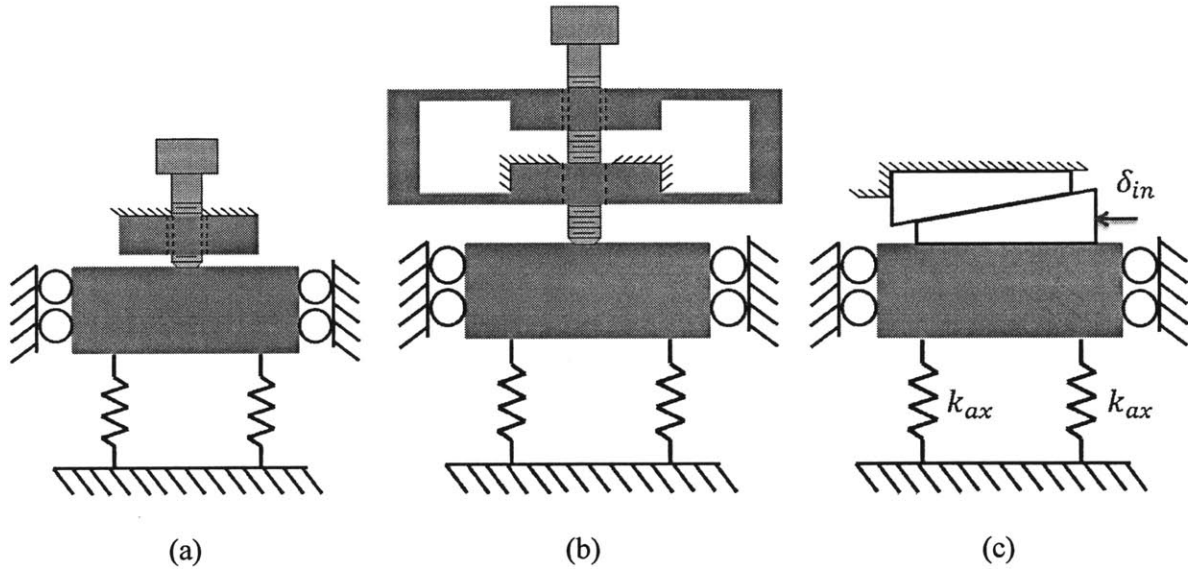
Figure 4.11: Several ideas for applying displacement inputs into the guidance flexure, from left to right:
a) Applying displacement directly with a micrometer head
b) Applying displacement through a deamplification flexure
c) Applying displacement through an inclined plane

Another idea considered that would allow for greater preload input resolution was to add a second set of springs in series with the beam-columns as shown schematically in Figure 4.12. The assembly in Figure 4.11(b) can be represented schematically as shown in Figure 4.12.
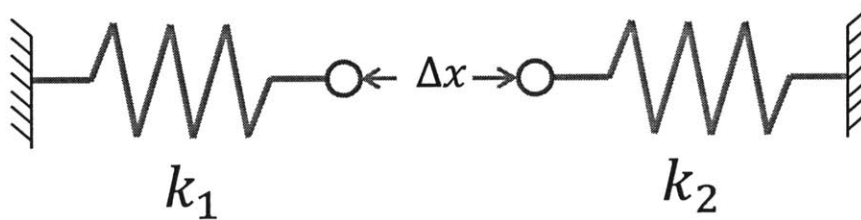
Figure 4.12: A displacement divider module that could be used for a preload module. By engineering the ratio of k_1 to k_2 it is possible to divide up the displacement input Δx between the two springs.

Suppose that k_2 is the combined axial stiffness of the compressed flexures and k_1 is the net stiffness of the preload flexure assembly; the input Δx, which could be provided by a screw, is divided between the two springs depending on the ratio of k_1 to k_2. The deflections of each spring x_1 and x_2 must add to Δx and the forces must balance, therefore

$$k_1 x_1 = k_2 x_2 \qquad (4.15)$$

$$x_1 + x_2 = \Delta x \qquad (4.16)$$

If Δx is the input and x_2 is the output, an input-output relation (4.17) can be written by solving (4.16) for x_1 and plugging into (4.15).

$$x_2 = \Delta x \left(\frac{k_1}{k_1 + k_2} \right) = \Delta x \left(\frac{1}{1 + \frac{k_2}{k_1}} \right) \qquad (4.17)$$

If the goal is to increase the preload resolution, one could engineer the ratio of k_2 to k_1 to achieve a specific deamplification ratio; for example, setting a ratio of 9 would allow the output to move $\frac{1}{10}$ of the input, effectively deamplifying the input by a factor of ten. In practice, such a flexure would have a disadvantage because it would not be able to effectively hold the flexure in place.

97
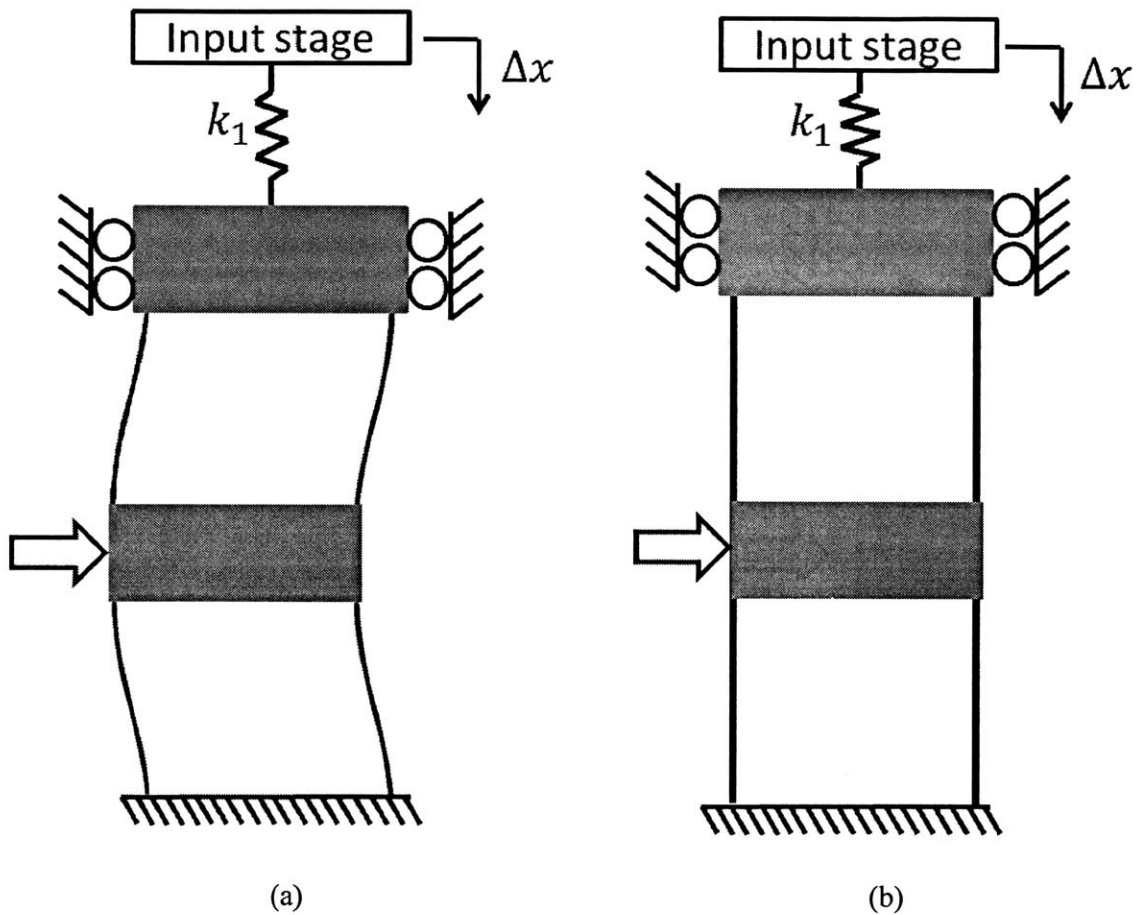
Figure 4.13: Diagram of a spring in series with the axial stiffness of the flexures.

(a) The input stage is moved a distance Δx while a lateral load is applied to the flexure stage. (b) If k_1 is not much stiffer than the axial stiffness of the flexures, the flexures will be able to relieve some of their displacement input by compressing k_1. If k_1 were much larger than the axial stiffness of the flexures, the flexures would be forced to maintain the input displacement Δx

Another idea was to use a wedge for preloading, and the mechanical advantage could be changed by varying the angle of the wedge. Such a module would provide excellent stiffness, as it would have a large cross-sectional area with a large thickness. Two wedge halves would slide along one another, and would be pulled together or apart by a screw going through one and threaded into the other. A 5 degree wedge was initially considered as it gave a factor of ten increase in displacement resolution, but the slope was too small to fit within the constraints of

98

the structure. A 10 degree wedge would give a factor of five increase in displacement resolution while remaining compact enough to fit within the confines of the experimental setup.
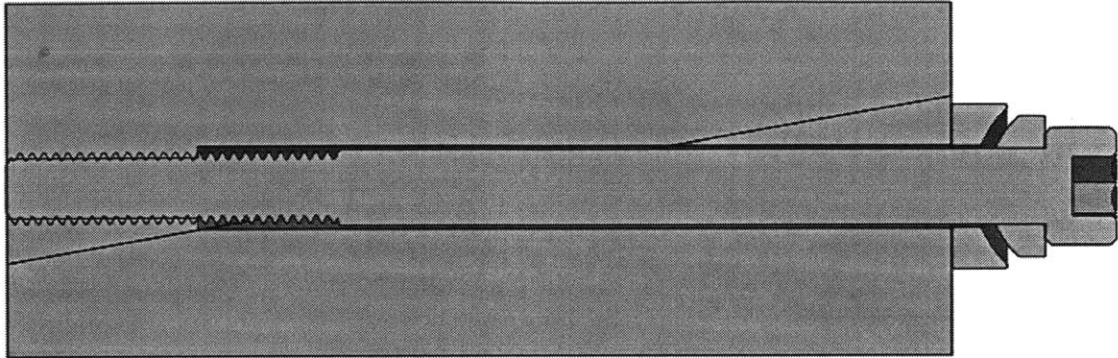
Figure 4.14: Cross-section of a wedge actuator with a 10° incline.
A shallower incline would require a longer bolt and wider wedges. Even with a greased spherical washer this design is overconstrained and relies on bolt flexibility to function, but was found to work well for this experiment.

To hold the preload wedge in place and couple it to the load frame, a heavy-duty quasi-kinematic coupling based on line contact was designed and is shown in Figure 4.15. The stiffness of this coupling is designed to be two orders of magnitude higher than the axial stiffness of the flexures. The quasi-kinematic coupling is preloaded using four 311 N [70 lbf] Belleville washers.
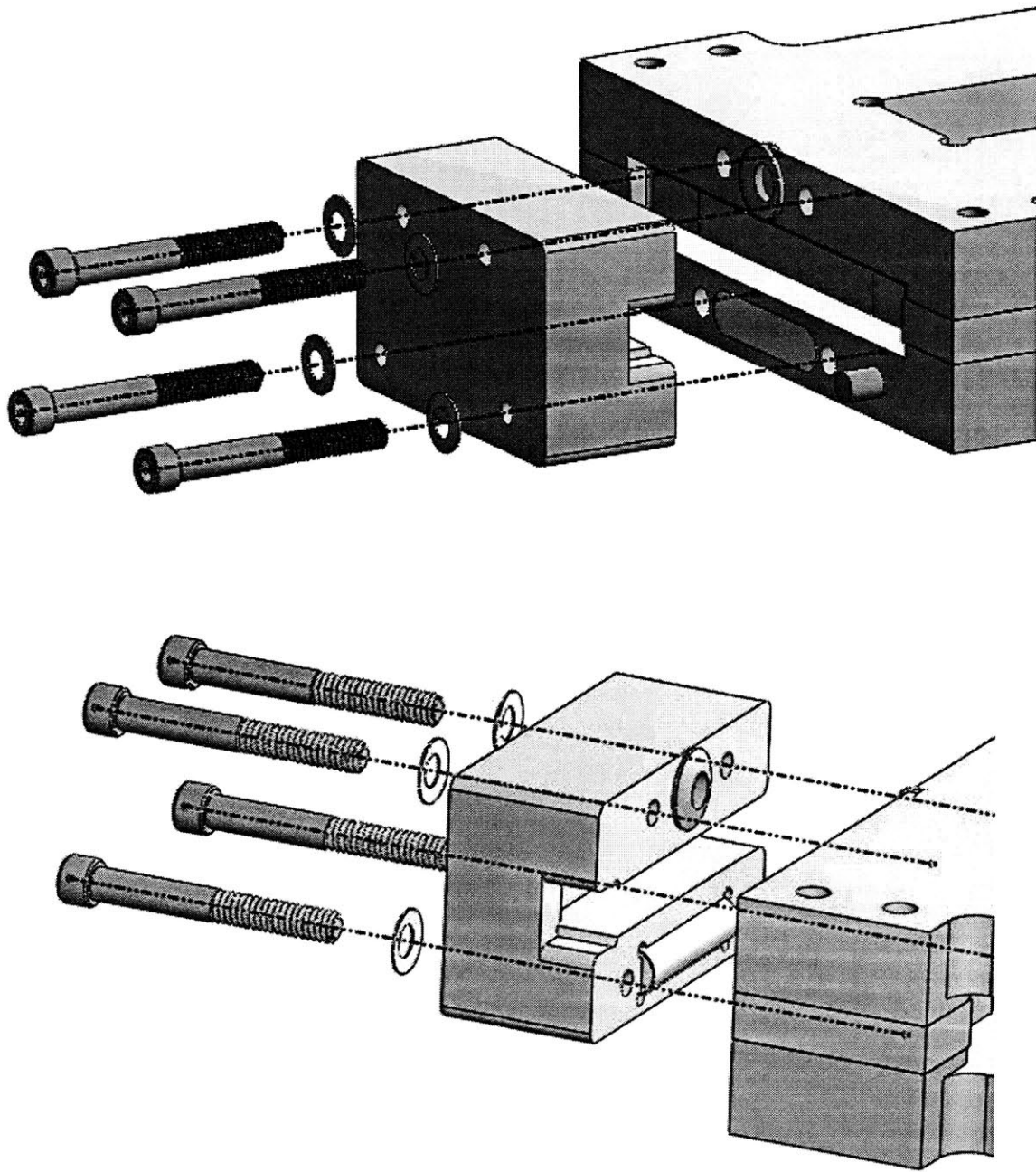
Figure 4.15: Exploded view of preload module coupling to the load frame.

Four Belleville washers are used to maintain coupling preload. A dowel pin is used to contact the bottom plate, and a spherical washer is used for the top plate. A dowel pin in the bottom plate constrains rotation.

100

4.6.5 Actuation module design

Several different actuator technologies were considered for applying force to the test stage, including voice coils, stepper motors, and pneumatic cylinders. A voice coil actuator was chosen due to its small size, simplicity of operation, and its ability to apply forces without contact.

The actuation module Figure 4.16 was designed with the requirement that it be at least two orders of magnitude stiffer than the stiffness of the flexures in the "sense" direction, and that bolting on the module does not distort the load frame. The actuation module bolts on to the load structure via a kinematic coupling which was designed to have the required stiffness two orders magnitude higher than the stage's stiffness in the Z direction.
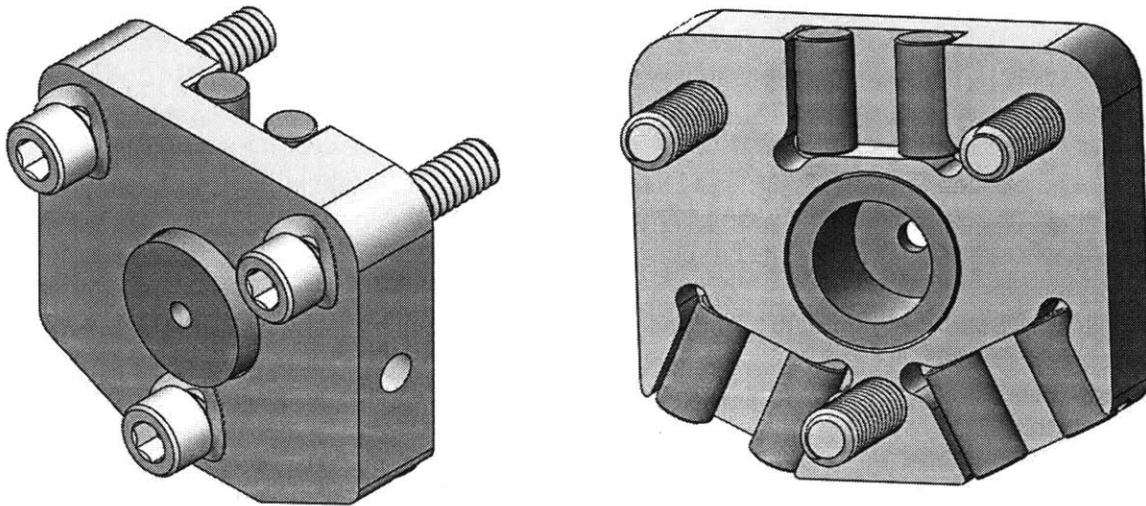
Figure 4.16: Front and back of actuator module.
This half of the module holds the voice coil magnet tube;. The tube magnet is potted in place with epoxy.
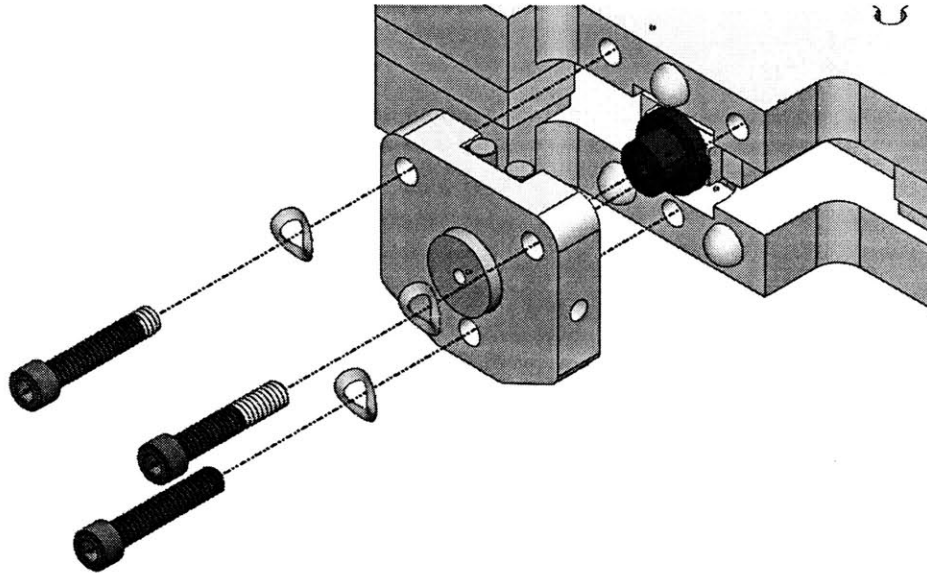
Figure 4.17: Exploded view of actuation module mounting on to load frame.
Wave washers are used to preload the kinematic coupling.

The actuation module is designed to mount on to the load frame through a kinematic

coupling whose stiffness is designed to be two orders of magnitude higher than that of the

flexure in the transverse direction. The kinematic coupling is preloaded using three $22\ N$ wave

washers. To ensure alignment of the voice coil magnet with the voice coil plunger, an assembly

process was developed. An adapter piece screws into the plunger and is epoxied to the test stage.

The voice coil plunger is wrapped with shims of decreasing thickness of either 0.5 mm, 0.25

mm, 0.127 mm, 0.025 mm or 0.0127 mm until a snug fit is achieved between the plunger and

magnet tube. Once the snug fit is achieved, the voice coil housing is left on the motor while the

kinematic coupling is installed – the central bore in the kinematic coupling is oversized so that

the coupling easily passes over the voice coil magnet housing. The kinematic coupling is then

102

bolted down until the wave washers flatten out to achieve the required preload. The gap between the kinematic coupling and voice coil housing is then filled with epoxy and allowed to cure. The kinematic coupling is unbolted and removed, and the shims are removed from the gap between the housing and plunger. The actuation module is calibrated and ready for use.

4.7 Instrumentation

The sensors, data acquisition hardware, actuators, and data processing software used to record and process data are described in the following subsections.

4.7.1 Sensors

Six Lion Precision C8 probes with a modular driver unit containing six DMT22 drivers were used to record displacements of the central motion stage; in addition, a C5R probe with its own standalone DMT22 driver unit was used to measure displacement of the input stage. The C5R probe's smaller form factor made the design of the metrology frame significantly simpler since the probe measuring the input displacement was placed deep within the structure. The probes have high and low resolution modes; it was found that the motions in the plane of the flexures were too large for the high resolution modes, but the out-of-plane motions were small enough such that using the high-resolution setting was acceptable. To characterize the sensor noise, the test setup was assembled and probe measurements were taken for 30 seconds at 1 kHz without actuating anything. Probe noise is summarized in Table 4.2; refer to Figure 4.9 for the location of each probe within the test setup.

Table 4.2: Probe noise, one standard deviation, averaged over three trials. Probes 1-3 and 7 are in low-resolution mode; 4-6 are in high-resolution mode

Probe	σ [nm]
1	9.58
2	9.95
3	14.5
4	2.3
5	3.7
6	1.5
7	8.7

4.7.2 Data acquisition

A National Instruments CompactDAQ cDAQ-9172 USB Data Acquisition system was used to measure signals. This system used modular input/output modules, allowing the experimenter to pick and choose exactly what hardware is needed to record data. Two 4-channel Analog-to-Digital Converter (ADC) 16-bit NI 9215 modules were used to record measurements from the capacitive probes. To record thermocouple data, an NI 9211 4-Channel 24-bit Thermocouple input module was used. Another NI 9215 module was used to record the output from the signal generator.

The 16-bit resolution of the ADC module over the 20 V range used by the capacitance probes resulted in a displacement resolution of 3.82 nm in low resolution mode and 0.762 nm in high resolution mode. The low resolution limit is smaller than the average capacitance probe

$\pm$ 3σ noise value by a factor of approximately 18, and the high resolution limit is smaller than the average hi-resolution capacitance probe $\pm$ 3σ noise value by a factor of approximately 20.

4.7.3 Actuation

An Agilent 33220A Waveform Generator was used to generate the input signal to a Moticont LVCM-019-016-02 linear voice coil actuator. The waveform generator is capable of creating all commonly used signals such as sine waves, square waves, and triangle waves. A triangle wave was chosen to emulate a simple load-unload test. The waveform generator has an accuracy of $\pm$ 1 mV_{pp} represents 1% of a 100 mV_{pp} signal.

The Moticont voice coil had a force constant of $1.5 \frac{N}{A}$, a resistance of 1.6 Ω, and a stroke of 6.35 mm. The voice coil force changes with stroke length, from its mid-stroke position to the end of its stroke losing 0.7 N off of 2.5 N, which represents 28% of its force output. During the experiments the coil moves at most 50 μm which represents 0.8 % of the coil's stroke. An estimate for the force drop-off during the experiments due to the voice coil force-stroke relationship would be 0.8% of 0.7 N, or 0.0056 N. With the actuation forces on the order of 1 N, this represents a 0.56% change in the force output during an experiment.

4.7.4 Data processing

Processing the data recorded by LabVIEW is done in MATLAB; a script performs the following actions:

- Imports the text file data into an array
- Converts probe measurements into stage displacements
- Creates various plots

105

- Writes a new directory and saves plots into this new directory

Since some of the models were derived using MathCAD's symbolic manipulation

capabilities, some data is also imported and processed in MathCAD. The transformation matrix

used to convert probe outputs to stage displacements is given in Appendix A, Figure A.2

5

RESULTS AND DISCUSSION

5.1 Experimental Procedures

Each section in this chapter describes an experiment and compares the results to the related models, if any. To establish the range of compression to be used in the experiments, preload was applied until the flexures were observed to snap-through buckle (snap-through buckling was chosen as the buckling criteria as discussed in §5.2); the amount of preload necessary for snap-through buckling was then used to establish inputs for the other experiments. Preloads between zero and the snap-through buckling preload were chosen, spaced at different intervals depending on the experiment. In some experiments, transverse loading from the voice coil actuator was not used, such as that described in §5.3; in that experiment only input preload was applied. In other experiments, such as those described in §5.4 and §5.5, the preload was set to a certain amount, then the voice coil actuator was energized with a 1 Hz triangle wave that both pushes and pulls on the test stage. The transverse stiffness was calculated from this data by dividing the output force by the measured stage displacement, and the output motion was also recorded to monitor other effects such as hysteresis or parasitic motions.

5.2 Determining the buckling load

It was found that the buckling input measured in the experiment was not consistent with the predictions made by the Euler equation; the buckling behavior itself was different from what was expected from Euler column buckling theory. Euler buckling theory predicts that the columns would remain in their initial straight configuration while being loaded, and would only bow out to the side at the critical buckling load; from the data presented in Figure 5.1 it can be seen that the flexure bows out monotonically with increasing load; there is no clear buckling load. The Euler critical load for each clamped-clamped beam is 407.3 N per column; for two columns, this requires a total buckling load of 815.0 N, which corresponds to a displacement of 17.88 μm.
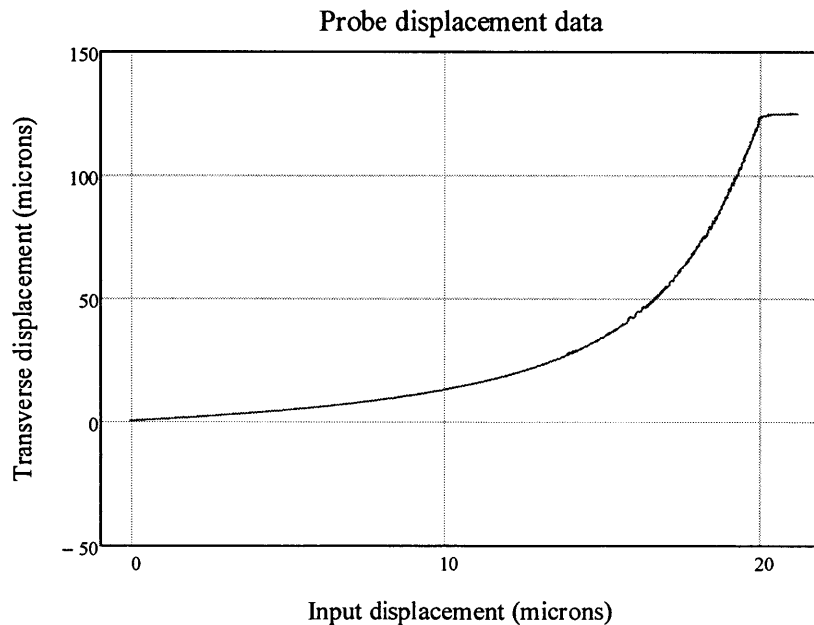
Figure 5.1: Transverse displacement of the flexure stage as a function of input displacement. There is a lack of a discrete 'buckling point'. Probe saturation occurs at the 125 micron mark, the probe's maximum range.

108

Initial imperfections in the flexures cause the flexures when loaded axially to monotonically increase their transverse displacement in response to the axial load. There is no single point at which the flexure suddenly buckles; if there exists any initial imperfection, the flexure will bow outwards in response to compressive loading to minimize its strain energy rather than remaining straight and there is no clear transition between Euler buckling and post-buckling behavior. By having initial imperfections, the column can be considered to already have buckled into its first mode.

This test was initially carried out by alternately applying a small amount of input displacement, then lightly probing the test stage, watching for snap-through behavior; at first it was thought that snap-through behavior meant that the flexure has buckled. However, snap-through behavior does not imply the first buckling mode; this test methodology cannot determine the first buckling mode. From the modeling in 2.3 it is known that the first buckling load is actually a range where the transverse displacement grows monotonically and nonlinearly, with Z displacement growing until the sensor saturates (see §5.3, Figure 5.4).

When the flexure is perturbed from its equilibrium position (Figure 5.2a), the flexure initially behaves as a spring. Upon further application of the perturbing force, the flexure columns are forced to shorten, causing compression in the beams. Eventually a point is reached where the columns "snap through" to the equilibrium position on the other side. This is known as snap-through behavior and while interesting in several engineering applications it is considered to be outside the scope of this thesis; in this thesis we focus on the pre-buckling behavior as opposed to post-buckling (behavior occurring after the first buckling load has been reached).
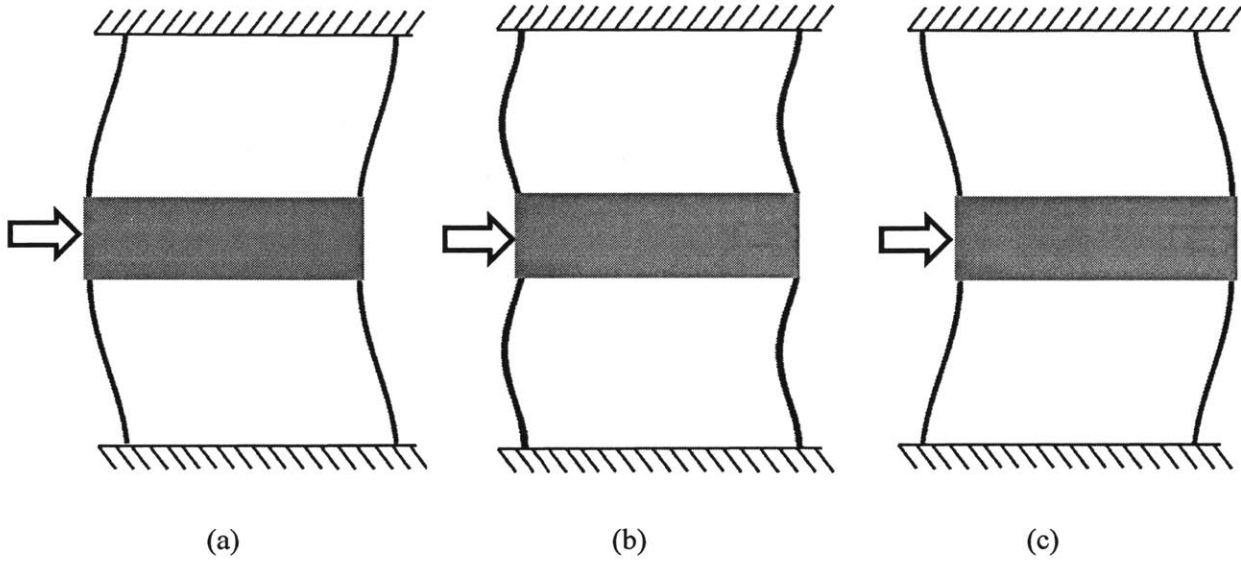
Figure 5.2: Series of figures showing snap-through behavior.
(a) a force is applied while the flexure is at equilibrium, pushing the stage to the right (b) the flexures are forced to compress and (c) will buckle the flexures, which snap through to the other equilibrium point

5.3 Preloading with no transverse actuation

In these experiments, the force coil actuator is not used; the only deformations are those resulting from the input displacement. Displacement is slowly applied to the input stage while the output stage motions are being recorded; any motions in all of the test stage's degrees of freedom (including those that are constrained) are recorded. Figure 5.3 shows the response of the test stage's six degrees of freedom in response to a compressive input displacement. Of particular interest is the motion of the stage in the sensitive direction Z, which is shown enlarged in Figure 5.4, and shows the monotonically increasing Z-displacement in response to the input preload.

The results in Figure 5.4 are significant because they show that assuming the beams buckle as Euler columns is an incorrect assumption; for ideal Euler buckling, no transverse deflection is predicted before buckling and the columns remain straight until buckling. Here it is observed that the flexures are "buckling" in the Z direction in response to any input loading – essentially they have already buckled into their first buckling mode with any compressive loading. This behavior was discussed earlier in §5.2.

The stage also moves in its other degrees of freedom in response to the input preloading; the magnitude of every degree of freedom is observed to correlate directly with the input preload. Only Z, the direction along which the flexures are guiding the motion of the test stage, and X, the compression axis, are expected to displace; the rest can be considered parasitic motions and are discussed in §5.9.

X displacement
$3\sigma = 0.0531~\mu m$

Y displacement
$3\sigma = 0.0091~\mu m$

Z displacement
$3\sigma = 0.0575~\mu m$

θ_x displacement
$3\sigma = 1.4319~\mu rad$

θ_y displacement
$3\sigma = 1.0454~\mu rad$

θ_z displacement
$3\sigma = 1.642~\mu rad$
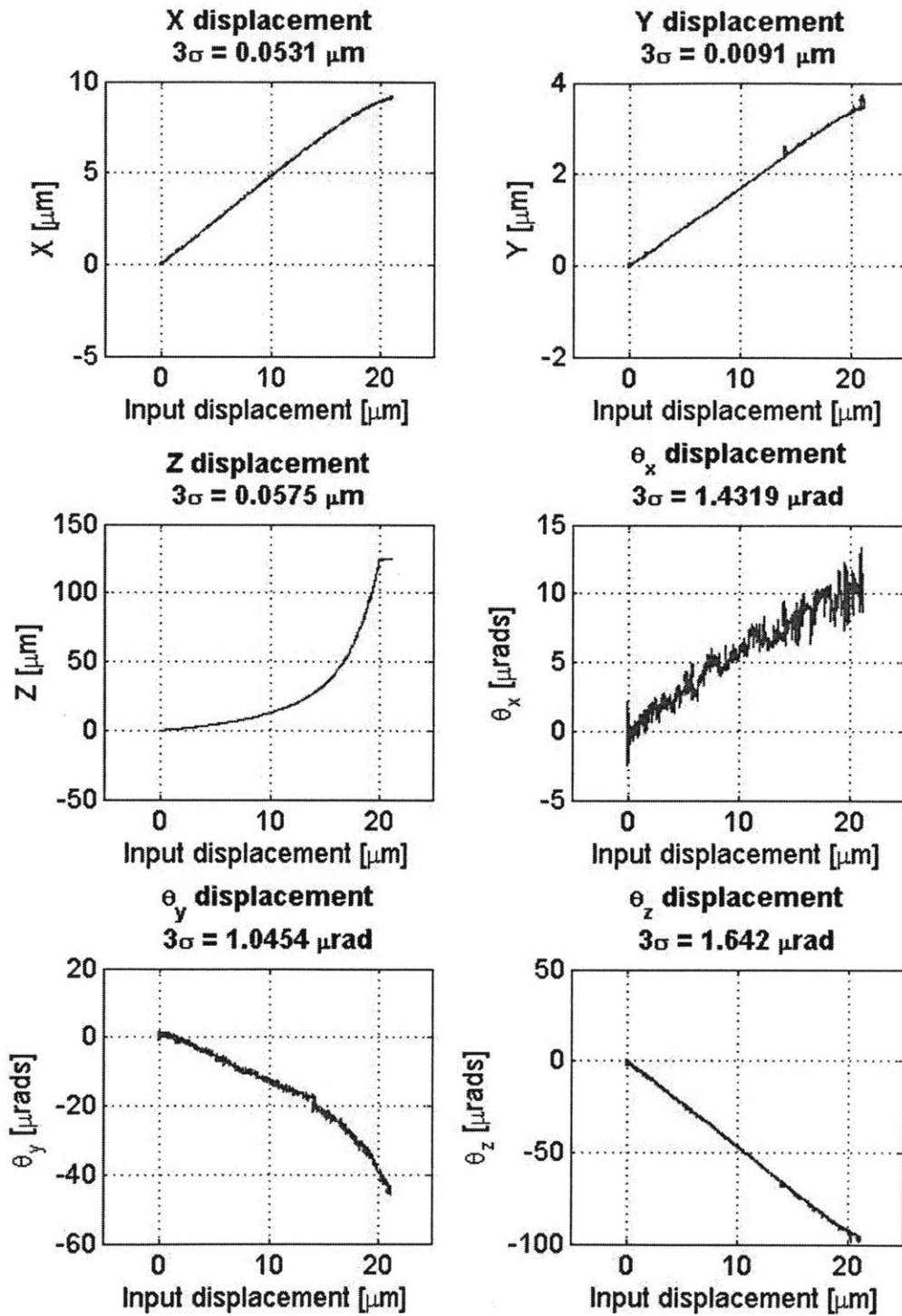
Figure 5.3: Test stage output motions in response to compressive input displacement.

112

Probe displacement data
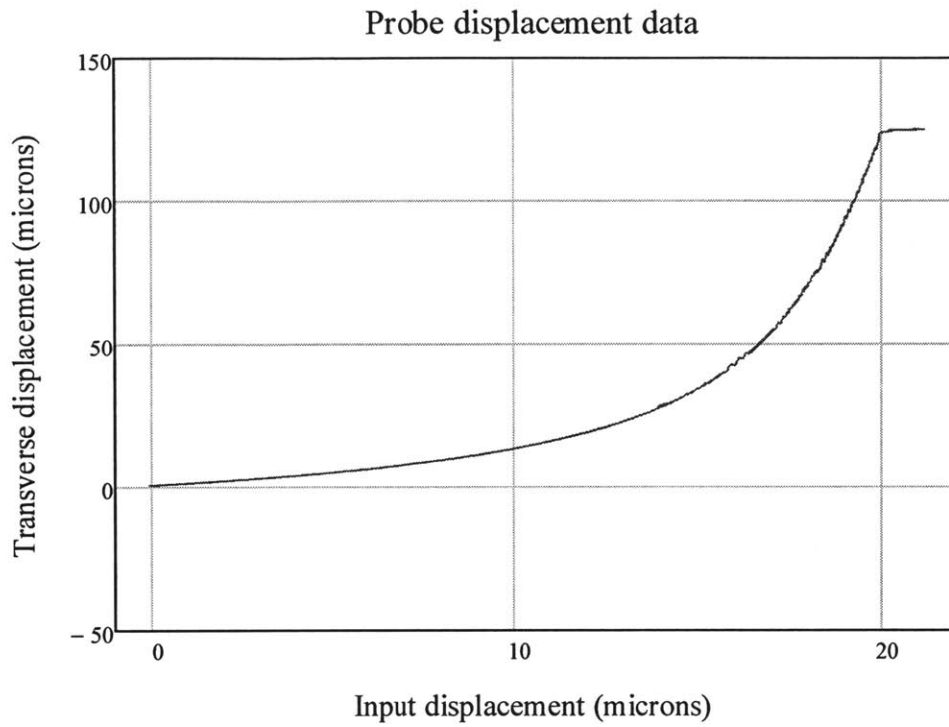
Figure 5.4: Output Z stage motion in response to input displacement.
The flatness at the end of the curve is due to probe saturation.

113

5.4 No preload with transverse actuation

This experiment can be considered a 'control' experiment, as it tests the flexures in their uncompressed state. Figure 5.5 is a plot of the input force against the Z displacement of the flexure, along with a best-fit line. The green lines are the best-fit line offset by $\pm 3\sigma$ where σ is one standard deviation of the Z probe noise; deviations wthin the green line can be considered to be due to noise. The slope of this line is the stiffness of the test stage in the sensitive direction, and the green lines are offset from the best fit line by $\pm 3\sigma$ where σ is one standard deviation of the measured noise. Figure 5.6 shows six plots representing each degree of freedom of the test stage in response to the triangle wave input. The best-fit line shows a stiffness of $85,928 \frac{N}{m}$ compared with a theoretical value of $86,110 \frac{N}{m}$ from modeling the flexures as two clamped-clamped beams in parallel; this is a percent error of -0.21%.

Figure 5.6 shows the displacements in all six degrees of freedom; each data point is also plotted with the probe noise uncertainty bands $\pm 3\sigma$ from the data point. For every output motion except for Z, the motions appear to be about the same magnitude as the probe noise.
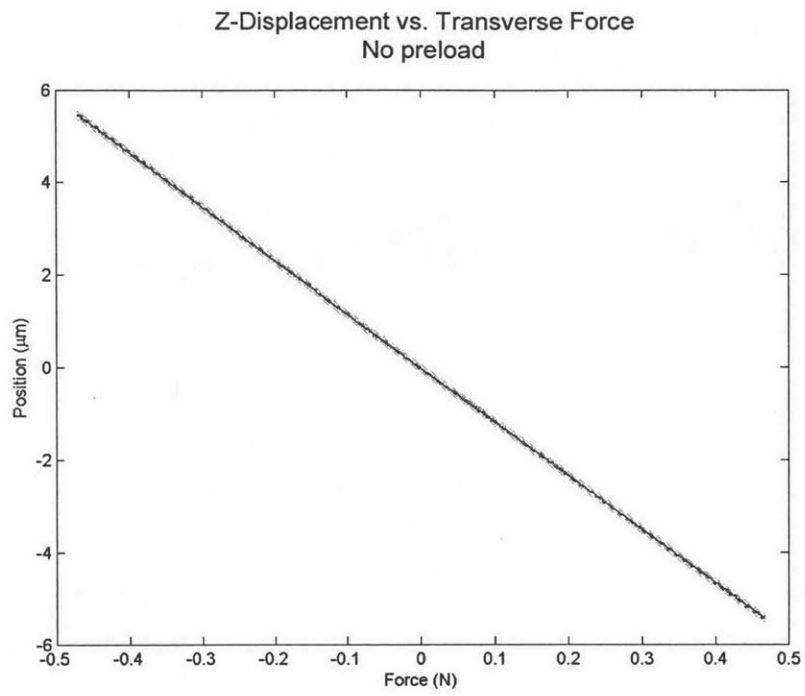
Figure 5.5: Force-displacement relation for an unpreloaded flexure shows ideal flexure behavior.
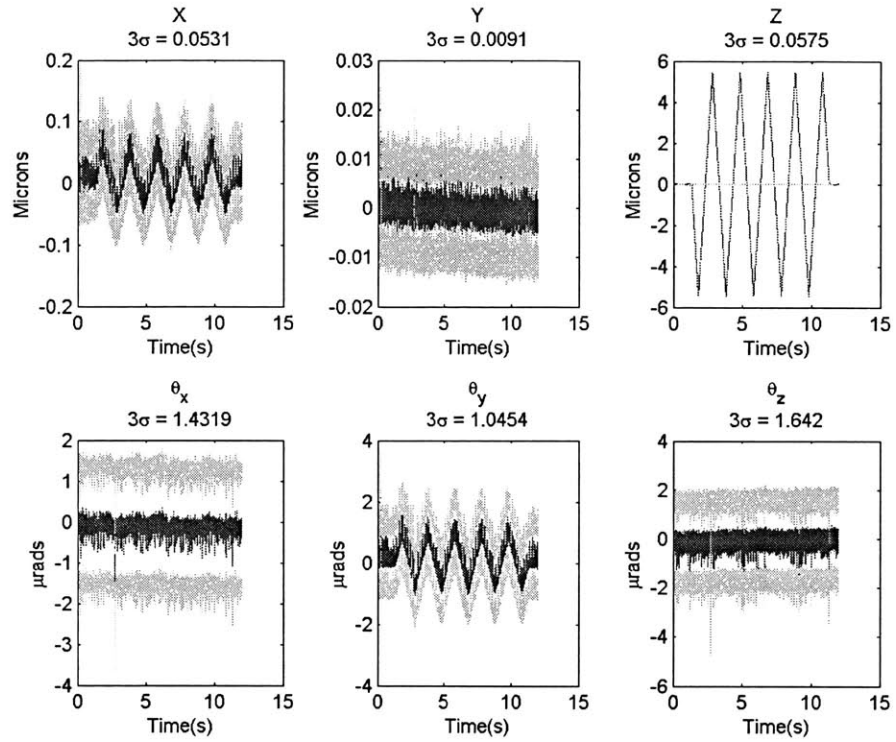
Figure 5.6: Output stage displacement motions in six degrees of freedom.

The green points are the data points offset by $\pm\, 3\sigma$. Only the Z output motion is significant compared to the probe noise; some of the input is also seen in θ_y, which is the in-plane rotation

Table 5.3: Ratios of output displacement amplitudes to probe noise uncertainty
Test performed with no preload

Direction	$\pm\,3\sigma$ probe uncertainty	Peak-peak output amplitude	$\dfrac{Output}{Noise}$
X	0.0531 μm	0.14 μm	2.64
Y	0.0091 μm	0.0079 μm	0.868
Z	0.0575 μm	10.972 μm	191
θ_x	1.43 μrad	0.814 μrad	0.569
θ_y	1.05 μrad	2.64 μrad	2.54
θ_z	1.64 μrad	1.03 μrad	0.628

5.5 Preload test – 19 μm preload

This experiment is similar to the experiment performed in §5.4 but in this case the flexures were compressed by 19 μm. This input displacement of 19 μm was chosen as good representative data because as will be seen in §5.6, beyond this preload the stiffness vs. preload curve levels off and begins to increase.

Figure 5.7 plots the input force versus the Z displacement. Note that the range of motion is an order of magnitude larger for the same input force; there also appears to be some curvature in the stiffness relation, with the compliance decreasing on the left side of the plot and the compliance increasing on the right side of the plot. The curvature is not accounted for from voice coil nonlinearity, as in §4.7.3 it was shown that the force output varies by no more than approximately 0.5%.

117
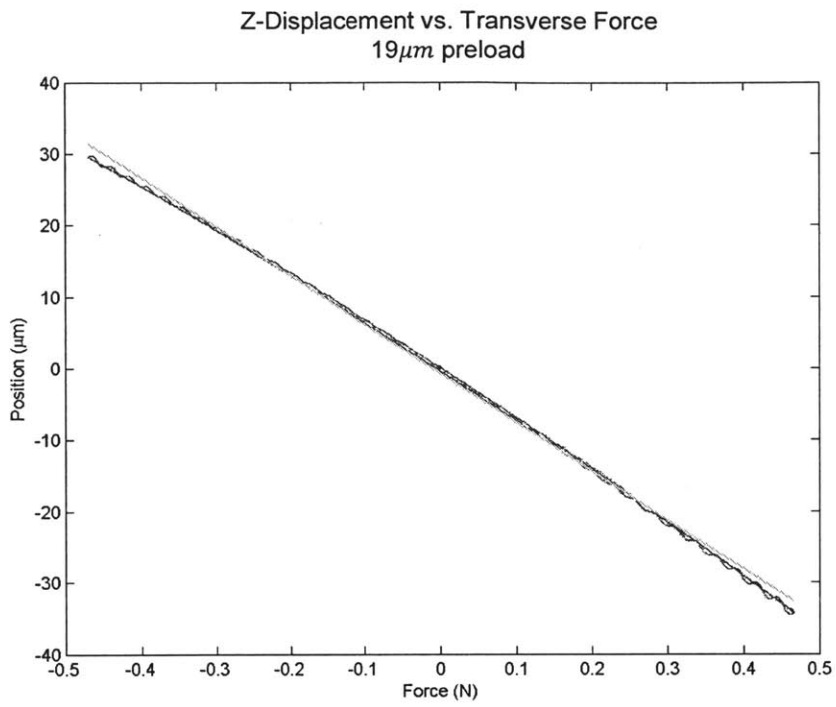
Figure 5.7: Force-displacement relation for a 19 μm preloaded flexure
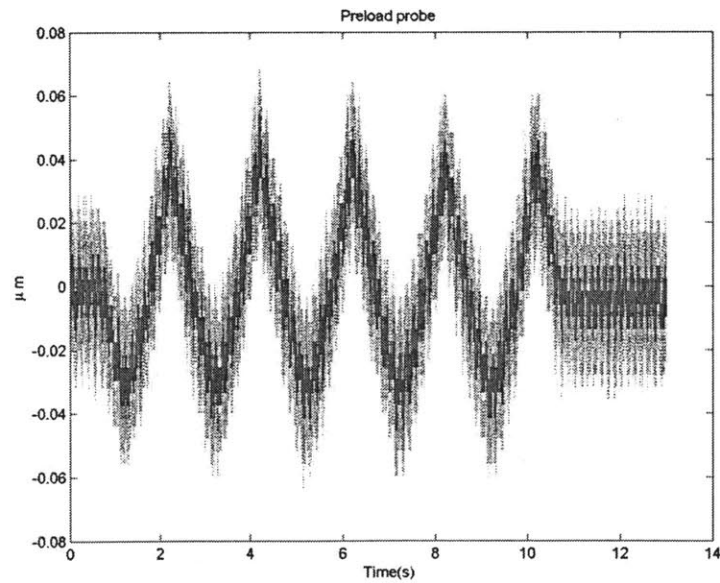
Figure 5.8: Preload variation during 19 μm preload with transverse actuation

118

The curvature can be accounted for by the variation in the preload plot Figure 5.8, with the preload varying approximately $0.04\ \mu m$ in each direction. From the experimental stiffness vs preload data, this is calculated to cause the stiffness to change by approximately 1% in both directions. When the flexure is preloaded, the test stage bows out to the side due to initial imperfections; from Figure 5.4 this initial displacement is approximately $100\ \mu m$. When it is actuated by the voice coil, the voice coil will push the flexures towards their initial straight configuration, which compresses the beam and increases the preload, thus reducing stiffness. It will then pull it away from the initial straight configuration, which stretches the beam and reduces the preload, thus increasing the stiffness. The amount of stretch in the beam can be estimated using the arc length approximation

$$\delta = \int_0^L \frac{1}{2}\left(\frac{dy}{dx}\right)^2 dx = \frac{(\pi z)^2}{4L} \tag{5.18}$$

where δ is the length change of the beam due to the shape of the beam changing, L is the original length of the beam and z is the amount of transverse deflection. From the force-displacement plot Figure 5.7 it is seen that the flexures are displacing approximately $30\ \mu m$ in each direction. Taking into account the initial displacement $z_o = 100\ \mu m$ and the measured deflections of the stage $z = \pm 30\ \mu m$, the net change in length of the beam due to deflections can be computed from

$$\delta_{net} = \frac{\pi^2}{4L}(z - z_o)^2 \tag{5.19}$$

This results in a beam length change of $-0.27\ \mu m$ and $0.37\ \mu m$, corresponding to a beam transverse stiffness change of -4.5% and 6%. The inverse slope at the right end is measured using a fitted line to be approximately $13,100\ \frac{N}{m}$ and at the left end $16,500\ \frac{N}{m}$, devations of -10% and

119

+12.9% respectively from the initial value of 14,600 $\frac{N}{m}$. While the estimate does not perfectly predict the stiffness change when the beam-columns are deflecting, it does raise the issue that the stiffness of the beam can vary significantly from the arc-length change alone; in light of this, compressing a beam by adding displacements may not be adequate to maintain the beam stiffness; maintaining beam stiffness would require a feedback controller that could maintain the loading in the flexure.

Figure 5.9 plots the displacements in the other stage degrees of freedom. It can be seen that in every degree of freedom but θ_z the input force is manifesting itself, though these motions are still within an order of magnitude of the 3σ noise in the probes.

From Table 5.4 it can be seen that the Z displacement is the only motion output that is significantly greater than the noise threshold of the probes; the other directions exhibit some motions but all are within a factor of ten of the probe noise floor, on the order of tens of nanometers or microradians.
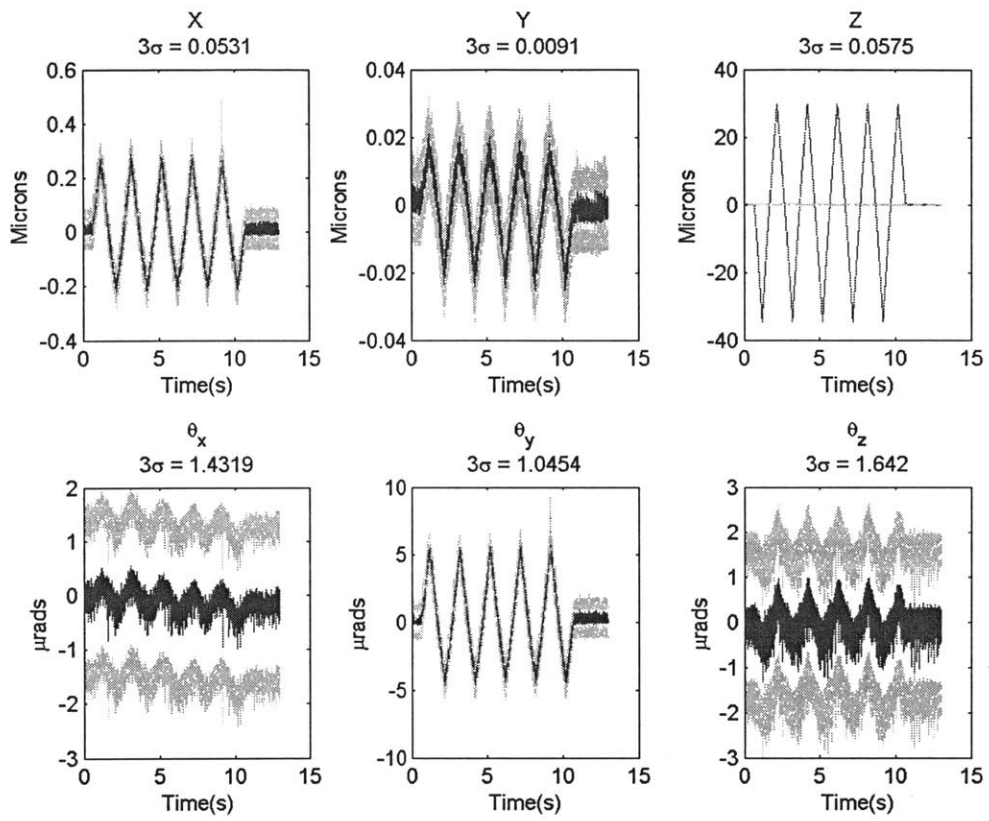
Figure 5.9: Output stage displacements during transverse actuation of 19 μm preloaded flexure

Table 5.4: Ratios of output displacement amplitudes to probe noise uncertainties
Test performed with 19 μm preload

Direction	± 3σ probe uncertainty	Peak-peak output amplitude	$\dfrac{Output}{Noise}$
X	0.0531 μm	0.492 μm	9.27
Y	0.0091 μm	0.044 μm	4.83
Z	0.0575 μm	64.3 μm	1120
θ_x	1.43 μrad	1.12 μrad	0.783
θ_y	1.05 μrad	10.4 μrad	9.91
θ_z	1.64 μrad	1.97 μrad	1.20

5.6 Stiffness versus preload

To determine how the stiffness changes with preload, the following test procedure was performed: the experiment would begin with the flexure un-loaded and the voice coil would be energized to impose a Z-displacement of the test stage, which was then measured. The stiffness in the Z direction was then computed by dividing the input force by the measured displacement. Preload was added to the flexures, and the experiment was repeated – this was continued until the flexure's stiffness was observed to increase rather than decrease, which would indicate that the flexure has entered the post-buckling behavior regime.

Figure 5.7 shows the transverse stiffness of the flexure as a function of the axial preload P and compares it against the energy model developed in §2.6, as well as the model based on the formulas from Roark developed in §2.4.

Transverse stiffness vs. Input displacement models
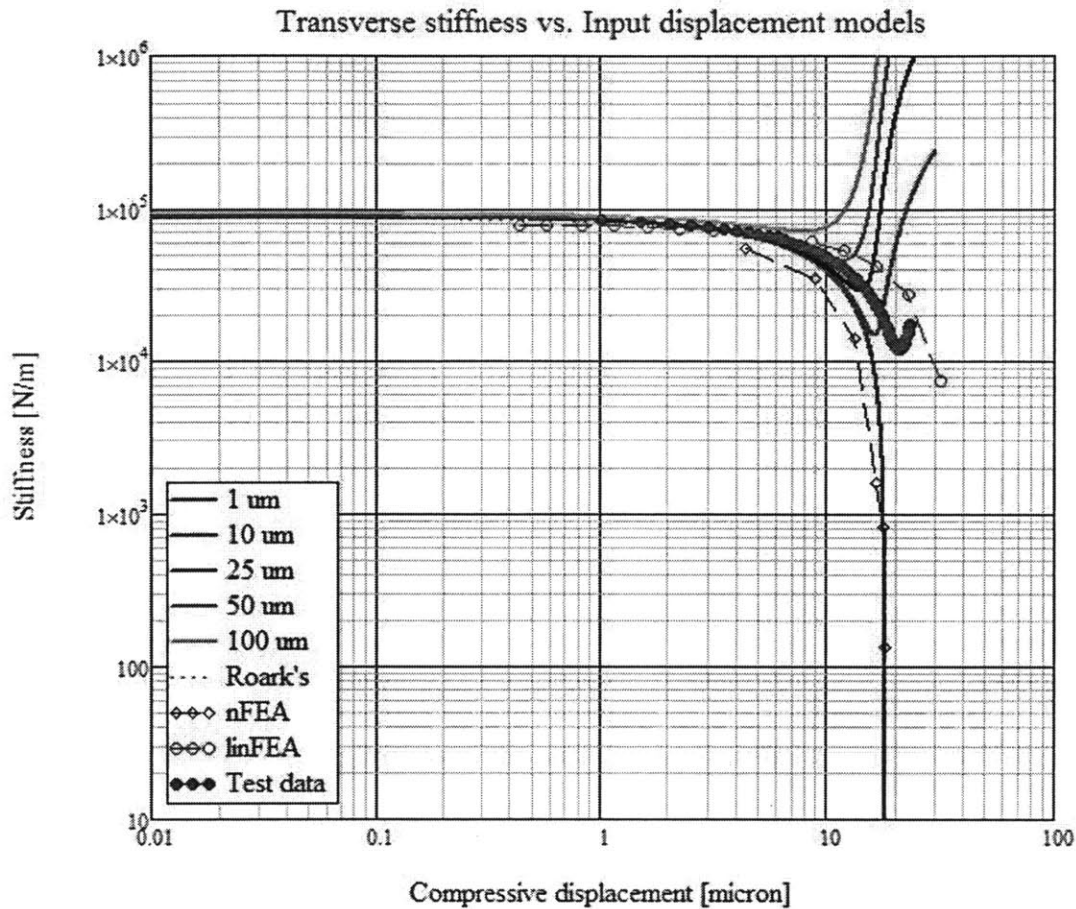
Figure 5.10: Measured Stiffness vs. Input Displacement plotted alongside the energy model.
The test data is plotted as the thicker line.

The overall shape of the flexure's preload vs. stiffness curve is as predicted by the energy

models developed in §2.6. The models begin close to the data; they deviate to within 10% for the

first 50% of the loading range. The 'ideal' models quickly lose their validity as preload is

increased further. Most of the models are within a factor of two for the remainder of the

preloading range. The implications of this are discussed in §5.10.

123

5.7 Time stability of stiffness

In this experiment the flexure was preloaded to approximately 17 μm, and the voice coil is allowed to push on the flexure stage for a period of approximately 6 hours. The input to the voice coil is a 0.5 Hz single-sided square wave (the square wave never goes negative, so the flexure is only pushed, then allowed to come to rest). The displacement between the flexure's rest position and when it is pushed by the voice coil is used to compute the stiffness; this stage motion is recorded by LabVIEW and later processed in MATLAB. The outputs are then plotted to observe any change in the flexure stiffness with time (Figure 5.11). It can be seen that there is a time delay before the flexure settles in from being disturbed; then there is a period where the stiffness steadily increases with time.

It is known from the thermocouple output that the ambient temperature increases by 0.5 $°C$ over the same period. This information can be used to explain the stiffness increase. The difference in the coefficients of thermal expansion in 440C steel $(10 \frac{\mu m}{m°C})$ and 6061-T6 aluminum $(23.6 \frac{\mu m}{m°C})$ is 13.6. The overall length of the flexure including the test stage is 70 mm. If it is assumed that aluminum and steel expand and contract together, and that the aluminum load plates are much more rigid than the steel flexures, then the steel flexure will have an α_{net} of 13.6 $\frac{\mu m}{m°C}$

$$\delta = \alpha_{net} L(\Delta T) \tag{5.20}$$

This results in an extension of 0.476 μm. The initial stiffness of 18,450 $\frac{N}{m}$ corresponds to a preload of 17.75 μm from the data in §5.7. If we follow the stiffness vs preload curve and reduce the preload by 0.5 μm, the new stiffness is 20,181 $\frac{N}{m}$. This agrees with the data shown in

figure Figure 5.11; the change in stiffness is caused by a loss of preload due to a CTE mismatch between the flexure and the load frame.
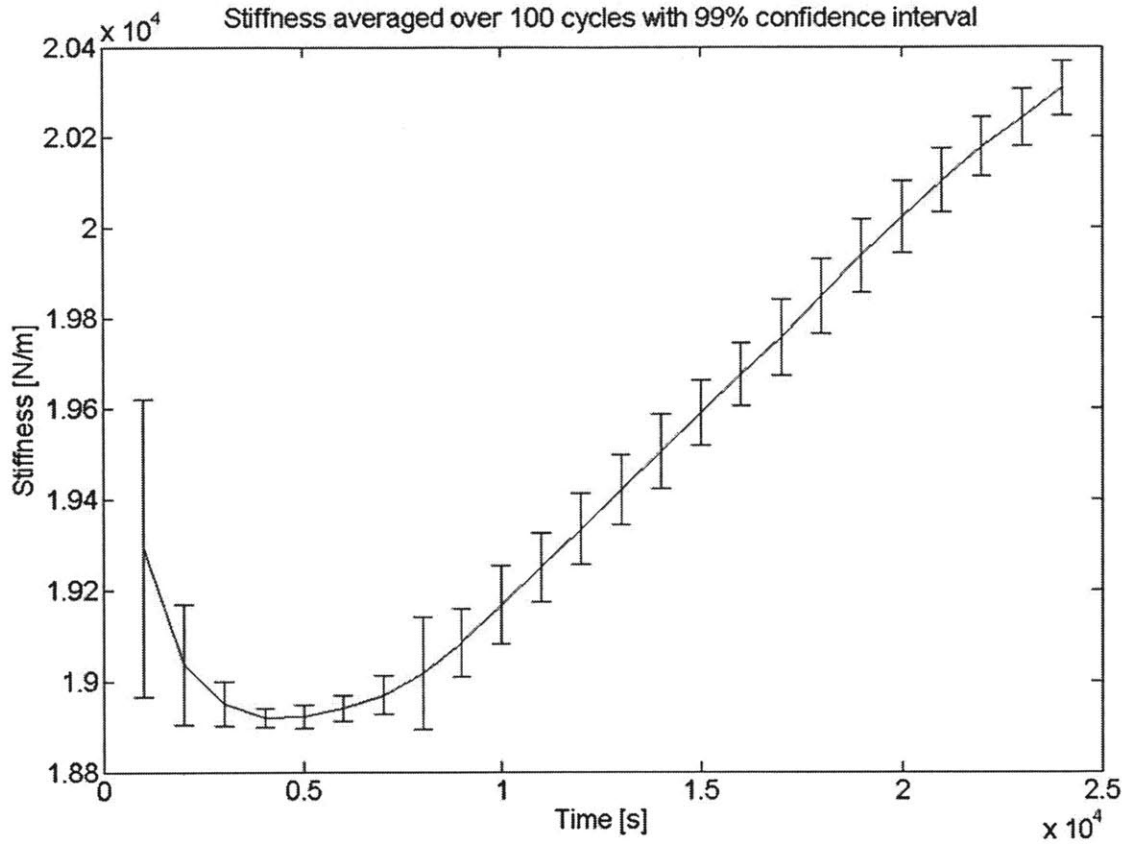
Figure 5.11: Flexure stiffness variation with time, approximately 6 hours.
The increase in stiffness can be explained by the difference in CTEs between the flexure material and the aluminum test setup parts

125

5.8 Presence of hysteresis

At low axial loadings there exist no hysteresis in the Z-displacement plots, such as in 5.4; however, with heavier compressive loadings, hysteresis loops become evident in the output motion of the test stage as shown in Figure 5.12.
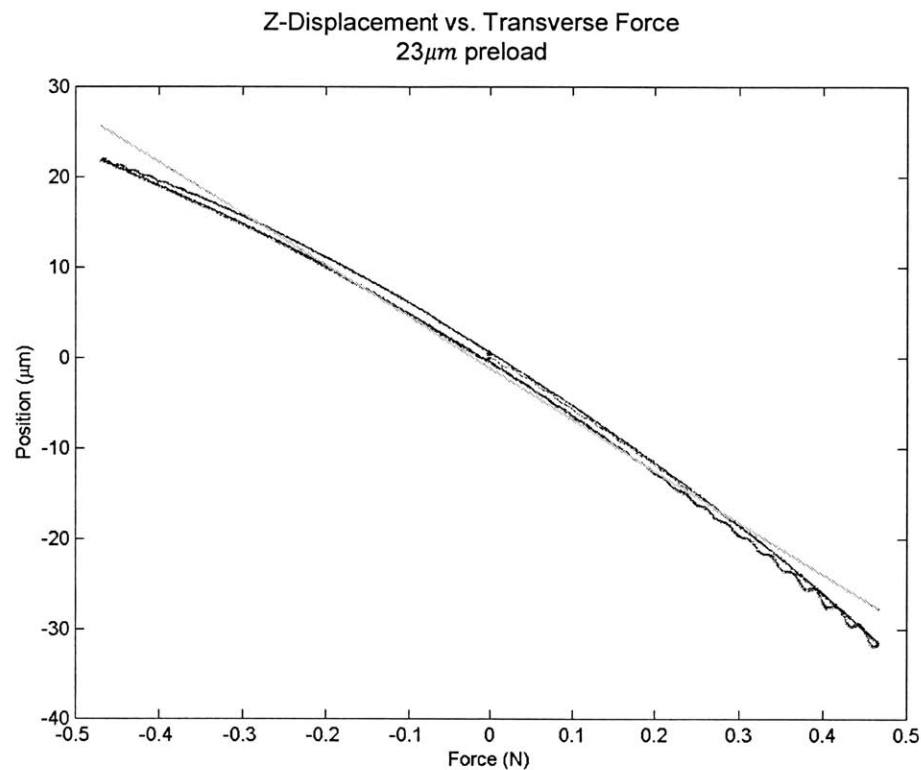
Figure 5.12: Force-displacement plot showing a hysteresis loop and nonlinear behavior

The stress formula for a beam-column, Eq. (2.6(2.26) predicts that stresses diverge as the column approaches Euler buckling; as soon as any plasticity is induced, however, the Euler model no longer applies. Eq. (2.6(2.26) can be used to show that the stresses can grow beyond the yield stress of the material; in this case, using the force-displacement relation Eq. (3.7) and

126

the imperfect beam-column stress relation Eq. (2.6(2.26), the maximum stress in the beam can be written as a function of the ratio of the compressive load to the Euler load.

$$\sigma_{max} = \frac{P}{A}\left(1 + \frac{1}{1-\alpha}\frac{6a}{t}\right), \quad \alpha = \frac{P}{P_E} \tag{5.21}$$

a is assumed to be on the order of 10 μm, and t is 500 μm; this formula can be rewritten as

$$\sigma_{max} = \frac{P}{A}\left(1 + \frac{1}{1-\alpha}0.12\right), \quad \alpha = \frac{P}{P_E} \tag{5.22}$$

If $\alpha = 0.75$, then the multiplier inside the parenthesis becomes 1.48. If $\alpha = 0.9$ the multiplier becomes 2.2; at $\alpha = 0.99$, the multiplier becomes 13. The compressive stress $\frac{P}{A}$ is computed to be 110 MPa; at $\alpha = 0.99$, the stress in the flexure reaches 1430 MPa. Increasing the load only further increases the multiplier; incrementing α to 0.995 brings the multiplier to 25 and the total stress to 2750 MPa, enough to cause yielding in the hardest of steels. It is not unreasonable to assume that approaching the Euler buckling load will cause plasticity and output hysteresis even for a hardened material.

5.9 Presence of parasitic motions

The data sets in §5.3 and §5.5 show that the flexure stage moves in directions other than the desired low-stiffness Z direction. When the flexure is being preloaded, the stage moves in all of its degrees of freedom in response to the input load. When the stage is actuated, the stage moves primarily in the Z axis but some of the input also manifests itself in the other degrees of freedom.

While the flexure is being preloaded, the stage's X and Z directions are expected to experience motion with the input loading. The X direction is the compression axis; as the flexures are being compressed, the stage will move with them by an amount of half the preload input. The Z direction will experience displacements in response to the input loading as discussed in §2.3 due to initial imperfections.

The ratio of the output motion amplitudes after preloading to before preloading are summarized in Table 5.5. The motions in θ_x and θ_z are within a factor of two of the probe noise uncertainty.

Table 5.5: Ratio of output amplitudes during transverse actuation after preloading to output amplitudes before preloading

Direction	$\dfrac{Output\ (with\ preload)}{Output\ (no\ preload)}$
X	3.51
Y	5.57
Z	5.86
θ_x	1.376
θ_y	3.90
θ_z	1.91

5.10 Stiffness Reduction

It was observed that for the test flexures, the stage stiffness was reduced by at most a factor of 7 rather than the larger factors of 100, 1000, or 10000 as proposed in the CSDL patent.

The energy model developed in §2.4 predicts that larger reductions are only possible for flexures with smaller initial imperfections.

From the curves in Figure 5.13 it can be seen that the highest reductions can be achieved by controlling the initial imperfection down to the micron level. The initial imperfection of 7.75 μm gives a curve that best matches the experimental data; however even that curve is off by a fair amount. When the model predicts the lowest stiffness, the data shows a stiffness that is a factor of 2.1 higher than predicted.
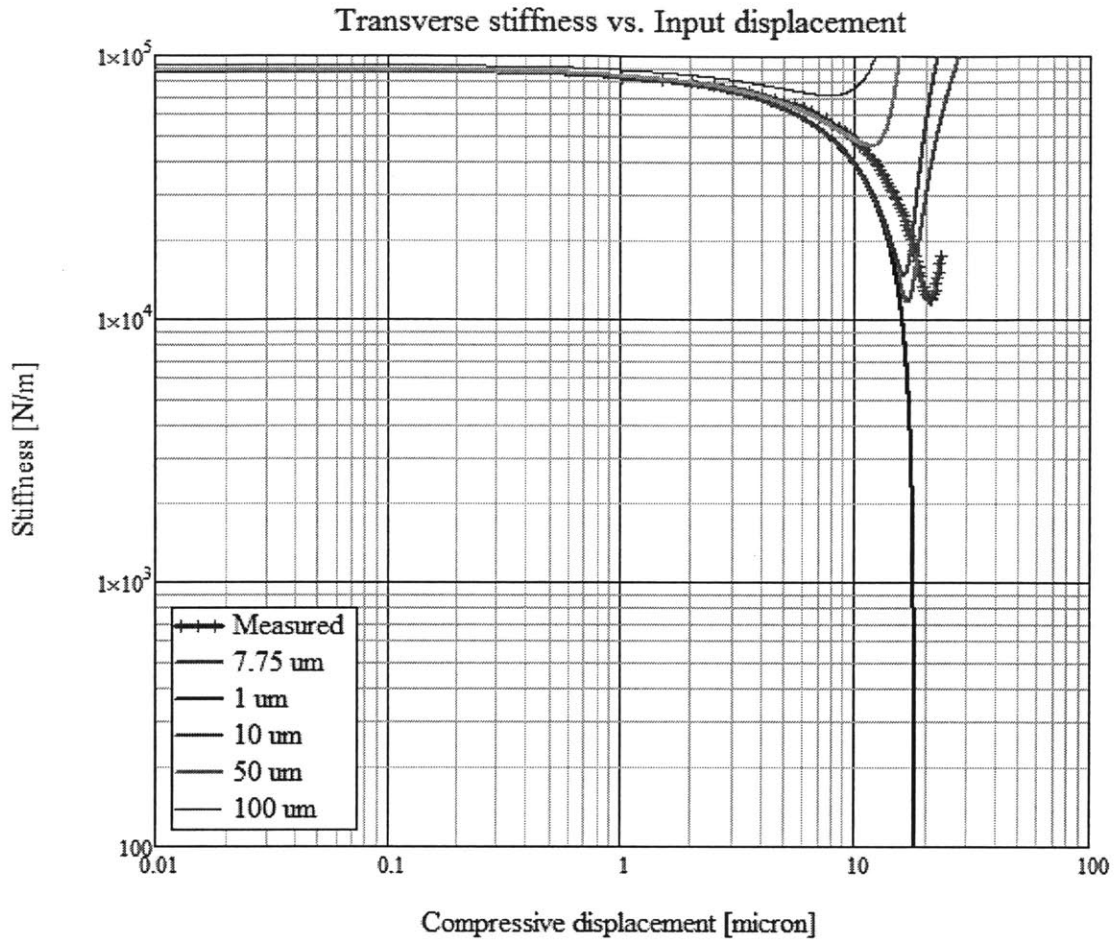
Figure 5.13: Preload vs Stiffness curves with varying initial imperfection.
Increasing imperfection limits the amount of stiffness reduction.

The model is limited in that it cannot pinpoint exactly what the stiffness will be when preload is added; however, what is learned from the model is the behavior of the flexure in response to initial imperfections. With further modeling effort a stronger model can be made that accurately predicts the stiffness of the flexures in response to compressive loading.

6

SUMMARY AND FUTURE WORK

6.1 Summary

A monolithic flexure stage supported by four tunable-stiffness flexural bearings was designed. This stage was designed with a secondary flexure stage designed to apply uniaxial compression to the four tunable flexural bearings. An experimental setup was designed that could measure six degrees of freedom of a test stage and the displacement of an input stage. The stiffness of the flexural bearings was reduced by a factor of approximately seven, falling short of the theoretical expectations of reductions of 1,000 or 10,000. Models developed to study the behavior of compressed flexures show that initial imperfections can compromise the ultimate amount of reduction that can be achieved.

It has been shown that stiffness reduction of at least one order of magnitude is achievable; higher stiffness reduction ratios remain achievable but were not observed in these experiments.

For designers who wish to use compressed flexures as very-low-stiffness suspension elements, this thesis has shown that initial imperfections ultimately reduce the largest stiffness

reduction achievable; designing a fixture and fabricating a flexure preloading assembly that does not introduce initial imperfections, or keeps the ratio of flexure thickness to imperfection to less than 500 would allow these very low stiffnesses to be achieved.

For designers who wish to use the compressed flexure as a tunable spring, a linear model has been developed that allows designers to design a compressed flexure in the variable-spring regime, Eq. (2.2) that remains accurate to within 10% compared to the exact model at preloads as high as 90% of the buckling load. When compared with test data, the linearized model (6.23) remains within 20% of the test data for 50% of the preloading range.

$$k_{lin}(P) = \frac{192EI}{l^3} - \frac{24}{5l}P \tag{6.23}$$

It has been shown that compressed flexures are highly sensitive to temperature variations; a 0.5 °C change resulted in an 11% increase in stiffness. It is hypothesized that controlling the flexure temperature can be used to control the amount of preload in the flexures. If compressed flexures are to be used in a precision system, special care must be taken to ensure a thermocentric design so that the compressed flexure elements will be immune to temperature variations and will not be losing or gaining preload due to these variations.

Guidelines for designing with compressed flexures have been generated. Compressed flexures should be designed with the intention of minimizing initial imperfections; the designer should be acutely aware of the impact that initial imperfections can have on compressed flexure performance. The strain-energy based model derived in this work predicts that initial imperfections ultimately limit the amount of stiffness reduction possible.

6.2 Transitioning from mechanical elements to mechanical systems

In this thesis, a flexural stage supported by four compressed flexures allowing one degree of freedom was considered. When designing with flexures it is often the case that more than one degree of freedom is desired; the flexure designer is able to combine the degrees of freedom of two sets of flexures by combining flexures in series. Alternatively, connecting flexure elements in parallel will keep the degrees of freedom common to both. Suppose that a designer wishes to use several compressed-flexures together to achieve some design goal, such as a low-stiffness two degree of freedom stage. Two stages such as the one studied in this thesis could be combined in series to allow two degrees of freedom. Of particular interest would be to study how the initial imperfections propagate through the assembly, and if both flexure assemblies could have their stiffnesses reduced by the same amount.

6.3 Low-stiffness rotational pivots

One example of a mechanical system that is composed of compressed flexures is a low-
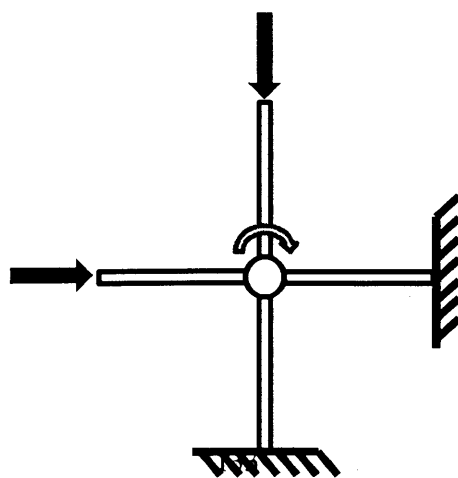
Figure 6.1: Low-stiffness pivot based upon compressed flexures

torsional-stiffness pivot such as the one described in the Draper patent [3]. Similar energy-minimizing methods as those used in this thesis can be used to model the behavior of compressed flexures oriented around a rotating element; such low-rotational-stiffness or tunable-stiffness pivots could find use in instrumentation and merit investigation.

6.4   In-depth study of stresses

The addition of a large compressive preload increases the overall stress in the flexure and shortens the life of the flexural bearing. A fatigue study was not performed in this thesis but would be important for most applications. The effect of initial imperfection on the stresses in the beam was shown by the model developed in §2.8 to have a multiplying effect; larger initial imperfections multiply the compressive stress. Continued work on compressed flexures would include a detailed study on the stress field in the compressed flexure along with the effect of the compression on fatigue life. An experimental setup where a beam-column with several strain gages is subjected to simultaneous deflection and compression, and could also have arbitrary initial imperfections imposed could be used to study the stresses as they develop in response to the combined effects of initial imperfections and loadings. Stresses in the beam-column must be controlled, or else the beam-column could develop hysteresis or fail prematurely due to fatigue.

6.5   Hysteresis study

During experimentation it was noticed that under higher preloads, the transverse force-displacement output would repeatably exhibit a hysteresis loop; hysteresis is undesirable in a flexural bearing as it is nonlinear behavior and prevents the flexure from being modeled as an ideal spring. An example of such output is shown in Figure 5.12.

It is hypothesized that the hysteresis is likely dependent on the flexure material, the initial imperfection of the beam, and the stress in the beam, which itself depends on the magnitude of the inputs. Some materials, such as aluminum, do not have a well-defined yield point and will always exhibit some plastic deformation even below the yield stress – this is known as microplasticity. Also of interest to know whether this microplastic behavior would be present in nonmetallic materials such as silicon (which would most likely be the material for a MEMS compressed flexure)

6.6 Investigate sources of initial imperfections

In this thesis it has been shown that initial imperfections play a commanding role in determining the stiffness behavior of compressed flexures and how close they approach ideal behavior. A next step would be to investigate sources of initial imperfections, either from manufacturing or assembly, and to learn whether or not these imperfections can be eliminated or minimized through specialized manufacturing or assembly techniques. Testing an assortment of beams with known imperfections could provide new design insight into how tolerant compressed flexures can be to initial imperfections. A setup such as the one described in §6.4 could be used to perform such initial-imperfection tests.

6.6.1 MEMS devices: microfabrication

For integration into MEMS devices, an investigation should be performed into potential sources of initial imperfection in MEMS microfabrication. Potential sources of initial imperfections include:

- Deformations due to thermal stresses during depositions

- Mask alignment errors

- Strains due to insulator/substrate thermal coefficient mismatch

Future work would include quantifying the effects of the above error sources and their impact on the compressed flexures.

6.6.2 Macro-scale devices: machining and assembly imperfections

The error sources for microfabricated compressed flexures are different from a larger-scale compressed flexure assembly, such as the flexure assembly used in this thesis. Larger-scale assemblies must consider the effects of larger-scale manufacturing processes such as CNC milling and the effects of multiple-component assemblies.

6.7 Calibrating imperfect flexures

It is hypothesized that by using sensors to detect deviations from beam straightness and utilizing feedback to correct these errors, initial imperfections can be greatly reduced or even eliminated. This would allow the experimenter to observe even greater stiffness reduction ratios, according to the model developed in §2.4, potentially to the reduction of 10,000 as predicted in the Draper patent. However, such a design could be problematic in that if the stage is being controlled under feedback, it would not be able to move. For sensing purposes, a nulling arrangement could perhaps be utilized, for example in the case of an accelerometer (see figure below).
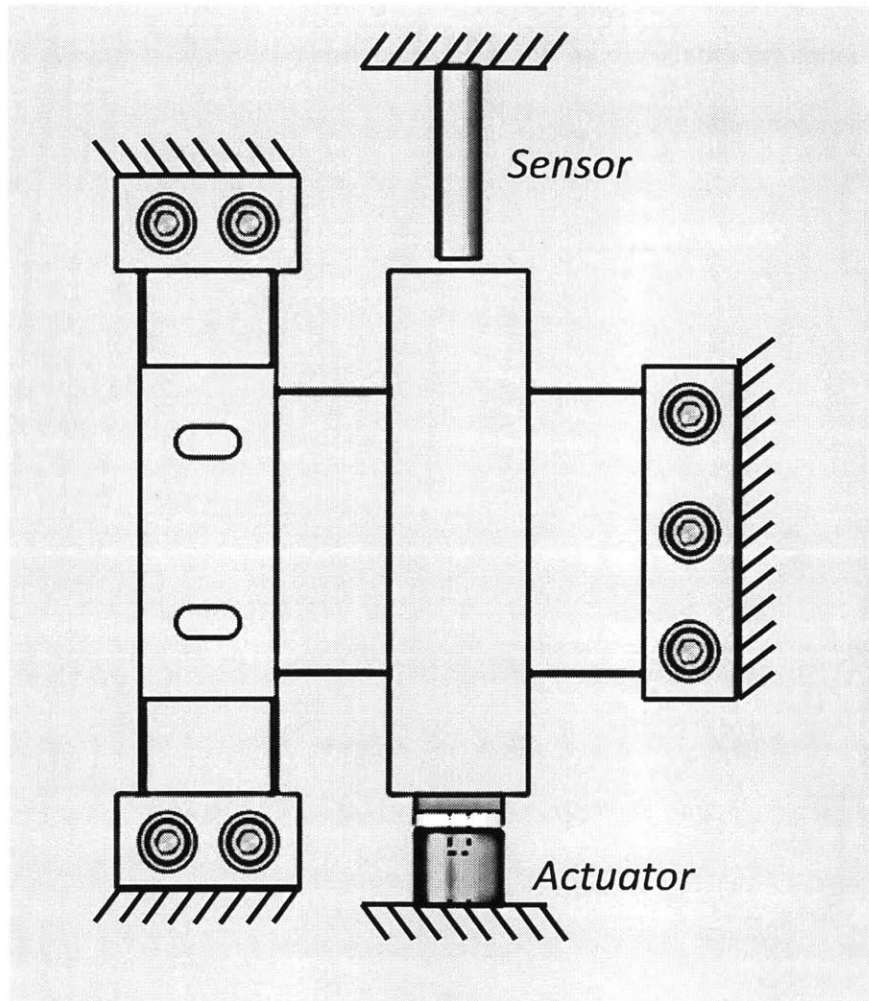
Figure 6.2: Sensor and actuator arrangement for sensing with nulling.
A disturbance force perturbs the central stage from its center, which is detected by the
sensor. The actuator restores the stage to its center. The actuator effort is a measure of
the disturbing force.

6.8 Beams with other boundary conditions

In this thesis only beams with fixed-fixed boundary conditions were investigated (zero

deflection and slope at the beam ends), but it is possible to design other useful flexural systems

that do not have these boundary conditions. Of particular interest are flexures which are mounted

137

serially with other flexures; such flexures do not have simple boundary conditions such as fixed-fixed or clamped-clamped. In these cases the rotational stiffness of the joint must be taken into consideration when computing buckling loads.

REFERENCES

[1] S. T. Smith, Flexures: Elements of Elastic Mechanisms, CRC Press LLC, 2000.

[2] L. Howell, Compliant Mechanisms, New York, NY: John Wiley & Sons, 2001.

[3] L. J. Jenkins, J. J. Bernstein and D. C. Fyler, "Flexure assemblies and methods for manufacturing and using the same". United States of America Patent 0132088, 2011.

[4] K. Yoder, M. Dwyer and N. D'Souza, "Prestressed Ceramic Coatings for Enhanced Reliability of Silicon Wafer Fracture Strength," *IEEE Transactions on Advanced Packaging,* vol. 30, no. 4, pp. 705-711, November 2007.

[5] S. Woinowsky-Krieger, "The effect of an axial force on the vibration of hinged bars," *Journal of Applied Mechanics,* vol. 17, pp. 35-36, 1950.

[6] J. E. Teter Jr., "A Discussion of Zero Spring Rate Mechanisms Used for the Active Isolation Mount Experiment," NASA, Hampton, 1999.

[7] S. E. Woodard and J. M. Housner, "Nonlinear Behavior of a Passive Zero-Spring-Rate Suspension System," *Journal of Guidance, Control, and Dynamics,* vol. 14, no. 1, pp. 84-89, January-February 1991.

[8] B. Hälg, "On a Micro-Electro-Mechanical Nonvolatile Memory Cell," *IEEE Transactions on Electron Devices,* vol. 37, no. 10, pp. 2230-2236, 1990.

[9] W. Fang and J. A. Wickert, "Post buckling of micromachined beams," *Journal of*

micromechanical microengineering, no. 4, pp. 116-122, 1994.

[10] S. Timoshenko and J. Gere, Theory of Elastic Stability, 2nd ed.

[11] W. C. Young and R. G. Budynas, Roark's Formulas for Stress and Strain, 7th ed., New York: McGraw-Hill Companies, Inc., 2002.

[12] A. H. Slocum, Precision Machine Design, Dearborn: Society of Manufacturing Engineers, 1992.

[13] R. M. Jones, Buckling of Bars, Plates, and Shells, Blacksburg: Bull Ridge Publishing, 2006.

[14] A. Shorya, *Synthesis and Analysis of Parallel Kinematic XY Flexure Mechanisms,* Cambridge, MA: Ph.D Thesis, Massachusetts Institute of Technology, 2004.

[15] H. C. Layton, *Principles and Techniques for Designing Precision Machines,* Cambridge, MA: , 1999.

[16] D. L. Blanding, Exact Constraint: Machine Design Using Kinematic Principles, New York: ASME Press, 1999.

[17] S. T. Smith and D. G. Chetwynd, Foundations of Ultraprecision Mechanism Design, Taylor & Francis Books Ltd, 1998.

[18] W. L. Hallauer and C. Ma, "On the mechanical behavior of slender, slightly curved, compressed microbridges," *Journal of Micromechanical Microengineering,* vol. 21, 2011.

[19] W.-F. Chen and T. Atsuta, Theory of Beam Columns: In-Plane Behavior and Design, Volume 1, J. Ross Publishing, 2008.

[20] S. D. Senturia, Microsystem Design, Kluwer Academic Publishers, 2001.

[21] J. Hartog, Mechanics, New York: Dover Publications, Inc, 1948.

(this page intentionally left blank)

(this page intentionally left blank)

A

PROBE AND STAGE OUTPUT NOISE

A.1 Coordinate system

The coordinate system and probe numbering used in this thesis is shown below. Probes 4, 5 and 6 are arranged in an equilateral triangle of side length a. The centroid of the equilateral triangle is coincident with the centroid of the test stage. Probes 2 and 3 are placed a distance $2L$ apart.
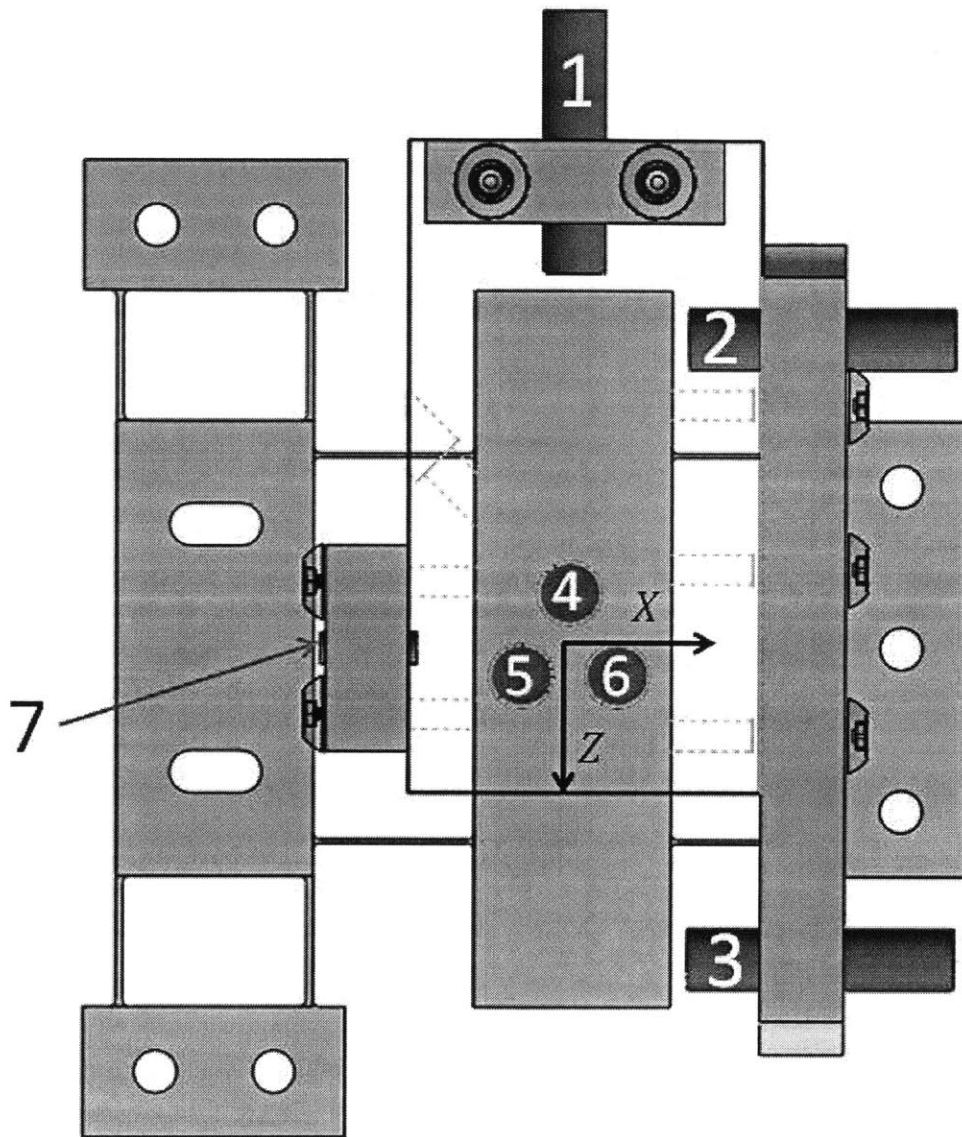
Figure A.1: Coordinate system and probe arrangement around test stage.
Y is the out of plane direction.

A.2 Converting probe displacements to stage motions

The probe output vector δ is a column vector with probe outputs $\vec{\delta} = [\delta_1, \delta_2, \delta_3, \delta_4, \delta_5, \delta_6]$

The stage displacements vector is $\vec{X} = [X, Y, Z, \theta_x, \theta_y, \theta_z]$

With geometric parameters:

$$a = 0.014665 \ m$$

$$L = 0.0508 \ m$$

Probe outputs $\vec{\delta}$ can be converted to and from stage displacements $\vec{X}$ via a transformation matrices

$$\vec{\delta} = J\vec{X} \qquad\qquad \vec{X} = J^{-1}\vec{\delta}$$

$$
J = \begin{pmatrix}
0 & 0 & -1 & 0 & 0 & 0 \\
1 & 0 & 0 & 0 & -1 & 0 \\
1 & 0 & 0 & 0 & 1 & 0 \\
0 & 1 & 0 & \dfrac{a\cdot\sqrt{3}}{4} & 0 & 0 \\
0 & 1 & 0 & \dfrac{-a\cdot\sqrt{3}}{4} & 0 & \dfrac{-a}{2} \\
0 & 1 & 0 & \dfrac{-a\cdot\sqrt{3}}{4} & 0 & \dfrac{a}{2}
\end{pmatrix}
\qquad
J^{-1} = \begin{pmatrix}
0 & \dfrac{1}{2} & \dfrac{1}{2} & 0 & 0 & 0 \\
0 & 0 & 0 & \dfrac{1}{2} & \dfrac{1}{4} & \dfrac{1}{4} \\
-1 & 0 & 0 & 0 & 0 & 0 \\
0 & 0 & 0 & \dfrac{2\cdot\sqrt{3}}{3\cdot a} & -\dfrac{\sqrt{3}}{3\cdot a} & -\dfrac{\sqrt{3}}{3\cdot a} \\
0 & -\dfrac{1}{2\cdot l} & \dfrac{1}{2\cdot l} & 0 & 0 & 0 \\
0 & 0 & 0 & 0 & -\dfrac{1}{a} & \dfrac{1}{a}
\end{pmatrix}
$$

Figure A.2: Transformation matrices used to convert probe outputs to stage displacement outputs

A.3 Probe and output stage noise

The noise in the capacitance probes was measured by taking a 30 second sample of data and computing the standard deviation of the noise over three trials. The noise values for each probe is given in Table A.1 below.

Table A.1: Probe noise, one standard deviation, averaged over three trials. Probes 1-3 and 7 are in low-resolution mode; 4-6 are in high-resolution mode

Probe	$\sigma\ [nm]$
1	9.58
2	9.95
3	14.5
4	2.3
5	3.7
6	1.5
7	8.7

The probe noise is converted to stage displacement noise by computing the propagation of error. The output stage noise due to the propagated probe noise is shown in Table A.2; this computation is done in the MathCAD worksheet *probe_error_propogation.xmcd.*

146

Table A.2: Output stage displacement uncertainty values, 99.7% confidence interval

Direction	$\pm 3\sigma$ [nm]
X	53.1
Y	9.1
Z	57.5
θ_x	1.43
θ_y	1.05
θ_z	1.64
Input	52.2

(this page intentionally left blank)

B

EXPERIMENTAL SETUP TOLERANCES

B.1 Test setup modules

The test setup modules were designed to be machined on a CNC mill having approximately 12 μm tolerances, therefore it is expected that the tolerances for any features that can be machined in a single CNC run is on the order of 10 μm. Some of the parts required multiple fixturing setups during machining; for those features the tolerances likely widen to approximately 100 μm due to refixturing. Such features include the holes drilled into the sides of the load plates and the pockets milled for the kinematic coupling balls.

B.2 Flexure tolerances

The flexure was cut on a wire EDM which had 5 μm tolerances. The most critical features of the test flexure were the thicknesses of the flexures, since deviations in the thickness change the buckling parameters of the flexures. The Euler buckling load is proportional to t^3 where t is the thickness of the flexure. A 5 μm tolerance represents at most a 2% deviation in thickness and a 6% change in the Euler buckling load; it is strongly recommended that the tolerances be no looser than this. Increasing the tolerance to 25 μm could cause a maximum thickness deviation of 50 μm, which represents 10% of the flexure thickness and a deviation in

the Euler buckling load of 33%. It is recommended that the flexures be cut with a wEDM if possible.